SOFT HIERARCHICALLY-STRUCTURED BIOMATERIALS

DEVELOPING SOFT HIERARCHICALLY-STRUCTURED BIOMATERIALS USING PROTEINS AND BACTERIOPHAGES

By LEI TIAN, B.Eng., M.Eng.

A Thesis Submitted to the School of Graduate Studies in Partial Fulfilment of the Requirements for the Degree Doctor of Philosophy

DOCTOR OF PHILOSOPHY (2022)

Chemical Engineering, McMaster University

1280 Main St W, Hamilton, Ontario L8S 4L7

TITLE: Developing Soft Hierarchically-Structured Biomaterials Using Proteins and Bacteriophages

AUTHOR: Lei Tian

B.Eng. (Southeast University, China)

M.Eng. (Southeast University, China)

SUPERVISOR: Dr. Zeinab Hosseinidoust

NUMBER OF PAGES: xxiii, 155

Lay Abstract

Bacteriophages (bacterial viruses), also known as phages, are natural bacteria predators. These viruses act as direct missiles, each phage targeting limited groups of bacteria. In addition, phages are an endless resource for self-propagating nanoparticles that can be used as building blocks for new material.

I developed a platform for manufacturing a large quantity of microscale beads made of millions of phages. These micro-beads can be sprayed on fresh produce and meat to remove bacterial contamination (with the added benefit of not affecting taste or smell). I also printed phages on substrates, like an ink. The printed phage ink evolved into a patented technology for designing phage coatings on surfaces with very high surface area, like the small structures on our fingers. This phage coating was successfully used to test the existence of bacteria in liquids.

Abstract

Bio-interface topography strongly affects the nature and efficiency of interactions with living cells and biological molecules, making hydrogels decorated with micro and nanostructures an attractive choice for a wide range of biomedical applications. Despite the distinct advantages of protein hydrogels, literature in the field has disproportionately focused on synthetic polymers to the point that most methods are inherently incompatible with proteins and heat-sensitive molecules.

We report the development of multiple biomolecule-friendly technologies to construct microstructured protein and bacteriophage (bacterial virus) hydrogels. Firstly, ordered and sphericity-controllable microbumps were obtained on the surface of protein hydrogels using polystyrene microporous templates. Addition of protein nanogels resulted in the hierarchical nano-on-micro morphology on the microbumps, exhibiting bacterial repellency 100 times stronger than a flat hydrogel surface. The developed microstructures are therefore especially suitable for antifouling applications.

The microstructures created on protein hydrogels paved the way for applying honeycomb template on proteinous bacterial viruses. We developed a high-throughput method to manufacture isolated, homogenous, pure and hybrid phage microgels. The crosslinked phages in each phage-exclusive microgel self-organized and exhibited a highly-aligned nanofibrous texture. Sprays of hybrid microgels loaded with potent virulent phage effectively reduced heavy loads of multidrug resistant *Escherichia coli* O157:H7 on food products by 6 logs.

We further expanded on bottom-up assembly of phages by printing phage bioinks in microdot arrays on prestressed flexible polystyrene substrates. Through a new biomolecule-friendly wrinkling method, the substrates were shrunk through critical point drying, leading to the formation of wrinkle structures on the attached phage microdots. This wrinkle-forming method was heat-free and preserved the delicate ordered nanostructure of phage bundles. Diverse wrinkle morphologies of the microdots were achieved by controlling the attachment and thickness of the microdots. The controllable microscale wrinkles and the nanofibrous phage bundles constituted a 3-level hierarchical structure on phage microdots and provided large surface area, making it a great candidate as a biosensing interface. DNAzyme was further incorporated into bioink to fabricate hybrid wrinkled phage microdots for bacteria-detection.

Acknowledgements

First and foremost, I want to express my sincerest appreciation to my supervisor Dr. Zeinab Hosseinidoust for tremendous support and guidance throughout my Ph.D. period. It was one of the best life choices I made to join her lab and get involved with bacteriophage research. When I came to McMaster, I could not speak English fluently (was very quiet in her classes) and never performed any aseptic biological experiment before. She helped me become a more passionate, confident, skilled and critical researcher. My career and research path would not be the same without her guidance.

I would also like to extend my thanks to the professors, Dr. Tohid Didar, Dr. Robert Pelton, and Dr. Leyla Soleymani, for their useful suggestions and constructive criticisms on my research design, which enabled me to think beyond my field to deepen my conceptual understanding and improve my research quality.

Special thanks to my amazing labmates and collaborators, Kyle Jackson, Leon He, Mathura Thirugnanasampanthar, Mellissa Gomez, Fereshteh Bayat, Shadman Khan, Gaoyin He, Amid Shakeri. My time in the lab would not have been so enjoyable without you.

It was my great pleasure to have acquainted with so many friends in Canada who gave me endless memories and made my life enjoyable, including Yinxin Li, Yichen Wu, Nan Zhang, Wenjuan Wang, and those that were not mentioned.

Finally, I would like to dedicate my dissertation to my dear parents who gave me the biggest love, patience, and encouragement throughout my Ph.D. period. I am so excited to start the next chapter of my life.

Table of Contents

List of Figures

List of Tables

List of Abbreviations

2D: Two-dimensional

3D: Three-dimensional

AFM: Atomic force microscopy

AMR: Antimicrobial Resistance

BSA: Bovine serum albumin

B. subtilis: *Bacillus subtilis*

CFU: Colony-forming unit

CPD: Critical point dry

C. perfringens: *Clostridium perfringens*

E. coli: *Escherichia coli*

EDC: 1-ethyl-3-(-3-dimethylaminopropyl) carbodiimide hydrochloride

Ex/em: Excitation/emission

FTIC: Fluorescein isothiocyanate

FTIR: Fourier transform infrared

GA: Glutaraldehyde

GDP: Gross domestic product

LB: Luria-Bertani

LED: Light emitting diode

L. monocytogenes: *Listeria monocytogenes*

OD: Optical density

PBS: Phosphate-buffered saline

PDMS: Polydimethylsiloxane

PEG: Poly(ethylene glycol)

PFU: Plaque-forming unit

PMMA: Polymethyl methacrylate

P(NIPAAm): Poly(N-isopropylacrylamide)

POEGMA: Poly(oligoethylene glycol methacrylate)

PS: Polystyrene

PVA: Poly(vinyl alcohol)

RGD: Arginylglycylaspartic acid

S. aureus: *Staphylococcus aureus*

SEM: Scanning electron microscope

TEM: Transmission electron microscopy

TSB: Tryptic Soy Broth

UV: Ultraviolet

VLP: Virus-like particles

Declaration of Academic Achievement

This Ph.D. dissertation is organized in a "sandwich style" based on published, submitted and prepared for submission articles described as follows:

First-author publications

1. L. Tian, K. Jackson, A. Zhang, Z. Wan, A. Saif, Z. Hosseinidoust, Bacteriophage-Built Gels as Platforms for Biomedical Applications, The Canadian Journal of Chemical Engineering, in press.
2. L. Tian, L. He, K. Jackson, R. Mahabir, Z. Hosseinidoust. Bacteria Repellent Protein Hydrogel Decorated with Tunable, Isotropic, Nano-On-Micro Hierarchical Microbump Array, Chem. Commun., 2021, 10883. https://doi.org/10.1039/D1CC03741B.
3. L. Tian, L. He, K. Jackson, A. Saif, S. Khan, Z. Wan, Z. Hosseinidoust, Self-Assembling Nanofibrous Viral Microgels as Sprayable Antimicrobials Targeting Multidrug-Resistant Bacteria, under minor revision in Nature Communications, NCOMMS-22-00018A-Z.
4. L. Tian, S. Khan, A. Saif, A. Shakeri, K. Jackson, Z. Hosseinidoust, Printed Viral Microdot Arrays with Tunable Three-Level Hierarchically Wrinkle Morphology as Biosensing Chips, manuscript in preparation.

Patents

1. Zeinab Hosseinidoust, Lei Tian, 2021, Hydrogel Microstructure Arrays, Methods of Making and Uses Thereof, 63/261803.

2. Zeinab Hosseinidoust, Lei Tian, Kyle Jackson, 2020, Bacteriophage Hydrogel Compositions and Uses Thereof, 16112-8 (157885).
3. Zeinab Hosseinidoust, Lei Tian, 2022, 3D Hierarchical Wrinkled Structures, Methods of Making and Uses Thereof, RoI.

Co-author publications

1. A. Peivandi, L. Tian, R. Mahabir, Z. Hosseinidoust. Hierarchically Structured, Self-Healing, Fluorescent, Bioactive Hydrogels with Self-Organizing Bundles of Phage Nanofilaments, Chemistry of Materials, 2019, 31, 5442.
2. G. He, L. Tian, A. Fatona, X. Wu, H. Zhang, J. Liu, M. Fefer, Z. Hosseinidoust, R. Pelton, Water-Soluble Anionic Polychloramide Biocides Based on Maleic Anhydride Copolymers. Colloids and Surfaces B: Biointerfaces, 2022, 112487.
3. A. Peivandi, K. Jackson, L. Tian, L. He, A. Mahmood, C. Fradin, Z. Hosseinidoust, Inducing Microscale Structural Order in Phage Nanofilament Hydrogels via Macromolecular Crowding with Globular Proteins, ACS Biomaterials Science & Engineering, 2022, 8, 340.
4. K. Jackson, A. Peivandi, M. Fogal, L. Tian, Z. Hosseinidoust, Filamentous Phages as Building Blocks for Bioactive Hydrogels. ACS Applied Bio Materials, 2021, 4, 2262.

Upcoming Publications (Expected in 4 months)

5. M. Thirugnanasampanthar, D. Libera, L. Tian, R. Rhem, M. Dolovich, Z. Hosseinidoust, Influence of Ambient Humidity on Viral and Bacterial Filtration Efficiency Exhibited of Respirators.
6. A. Shakeri, S. Khan, L. Tian, Z. Hosseinidoust, T. Didar, Detection of *Legionella* from Water via DNAzyme-Embedded Hydrogels with Ring Structures.
7. G. He, L. Tian, A. Fatona, X. Wu, H. Zhang, J. Liu, M. Fefer, Z. Hosseinidoust, R. Pelton, Factors influencing bactericidal activity of anionic and cationic, water-soluble polychloramides.

Chapter 1: Introduction and Objectives

1.1 Introduction

1.1.1 Structured soft biomaterials

Soft biomaterials are soft matter based on biologics such as lipids, nucleic acids, proteins, cellulose, viruses or cells.[1,2] Hydrogels made with protein,[3,4] viruses[5,6] and DNA[7] have shown excellent injectable, environment-responsive, biocompatible properties, constituting a powerful platform for tissue engineering, drug delivery and biosensing. These properties and structures are significantly affected by their inner and interfacial structures.

When it comes to defining/characterizing the nature of structured soft biomaterials, the structures we discuss here do not include the inner-molecular structures, such as protein folding or protein alignment on viral capsids. Instead, the self-organizing structures of building blocks and artificially-induced micro/nano-structures in these biomaterials are the subject of interest. To date, the work on structured soft biomaterials have been focused on cellulose hydrogels where microstructures enhanced their performance on tissue engineering and biosensing.[8,9] Meanwhile, casting microstructures on other soft biomaterials have been rarely investigated.

Work in our lab has focused on using bacteriophages and globular proteins as building blocks to fabricate soft hydrogels.[6,10,11] Compared to cellulose nanocrystals, bacteriophages offer diversity in shape and size, self-propagation, and more importantly, potential for multiplex biorecognition. The background literature corresponding to the research outlined in this thesis is discussed in detail in chapter 2. In general, crosslinked

phages in the hydrogels retained bioactivity and self-organized into hierarchical structures.[6] Moreover, phage hydrogels exhibit autofluorescence and self-healing.[6] These properties makes them well suited for biomedical applications, allowing for antimicrobial implant coating or burn-wound dressing. However, designing microstructures on phage hydrogels has, to date, been rarely investigated despite its critical importance for bio-interfacial and biosensing applications. Thus, there is a clear research opportunity to develop heat-free and even solvent-free strategies to fabricate microstructured protein and phage hydrogels.

1.1.2 Honeycomb films: a potential template for structured biomaterials

Orderly porous polymer film (honeycomb film) is a critical foundation of templating method to cast microstructures. Such films exhibit extremely high specific surface areas which allow their employment in a lot of applications including self-cleaning surfaces,[12,13] electrodes,[14] sensors[15] and in our case, molding.[16,17] So far, multiple methods have been developed to obtain honeycomb structure, including utilizing self-assembled surfactants,[18] using templates such as ordered array of colloidal particles[19,20], lithographic methods.[21] and the most common approach, breath figure method.[22]

Breath figure happens in our daily life, such the fog that appears on a window when we breathe on it. This is also the origin of the name “breath figure”. Inspired by this natural phenomenon, scientists cast polymer solution on a substrate and blow humid air on it. A recent review by Zhang *et al* discussed the history and status of literature on this method in detail.[23]

Due to the evaporation of the solvent, the solution surface turns cold so that humid vapor condenses into water microdroplets which self-assemble due to Magnus effect and sink into the solution gradually. After the complete evaporation of solvent as well as the water droplets that spontaneously condensed at the air-solution interface, honeycomb films with controlled porous structures could be obtained on the substrate (**Figure 1a**).[24]

Thanks to the breath figure method, honeycomb films with customizable microporous structures, including spherical, hemispherical, cylindrical or mushroom-like microstructures could be conveniently manufactured in a large scale.[23,25–27] Besides the pore shape, a number of reports have been published on pore size control by adjusting experimental conditions such as temperature, polymer concentration and volume.[28] For instance, my previous research successfully prepared size-controllable pores as well as ordered spindle pores by stretching honeycomb films (**Figure 1b**), providing a solid base for the further research in this thesis.[24]

The breath figure method is an efficient and cheap method to fabricate honeycomb films. However, many functional materials of interest are not suitable to be directly used in this process. Therefore, some researchers have used the honeycomb film, which provides various types of pore shape, as a template to direct the synthesis of other materials with ordered structures.[29–31] In my previous research, inspired by the compound eyes of bees displaying hierarchic micro/nano-structure, I induced silica nanoparticles to self-assembly inside the honeycomb film and then pour polydimethylsiloxane (PDMS) which leads to a super-hydrophobic flexible film (**Figure 1c**).[24]

Though considerable efforts have been devoted to using honeycomb films as templates for hard materials, there is no related research on preparing microstructured biomaterials or soft microparticles. As mentioned, current honeycomb molding procedure requires calcination or organic solvents which are not feasible for biologics. Therefore, evolution of the molding method needs to be addressed for our interest, designing microstructures on protein/phage hydrogels, and eventually becoming a generic method for all soft biomaterials.

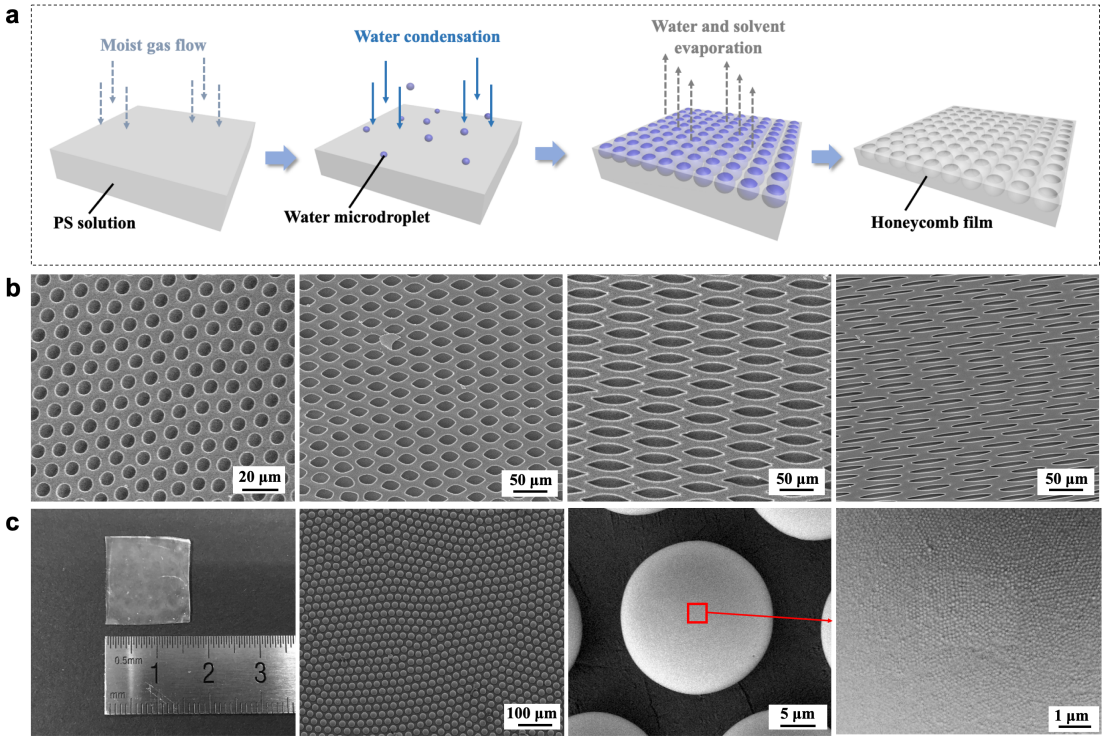

Figure 1. The preparation of honeycomb films and casting microstructured PDMS films. a. Schematic of breath figure method to produce honeycomb films. **b.** Different shapes of micropores honeycomb films. **c.** Hierarchical microbumps on PDMS films using honeycomb films as templates. Figure adapted with permission from reference,[24] copyright 2018 John Wiley and Sons.

1.2 Thesis objectives

This thesis aims to develop a versatile platform of microstructured protein and viral materials. Several novel biomaterial-friendly techniques such as molding-peeling method and critical point drying-induced shrinkage method are established to accomplish the following goals (**Figure 2**):

1. **To prepare hierarchical microbumps on protein hydrogels** as antifouling surface. To date, techniques for structuring hydrogel surfaces are limited to either lengthy preparation process or expense. Designing a cheap and efficient way to produce tunable microstructures on the surface of hydrogels, especially protein hydrogels, is therefore of significance.
2. **To produce phage-exclusive and phage-protein hybrid microgels** via a newly-designed high-throughput templating method without heat and organic solvents. Microgels offer distinct advantages over bulk material because they offer larger surface area and thus more contact points for phage with contaminating bacteria, as well as enhanced flow properties in suspensions, allowing for delivery via spray or injection, all of which make them a more versatile option for effective delivery for biocontrol.
3. **To construct three-level hierarchically wrinkled phage microdots** via a novel pressure-induced substrate-shrinkage method. This method in particular is beneficial for preserving sophisticated biofunctional structures of biomaterials, which could efficiently maintain the biological functions of produced wrinkled materials.

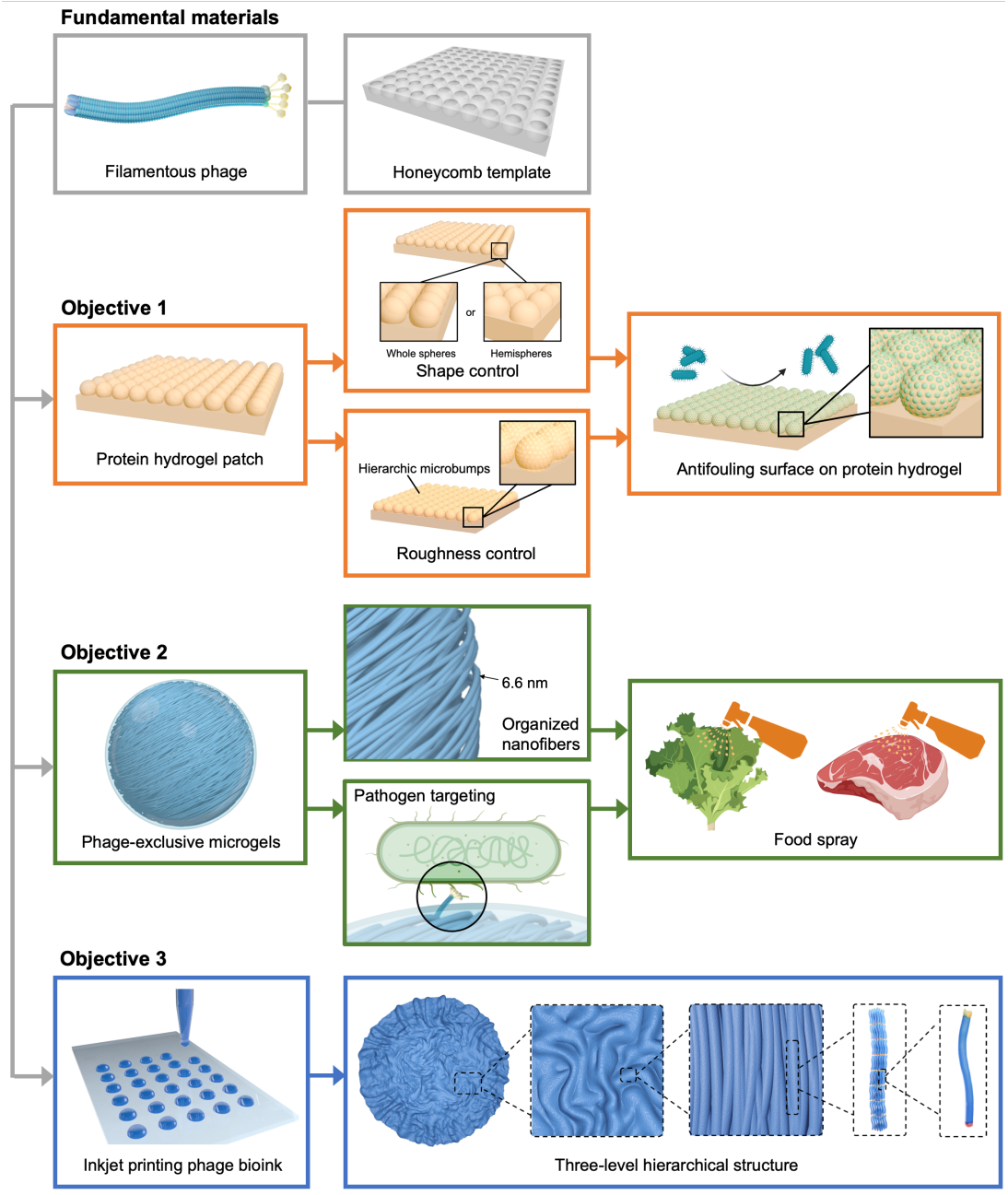

Figure 2. Research objectives, investigated properties and accomplished applications in the thesis. Objective 1. Honeycomb template is firstly used to create microstructured protein gels with controllable shape and roughness. It is the foundation of extending this method for phages because of the similar proteinous gelation mechanism. **Objective 2.**

Honeycomb template method is further adjusted and combined with phage gelation to prepare phage-built microgels. **Objective 3.** Based on the more understanding of phage organization in microgels, inkjet printing is induced to fabricate phage microgels as well. In addition, a new biomaterial-friendly shrinkage method is established to further create three-level hierarchial wrinkle pattern on these microgels.

1.3 Thesis outline

Chapter 1 - Introduction and Objectives

This chapter briefly introduces the background and objectives of the project, and provides a brief overview of research details in each chapter.

Chapter2 - Literature Review: Bacteriophage-Built Gels as Platforms for Biomedical Applications

This chapter provides a critical review on the development, properties and applications of bacteriophage-built gels. The motivation and challenges of using bacteriophages as building blocks are also discussed. This chapter is based on the review paper that has been accepted in *The Canadian Journal of Chemical Engineering, special issue on celebration of advances in chemical engineering*.

Chapter 3 - Bacteria repellent protein hydrogel decorated with tunable, isotropic, nano-on-micro hierarchic microbump array

This chapter reports the fabrication of microbumps on protein hydrogels utilized honeycomb templates. The control of sphericity and roughness of microbumps is investigated. Eventually, nano-on-micro hierarchical structures are produced on protein hydrogels as antifouling surfaces. The work has been published in *Chemical Communications*.

Chapter 4 - Self-Assembling Nanofibrous Viral Microgels as Sprayable Antimicrobials Targeting Multidrug-Resistant Bacteria

Using techniques developed in the previous chapter, this chapter demonstrates the preparation of self-assembled bacteriophage microgels for preservation and delivery of a high titer of bacterial viruses. The nanostructure and tunable fluorescence of viral microgels are further explored. It also demonstrates the strong antimicrobial potency of these microgels when implemented as a patch or a spray. The work is under peer review in *Nature Communications*.

Chapter 5 - Printed Viral Microdot Arrays with Tunable Three-Level Hierarchically Wrinkle Morphology as Biosensing Chips

This chapter explores the designing of microstructures on viral materials without the assist of templates. A new substrate-shrinkage method is established to create wrinkled morphology on phage microdots. The effect of phage concentration and volume on the wrinkle patterns are determined. In addition, the three-level hierarchical geometry of the microdots explored. The work is in preparation to be submitted to *Nature Nanotechnology*.

Chapter 6 – Conclusions and Future Direction

This chapter summarizes the main contributions of this thesis. It also discusses future works and challenges towards developing a more comprehensive platform of microstructured viral materials.

1.4 References

1. Hamley, I. W. & Castelletto, V. Biological soft materials. *Angewandte Chemie - International Edition* **46**, 4442–4455 (2007).
2. Hamley, I. W. Nanotechnology with Soft Materials. *Angewandte Chemie* **115**, 1730–1752 (2003).
3. Miyata, T., Asami, N. & Uragani, T. A reversibly antigen-responsive hydrogel. *Nature* **399**, 766–768 (1999).
4. Khoury, L. R., Slawinski, M., Collison, D. R. & Popa, I. Cation-induced shape programming and morphing in protein-based hydrogels. *Science Advances* **6**, 1–7 (2020).
5. Souza, G. R. *et al.* Three-dimensional tissue culture based on magnetic cell levitation. *Nature Nanotechnology* **5**, 291–296 (2010).
6. Peivandi, A., Tian, L., Mahabir, R. & Hosseinidoust, Z. Hierarchically Structured, Self-Healing, Fluorescent, Bioactive Hydrogels with Self-Organizing Bundles of Phage Nanofilaments. *Chemistry of Materials* **31**, 5442–5449 (2019).
7. Xing, Y. *et al.* Self-assembled DNA hydrogels with designable thermal and enzymatic responsiveness. *Advanced Materials* **23**, 1117–1121 (2011).
8. Zou, J. *et al.* Highly Efficient and Environmentally Friendly Fabrication of Robust, Programmable, and Biocompatible Anisotropic, All-Cellulose, Wrinkle-Patterned Hydrogels for Cell Alignment. *Advanced Materials* **31**, 1–8 (2019).
9. de France, K. J. *et al.* 2.5D Hierarchical Structuring of Nanocomposite Hydrogel Films Containing Cellulose Nanocrystals. *ACS Applied Materials and Interfaces* **11**, 6325–6335 (2019).
10. Jackson, K., Peivandi, A., Fogal, M., Tian, L. & Hosseinidoust, Z. Filamentous Phages as Building Blocks for Bioactive Hydrogels. *ACS Applied Bio Materials* **4**, 2262–2273 (2021).
11. Peivandi, A. *et al.* Inducing Microscale Structural Order in Phage Nanofilament Hydrogels with Globular Proteins. *ACS Biomaterials Science and Engineering* **8**, 340–347 (2022).
12. Kim, J., Lew, B. & Kim, W. S. Facile fabrication of super-hydrophobic nano- needle arrays via breath figures method. 1–8 (2011).
13. Li, Z., Zhang, Z., Kong, Q. & Ren, X. Adhesive and repulsive properties of water droplet impact on honeycomb surfaces through breath figure method. **45476**, 1–6 (2017).
14. Yabu, H. *et al.* Stretchable, transparent and molecular permeable honeycomb electrodes and their hydrogel hybrids prepared by the breath figure method and sputtering of metals. *RSC Adv* **5**, 88414–88418 (2015).

15. Chen, P., Wan, L., Ke, B. & Xu, Z. Honeycomb-Patterned Film Segregated with Phenylboronic Acid for Glucose Sensing. *Langmuir* **27**, 12597–12605 (2011).
16. Gong, J., Xu, B. & Tao, X. Breath Figure Micromolding Approach for Regulating the Microstructures of Polymeric Films for Triboelectric Nanogenerators. *ACS Appl Mater Interfaces* **9**, 4988–4997 (2017).
17. Zhang, L. & Li, X. Facile preparation of honeycomb-structured TiO2 nanofilm via breath figures assembly and coffee ring effect. *Materials Letters* **227**, 74–77 (2018).
18. Zhang, Y., Ding, H. & Wei, S. Hierarchical macroporous epoxy resin templated from single semi-fluorinated surfactant. *Journal of Porous Materials* **17**, 693–698 (2010).
19. Parker, I. D. *et al.* Conjugated Polymer Inverse Opals for Potentiometric Biosensing. 1837–1841 (2002).
20. Hong, B. J., Park, J., Chun, C. & Kim, D. Photoinduced Tuning of Optical Stop Bands in Azopolymer Based Inverse Opal Photonic Crystals. *Advanced Functional Materials* **17**, 2462–2469 (2007).
21. Campbell, M., Sharp, D. N., Harrison, M. T. & Denning, R. G. Fabrication of photonic crystals for the visible spectrum by holographic lithography. **404**, 53–56 (2000).
22. Widawski, G. & Rawiso, M. Self-organized honeycomb morphology of star-polymer polystyrene films. *Nature* **369**, 387–389 (1994).
23. Zhang, A., Bai, H. & Li, L. Breath Figure: A Nature-Inspired Preparation Method for Ordered Porous Films. *Chem Rev* **115**, 9801–9868 (2015).
24. Zhu, C., Tian, L., Liao, J., Zhang, X. & Gu, Z. Fabrication of Bioinspired Hierarchical Functional Structures by Using Honeycomb Films as Templates. *Advanced Functional Materials* **28**, 1–8 (2018).
25. Daly, R., Sader, J. E. & Boland, J. J. Taming Self-Organization Dynamics to Dramatically Control Porous Architectures. *ACS Nano* **10**, 3087–3092 (2016).
26. Ponnusamy, T., Chakravarty, G., Mondal, D. & John, V. T. Novel " Breath Figure " -Based Synthetic PLGA Matrices for In Vitro Modeling of Mammary Morphogenesis and Assessing Chemotherapeutic Response. *Advanced healthcare materials* **3**, 703–713 (2014).
27. Wang, W. *et al.* Deterministic Reshaping of Breath Figure Arrays by Directional Photomanipulation. *ACS Applied Materials & Interfaces* **9**, 4223–4230 (2017).
28. Takehiro Nishikawa *et al.* Fabrication of Honeycomb Film of an Amphiphilic Copolymer at the Air−Water Interface. *Langmuir* **18**, 5734–5740 (2002).
29. Miller, S. & Bao, Z. Fabrication of flexible pressure sensors with microstructured polydimethylsiloxane dielectrics using the breath figures method. *Journal of Materials Research* **30**, 3584–3594 (2015).
30. Li, X. *et al.* A Bottom-Up Approach To Fabricate Patterned Surfaces with Asymmetrical TiO2 Microparticles Trapped in the Holes of Honeycomblike Polymer Film. *J Am Chem Soc* **113**, 3736–3739 (2011).
31. Kim, B. S., Kim, W. J., Kim, Y. do & Huh, D. S. Silver Immobilization on Honeycomb-patterned Polyvinypyrrolidone thin Films via an Electroless Process. **32**, 4221–4226 (2011).

Chapter 2: Literature Review: Bacteriophage-Built Gels as Platforms for Biomedical Applications

This chapter serves as a unique and valuable resource for engineers and chemists that are interested in using bacteriophages, but may not be equipped to navigate the literature in the field. Although phages are being heavily investigated for their use in the biomedical sector (both as therapeutics and for diagnostics/biosensing), they have remained obscure to most scientists in other fields. In addition, there is a translation gap when it comes to using the information provided by phage microbiologists for real life applications, a gap that we strived to address in this chapter.

This chapter is based on the review paper that has been accepted in *The Canadian Journal of Chemical Engineering, special issue on celebration of advances in chemical engineering*. Lei Tian performed the literature review, data gathering and wrote the initial draft of the review paper with help from Kyle Jackson, Amy Zhang, Zeqi Wan and Ahmed Saif under supervision of Dr. Zeinab Hosseinidoust. All text and figures are reproduced/adapted with permissions from John Wiley and Sons.

Bacteriophage-Built Gels as Platforms for Biomedical Applications

Lei Tian, Kyle Jackson, Amy Zhang, Zeqi Wan, Ahmed Saif, Zeinab Hosseinidoust

The Canadian Journal of Chemical Engineering, **2022**, *in press*.

2.1 Abstract

Bacteriophages, or phages (bacterial viruses), have seen a resurgence in their applications following the emergence of antimicrobial-resistant superbugs that pose enormous risks to human health and food supplies. Phages present numerous advantages over conventional small-molecule antibiotics, including that they are highly selective bacteria-killers and demonstrate low inherent cytotoxicity to human health. Notwithstanding the direct therapeutic applications of these innate bacteria-killing viruses, they have also garnered attention as biological nanoparticles. Due to the diversity in sizes and shapes of phages, self-replicating capacity, geometrical batch-to-batch consistency, and ease of synthetic modifications, phages are excellent building blocks for creating bioactive biomaterial platforms. In this review, we provide a brief history of the development of phage-based materials and identify key stakeholders who are driving innovation in this space. In addition, we explore various phage-based gel structures and provide critical analysis of how their structures produce distinct advantageous properties that can be exploited for applications in solving challenges in biomedical engineering.

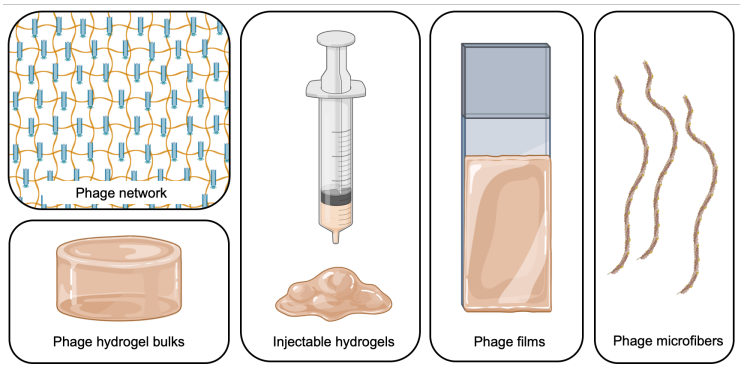

Graphic abstract. Phage-crosslinked network and diverse types of phage-based gels including phage hydrogel bulks, injectable hydrogels, phage films and phage microfibers.

2.2 Introduction

2.2.1 Phage research

Viruses are obligate cellular parasites that can hijack a living cell and use its machinery to create progeny that will, in turn, infect more cells. On the planet, there are many forms of viruses that can infect different types of cells. A large subset of the viral population are bacteriophages (phages), which are viruses that are solely capable of infecting bacteria.[1,2] Phages are among the biosphere's most common and diverse entities.[3] It is estimated that there are more than 10^{31} phages on the planet.[3,4]

Phages have been used for a wide variety of purposes. Historically, they have been used as alternative antimicrobial agents in the former Soviet Union and Central Europe.[4] Shortly after being formally discovered independently by Frederick Twort and Felix d'Herelle in the early 20th century, both men proposed using them to treat infections.[5] d'Herelle, a French-Canadian microbiologist then working out of the Institute Pasteur in Paris, France, actively sponsored clinical trials to assess the therapeutic capacity of these bacteria-killing machines.[5,6] At the onset of The Great War, d'Herelle and his colleagues actively formulated millions of doses of phage-based therapeutics for allied military units.[6] Years after The Great War concluded, phage therapy became mainstream globally. d'Herelle traveled to Tbilisi, Georgia, where he co-founded the Eliava Institute, which is considered a world-leading center for phage therapy and still serves patients to this day.[6,7]

2.2.2 Phage in the context of the challenge of drug-resistant superbugs in Canada

Phages were seldom used in Western countries after the advent of antibiotics.[8] This was due to several reasons but notably stemming from a limited understanding of phage

biology,[9] a lack of large-scale randomized clinical trials supporting the efficacy of phage,[10] poor uncontrolled science in clinical setting,[10] unreliable and inconsistent phage manufacturing practices,[10] and political tensions brewing between Western powers and the Soviet Union.[11] Despite these historical barriers, phages have seen a resurgence in popularity due to the onset of emerging crises such as climate change and antimicrobial resistance (AMR).[12] Both crises are driving the emergence of new pathogens that can evade conventional therapeutic interventions that Western healthcare systems have depended on for decades.[12] In response, we have seen a surge in the number of compassionate use cases employing phages to treat AMR infections in the United States and Europe, which have resulted in dozens of clinical success stories.[13] Likewise, Canada has also seen a rise in phage research in general and phage biocontrol research in particular and continues to be a global leader in the space. Of note is the Université Laval, which houses the Felix d'Herelle Reference Library for Bacterial Viruses, the only phage repository in the country and one of the largest in the world.[14]

AMR is a current global threat and is presently felt by Canadians. In 2018, it was reported that one in 180 patients admitted to a hospital in Canada was the result of an AMR-associated infection.[15] Of those patients admitted due to AMR infections, it was further reported that one in five patients died.[15] The Council of Canadian Academics independently reported in 2018 that an estimated 14,000 Canadian deaths could be indirectly attributed to AMR infections.[16] Between 2019 and 2020, prior to the SARS-CoV-2 pandemic, there were approximately 3 million acute inpatient hospitalizations in Canada.[17] This would mean that an estimated 3,000 Canadian deaths could be directly attributed to AMR

infections. Key drivers that are contributing to this growing problem, whether that be in Canada or globally, include clinical misuse,[18] biological evolution,[18] societal, political, and economic pressures,[19,20] and climate change.[18–21] The cumulation of these drivers disseminates into human and animal populations, creating a feedback loop inflicting more pressure on the drivers and exacerbating the root causes of the issue.[21]

Aside from the considerable healthcare burden inflicted on Canada, the economic consequences of AMR will be equally devastating. A 2019 report found that AMR cost the Canadian healthcare system $1.4 billion in 2018.[16] If current resistance rates continue, then by 2050, associated healthcare expenditure will reach $120 billion per annum.[16] Likewise, AMR continues to have a distinct impact on our economy. AMR reduced Canada's GDP by an estimated $2 billion in 2018, and if resistance rates persist, the economy could lose between $13 and $21 billion per year by 2050.[16]

Accompanying the growing AMR crisis in Canada, reports have also indicated increased rates of foodborne pathogens.[22] According to a report published by Thomas *et al.* in 2013, it is estimated that 4 million Canadians suffer episodes of domestically acquired foodborne illnesses.[23] Thomas *et al.* further reported that in 2015, the combined estimate of 30 specified and unspecified foodborne pathogens accounted for approximately 11,632 hospitalizations and 238 deaths related to domestically acquired foodborne illness in Canada.[22] Bacterial foodborne pathogens associated with the highest rates of hospitalizations and deaths include nontyphoidal *Salmonella* spp., *Campylobacter* spp., verotoxin-producing *Escherichia coli* (VTEC) O157, and *L. monocytogenes*. These pathogens differ from those that cause the greatest proportion of non-hospitalized related

illnesses, which make up the bulk of reported cases, including *C. perfringens* and *Bacillus cereus*.[22] Although there is no silver bullet for tackling AMR, bacteriophages offer hope as an alternative antimicrobial when last resort antibiotics fail, as demonstrated by high-profile cases in the US.[24] It has also been proposed that dual-treatment combining antibiotics and phages can achieve better bactericidal efficiency.[25–29] Therefore, phage-composed materials offer a mode of preservation and delivery for such applications and are thus the urgent investigating targets.

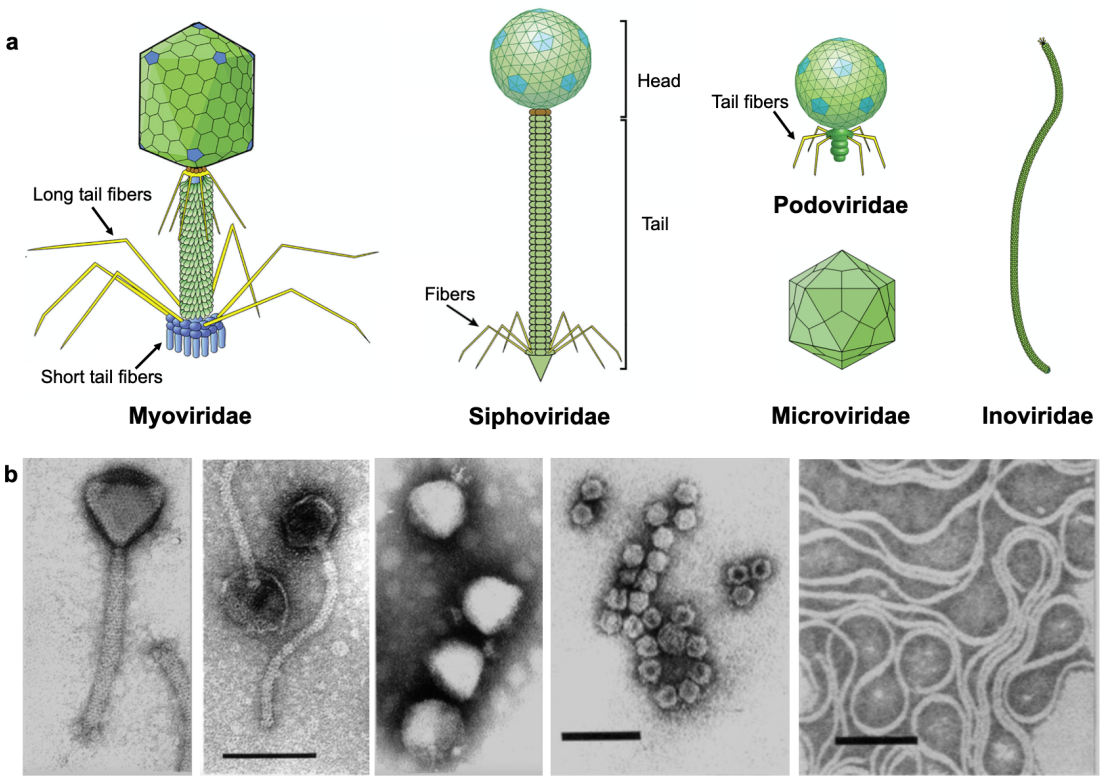

Figure 1. Diverse shape and size of bacteriophages. a, Schematics of different shapes of phages: Myoviridae, Siphoviridae, Podoviridae, Microviridae and Inoviridae (adapted from other studies[50]). **b,** TEM images of corresponding types of phages. Scale bar: 100 nm (adapted from other studies[51]).

2.2.3 What do phages offer in addition to antimicrobial activity?

In more recent years, phages have been explored in other contexts aside from their natural antimicrobial capabilities. They are excellent nanoparticles for constructing nanomaterials based on the following properties:

(1) Diverse size and shape: Phages have an enormous diversity of physical structures, both shape, and sizes.[30] They are either icosahedral, filamentous, or head-tail in shape, and their size can vary from a few nanometers to over one micrometer (**Fig. 1**). It provides abundant options to design phage-built materials according to the aiming structures and applications.

(2) Sophisticated inner structure: The protein arrangement on the phage capsids is remarkably intricate. For example, M13 filamentous phages are chiral colloidal particles where the major coat proteins arrange with helical symmetry.[31] This special structure contributes to the unique optical properties of phage-built hydrogels, which will be emphasized later.

(3) Self-replication. As mentioned, phages can infect host bacteria and self-propagate. The isolation and purification procedure of phages are well-developed.[32]

(4) Consistency: Phages maintain the same shape and size during self-replication.[33]

(5) Stability: phages can maintain their infectivity and structures in appropriate ambient conditions for years without degradation.[34–37]

(6) Ease of modification: The modification of phages has been well-developed in two strategies, including genetic modification to display peptides[38] and chemical conjugation

to bind small molecules.[39–43] In fact, the modification of phages significantly expands the functions of phage materials which will be illustrated later.

(7) Self-organization: Filamentous phages are rod-shaped viruses that have the capacity to self-assemble at high concentrations creating hierarchical macro-structures.[44–46] These macro-structures are based on the formation of liquid crystalline formations that displays unique optical properties that expand the functionality of these bioactive materials.

(8) Excellent biocompatibility: Phages and phage-composed materials were found to have great biocompatibility.[47–49]

Therefore, phages can be regarded as powerful building blocks with unique properties for material synthesis.

2.2.4 History of phage hydrogels

Herein, we focus on the hydrogels where phages are a structural component, known as phage-built gels. Compared to phage-encapsulated hydrogels[52–57], phages in these phage-built hydrogels play an important role in the nanostructures in addition to potential antimicrobial capability. Multiple labs have made significant contributions to the development of phage-built gels in diverse directions, as shown in **Fig. 2**. Crosslinking phages was first reported by Dr. George Smith in 1998.[58] Since then, the Pasqualini lab at the University of Texas reported phage-built hydrogel bulks and macro-spheres for cell culture and drug delivery.[59–61] The Belcher lab at MIT proposed the phages microfibers and films as optical and electrical devices.[62–65] The Zhang lab at Nankai University reported the injectable hydrogels.[66,67] Meanwhile, the Serizawa lab from the Tokyo Institute of Technology focused on the optical properties of phage hydrogel bulks.[68–71] Since 2019, our

team at McMaster University has fabricated pure phage hydrogels and microgels for antimicrobial applications.[44–46] The details of these works will be discussed in the following sections.

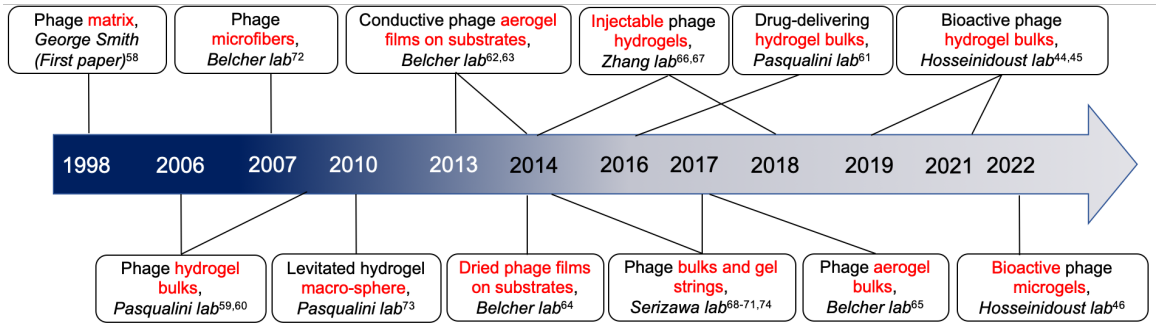

Figure 2. Development of phage-based gels since 1998 when phage gels were proposed for the first time.

2.3 Preparation of phage-built gels

2.3.1 Phage gel materials

Numerous combinations of phage modification and crosslinking mechanisms have been tested (**Table. 1**). In general, filamentous phages, M13, *fd*, f8 phages in particular, are the most common building materials which employ a unique combination of individual interactions (*e.g.,* hydrogen bonding, steric hydration, electric double layer, van der Waals, cation–π, and hydrophobic interactions) with themselves in order to construct crosslinked networks.[72–74] Moreover, all three types of phage are closely related in regards to their morphology and target host, *Escherichia coli.* Given the similarities, these three phages can undergo non-covalent bonding with each other, giving rise to hybrid materials with applications in target-specific drug delivery, bioimaging, and biosensing systems, among many others.[75–78] Of the three types of filamentous phage, M13 is the most popular and

well-studied. This virion is approximately 900 nm in length and comprised of five coat proteins: pVIII (p8), pIX (p9), pVII (p7), pIII (p3), and pVI (p6),[79–81] all of which play critical roles in its self-assembly of larger macro-, micro-, and nanostructures.[81] Additionally, all five of these proteins are readily modifiable, increasing the versatility of M13, making them highly convenient nanoparticles.

As for the crosslinker, the most common options are Au nanoparticles, glutaraldehyde, and 1-ethyl-3-(3-dimethylaminopropyl)carbodiimide (EDC), which provide different crosslinking mechanisms. Au nanoparticles connected phages through charges[60] or Au-binding peptides.[82] Glutaraldehyde reacts with the amide groups on phage capsids, while EDC induces the reaction between amide groups and carboxyl groups on phage capsids.[46,64]

Table 1. Phage materials and corresponding crosslinkers to construct phage-built gels.

Phage	Phage modification	Crosslinker
M13	- None [44–46,62,64,65,71]	- Glutaraldehyde,[44–46,62] EDC,[46,64] physical-crosslinked gelatin,[71] and physical bond formation (van der Waals)[65]
	- Displaying antigen on PIII [68–70]	- Gold nanoparticles (with antibodies),[68–70] and physical-crosslinked gelatin[69]
	- Displaying gold-binding peptides [82]	- Au nanoparticles (citrate-capped)
	- Displaying a peptide extension that carried a higher positive charge on pVIII[60]	- Au nanoparticles (negative charge)
	- Engineered to be glutamate-rich[83]	- Glutaraldehyde
	- FTIC-labeled [84]	- Glutaraldehyde
	- Displaying RGD [85]	- Au nanoparticles and magnetic iron oxide
	- Binding gold nanoparticles [62]	- Glutaraldehyde
	- Genetically modified to bind carbon nanotubes[60]	- Glutaraldehyde
	- Conjugated with Ruthenium and cobalt ferrite[65]	- Physical bond formation (van der Waals)
	- Conjugated with phenylboronic acid derivative [66,67]	- Self-crosslink, [66] multiple Diol-Containing Polymers[67]
	- Grafted with cyclodextrin [86]	- Azobenzene-modified hyaluronan
fd	- None [58,59,61]	- NHS-dextran, [58] Au nanoparticles [59,61]
	- Displaying RGD on pIII [59]	- Au nanoparticles
f88	- Displaying the guest peptide NH 2-PTEWCPPHRTCWPTT on pIII[58]	- NHS-dextran
Gli27	- f8 phage displaying ELRGDSLP peptide[87]	- NHS-dextran

2.3.2 Preparation of phage bulk hydrogel and aerogels

Through bottom-up assembly, phage hydrogel bulks can easily form in vials or syringes (**Fig. 3a-c**).[44,60,70] Pasqualini's lab connected positive-charged *fd* phages and negative-charged Au nanoparticles to construct phage bulks. It was innovative to use this physical

crosslinking mechanism to fabricate phage gels. Serizawa's lab utilized Au nanoparticles to crosslink phages but with a different mechanism. The Au nanoparticles were conjugated with antibodies to connect phages displaying the corresponding antigen. Meanwhile, Chen *et al.*[86] used a well-studied photosensitive molecule, azobenzene, to crosslink M13 phages. Consequently, the gelation of those phage bulks is reversible, given its responsiveness to light and chemicals. It is worth mentioning that they compared M13 phage bulks with the gels composed of tobacco mosaic virus. M13 phage with a higher aspect ratio and more flexible structure reportedly led to a much more robust hydrogel. Furthermore, our lab reported free-standing phage hydrogel bulks using M13 phages and glutaraldehyde. One small tip to isolate phage gels easily is employing plastic syringes as containers instead of glass vials. The gels can be extruded out after cutting the tip end of the syringes, which maintains the gel shapes (if the gels are rigid enough to hold the shape).

Zhang's lab presented that phage hydrogels can be injected out effortlessly from syringes (**Fig. 3d**).[66,67] Multiple diol-containing agents, such as poly(vinyl alcohol), induced fast gelation of the M13 phages modified phenylboronic acid. The extruded phage matrix is maintained in the gel shape and can be molded into diverse shapes, providing more formats of phage gels.

In addition to hydrated status, the phage hydrogel bulks can also be easily made through freeze-drying (**Fig. 3e**).[65] These aerogels provide a free-standing scaffold to load inorganic materials, which will be discussed in the application section.

Interestingly, phages can also form macroscale spheres aside from the traditional bulk shape of hydrogels (**Fig. 3f**).[85] Pasqualini's lab further added magnetic iron oxide to the

hydrogel system and used a magnetic field to induce the formation of spheres composed of phage gels and cells. It provided an excellent combination of phages and magnetic nanoparticles.

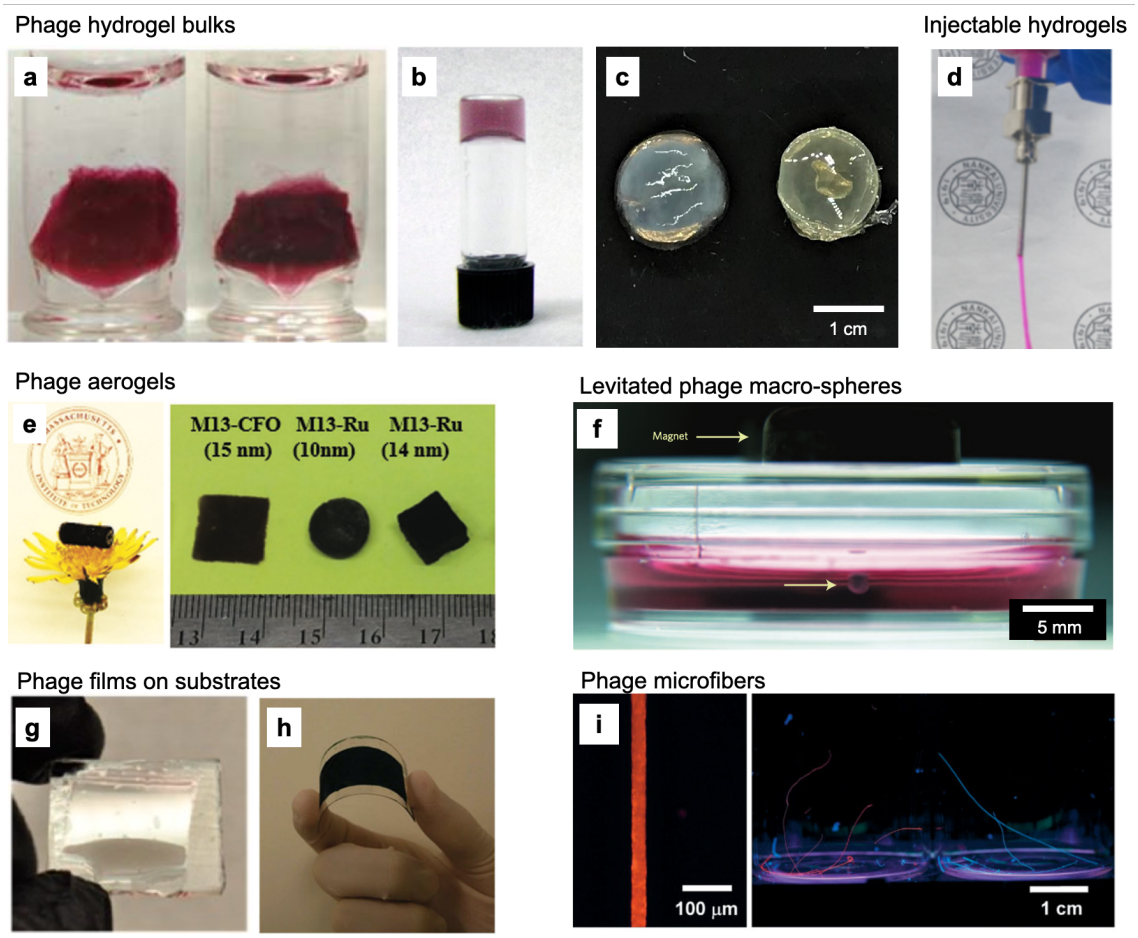

Figure 3. Different phage gel products. a-c, Phage hydrogel bulks (adapted from other studies[44,60,70]). **d,** Injectable hydrogels (adapted from other studies[67]). **e,** Independent phage aerogels (adapted from other studies[65]). **f,** Levitated phage macro-spheres encapsulating magnetic nanoparticles (adapted from other studies[85]). **g-h,** Phage films on the substrates (adapted from other studies[62,63]). **i,** Phage microfibers (adapted from other studies[83]).

2.3.3 Preparation of phage films

Compared to independent hydrogel bulks, constructing phage films on the substrates required different preparation strategies. Belcher's lab reported three different phage films based on two methods (**Fig. 3g-h**). In the first method,[62,63] a small amount of phage suspension (pure phage or mixing with Au nanoparticles) was dropped on plasma-treated glass substrates, which were subsequently immersed in the crosslinker solution (50% glutaraldehyde). After the 2-hour gelation process, the hydrogels on the films were transferred to an acidic environment to remove excessive crosslinker. In the second method,[64] the substrates were first dipped into EDC to activate the carboxylic acid groups and then dipped into a phage solution to form amide bonds. Layers of crosslinked phages were formed while repeating the dipping procedure. The structures and functionalities of the phage films will be illustrated in the later sections.

2.3.4 Preparation of microscale phage gels

Belcher's lab fabricated phage microfibers by injecting M13 phage suspension into a crosslinker solution (0.5% - 10% glutaraldehyde), as shown in **Fig. 3i**.[83] Interestingly, these microfibers' mechanical toughness and strength were comparable to synthetic polymer fibers. This work proved that filamentous phages could be combined with current fibril and woven-mesh manufacturing processes, enabling as new structure for biology devices. Since then, phages have been incorporated with Au nanoparticles,[82] conductive polymers[88] and cellulose[89,90] to obtain functional fibers.

Another important microscale product, phage microgel, was newly proposed by our lab.[46] The preparation of these soft microgels is much more challenging than preparing

macroscale phage hydrogel bulks. The common environments of microparticle preparation (such as UV, organic solvents, and heat) would de-active phages and jeopardize the antimicrobial applications of the produced microgels.[91–95] We designed a new biomaterial-friendly method to fabricate phage microgels. Microporous films were applied as the mold to produce microgels at a large scale without organic solvent or heat. Accordingly, our lab reported pure phage microgels, each composed of millions of M13 phage nanofilaments, as a virus-exclusive microparticle platform.[46] In addition to pure phage microgels, our lab also fabricated hybrid phage microgels. It is worth mentioning that the hybrid microgels we discuss here still use phages as the main building materials.[46] Bovine serum albumin (BSA) added into the phage microgels was to enhance the mechanical properties and assist in the preservation of phage bioactivity. The detailed properties and applications of these soft microgels will be discussed later.

2.4 Properties of phage-built gels

2.4.1 Nanostructure

2.4.1.1 Liquid crystal structures

Filamentous phages can create hierarchical biomaterials that are in part due to the formation of liquid crystals.[96] Liquid crystals are a special state of matter that can display properties of both the liquid and solid states. For instance, a liquid crystal may flow like a liquid, but its molecules may be oriented in a crystal-like pattern.[97] The fluid-like crystal structures seen in liquid crystals are the optimal environment for birefringent properties to be observed.[98] As a result, the types of colour formations seen by liquid crystals are highly dependent on the ordered nano- and micro-structures, which are dictated by the material

building blocks. In the context of M13 bacteriophages, they can form lyotropic liquid crystals with three main subtypes: nematic, cholesteric, or smectic, leading to a special optical property, birefringence.[97,99,100]

Birefringence is an optical property of a material having a refractive index that depends on the polarization and propagation direction of light.[98,101] It is defined as the difference between the minimum and maximum indexes of refraction within a material. Birefringence is best observed when a material is observed under a polarized light microscope and is often used as an indicator to confirm the presence of liquid crystalline structures within larger macrostructures.

Work conducted in our lab has investigated the formation of hydrogels using M13 bacteriophages. [44,45] We have investigated the parameters influencing the formation of filamentous phage-based hydrogels with a crosslinking agent alone[44] or in the presence of globular proteins such as bovine serum albumin.[45] In both studies, birefringence was observed in the larger gels, confirming the highly organized self-assembled liquid crystals. Furthermore, it was found that the addition of globular proteins can influence M13 phages to self-assemble into ordered nanostructures at concentrations 50,000-fold lower than they otherwise would naturally.[45]

Further research from the Serizawa Lab combined filamentous phages with gold nanoparticles alongside the crosslinking agent glutaraldehyde to form hybrid hydrogels. When observing the structure under a polarized light microscope, the researchers reported birefringent optical properties confirming the presence of lyotropic liquid crystalline structures.[82] Here, they reported the successful formation of liquid crystalline structures at

filamentous phage concentrations 1000-fold lower than they would otherwise form naturally.[82] Moreover, the observation of birefringent properties was used to confirm the formation of phage-gelatin-based hydrogels for the purposes of controlled drug release into surrounding environments.[69] Researchers in the Zhang Lab further reported the presence of birefringent properties in their injectable phage-based hydrogels and confirmed that the resulting optical intensity is dependent on the concentration of viral nanoparticles.[67]

2.4.1.2 Highly-porous structures

Phage gels exhibit highly-porous morphologies, which make them of keen interest to some researchers when compared to the uniform morphology seen in liquid crystal structures. The phage films from Belcher's lab exhibited unordered porous nanostructure which was formed from rapid crosslinking.[62,63] This morphology still provided a powerful template for the nucleation of nanoparticles and nanowire meshes.

2.4.2 Fluorescence

Our lab reported the fluorescence of phage hydrogels among all excitation channels (**Fig. 4a-b**).[44] It is worth mentioning that the fluorescent signal was generated by the crosslinking reactions without any additional components. When the UV-vis spectrum of the M13 phage suspension and the M13 phage hydrogels were compared, the hydrogel displayed a new, relatively broad peak around 310nm.[44] To further determine the chemical changes in the hydrogel, Fourier transform infrared (FTIR) spectra of the hydrogel were analyzed and compared to the M13 suspension.[44] The hydrogel exhibited amide II (~1570 cm^{-1}) and amide III bonds (~1280 cm^{-1}) because of glutaraldehyde reacting with proteins and peptides. Further spectrometry revealed the M13 hydrogels to exhibit autofluorescence

when excited at specific wavelengths. Distinct peaks appeared when the hydrogel was excited at λ=470 nm and λ=598 nm. In comparison, the spectrums for glutaraldehyde, water, and M13 phage suspension did not exhibit the same peaks. Microscopy had also confirmed autofluorescence of the hydrogels as the gels fluoresced blue, green, and red with optical filter sets (ex/em 358/461 nm, ex/em = 498/509 nm, ex/em = 598/615 nm), whereas when the same filters sets were used on M13 phage suspensions or glutaraldehyde, fluorescence did not appear. Although the results from both spectrometry and microscopy suggested the presence of a fluorescent molecule/ functional group due to M13 cross-linking with glutaraldehyde, the functional group could not be resolved by FTIR. However, the fluorescence observed has been estimated by our lab to be attributed in part to the electronic transitions that take place, such as the π−π* transition of the C=C bond in glutaraldehyde and n−π* transition of C=N bonds in the Schiff's base, which is the result of the reaction that occurs between α,β-unsaturated aldehyde polymers in glutaraldehyde and M13 surface proteins.[44] Our lab has also concluded that the nature of the autofluorescence may depend on various factors, including the type of protein that reacts with glutaraldehyde, the size of the protein/ peptide, and the pH of the reaction. This variance offers a versatile method to prepare hydrogels for imaging applications.

However, fluorescence needs to be avoided for certain application scenarios, such as biosensing, where background fluorescence would disrupt the signal. Therefore, our lab also used EDC for phage gelation with different chemical reactions.[46] Consequently, the phage gels showed much lower fluorescence than those made with glutaraldehyde. The tunable fluorescence provides flexible options for phage gels in optical applications.

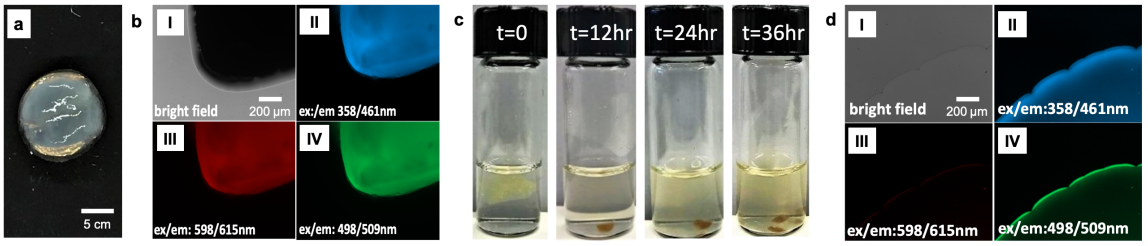

Figure 4. Fluorescence and degradation of phage hydrogels crosslinked by glutaraldehyde (adapted from other studies[44]). **a,** Picture of a phage hydrogel. **b,** Bright field and fluorescent images of phage hydrogels. **c,** Degradation of the phage hydrogel in proteinase K solution in 36 hrs. **d,** Bright field and fluorescent images of the degradation product of phage hydrogels.

2.4.3 Degradation

The degradation of phage hydrogels was monitored in proteinase K solution (**Fig. 4c**).[44] M13 phage hydrogels were digested for 36 hrs at 37 °C with a 1mg/mL solution of proteinase K. The solution turned yellow, the same color as the hydrogels, and also exhibited autofluorescence (**Fig. 4d**). However, fluorescence was not observed in the red channel. Proteinase K hydrolyzes amine bonds and breaks the ester bond formation process to track color changes. Since red autofluorescence (ex/em 598/618) was no longer observed in the degradation product, biodegradation of hydrogels could be tracked in tissue engineering applications. An advantage of using the M13 phage hydrogels in biological models is that the degradation products could be tracked in other channels while degradation is being tracked in the red channel.

2.4.4 Swelling property

Hydrogels developed using both M13 phage and Bovine serum albumin (BSA), or hybrid M13-BSA hydrogels, exhibited a significantly larger swelling ratio (~14 times their dry weight) when compared to BSA hydrogels (~4 times their dry weight).[45] Further decreasing the BSA concentration of these hydrogels from 3% to 1% resulted in an even higher swelling ratio of ~15 times their dry weight. These results suggest a possible change in the pore structure of the hydrogels in the presence of BSA.[45] Upon comparing the pore structure of hybrid M13-BSA (3%) hydrogels with BSA hydrogels of the same concentration of BSA, it was determined that the hybrid M13-BSA hydrogels have a finer pore structure (~45 μm) in contrast to BSA hydrogels (~200 μm).[45]

Observations obtained from our lab indicate that an increase in cross-linking density of M13 results in a decrease in the M13 hydrogel swelling ratio.[44] When comparing two hydrogels prepared with differing concentrations, the hydrogels made with 3×10^{13} PFU/mL M13 possessed the highest swelling ratio of 16 times their dry weight, while the hydrogels made with 3×10^{14} PFU/mL M13 only absorbed 11 times their dry weight.[44] Our lab also observed a decrease in the swelling ratio (from 13 times to 10 times) at temperatures other than room temperature (~25 °C).[45]

2.4.5 Biocompatibility and cytotoxicity

The cytotoxicity and biocompatibility of phage hydrogels are critical for their medical and antimicrobial applications. Chen *et al*.[86] performed cytotoxicity evaluation of the two hydrogel components (azobenzene-modified hyaluronan and M13 phages grafted with cyclodextrin) on fibroblast cells. There was no observable decrease in cell viability, proving the ideal cytocompatibility of these phage gels. Similar excellent biocompatibility

was verified for M13-Au hydrogels as well.[59,61,85] As to another common crosslinker, glutaraldehyde, there were concerns about whether it affects the biocompatibility of produced phage gels considering its potential toxicity. However, it has been proved that glutaraldehyde-crosslinked phage hydrogels showed no toxicity to the cells.[84] Meanwhile, additional side evidence illustrates the safety of glutaraldehyde-crosslinked phage hydrogels. Protein-based hydrogels crosslinked by glutaraldehyde were also non-cytotoxic both *in vitro* and *in vivo*.[102]

Although the biocompatibility of these gels with human cells has previously been extensively proved, this characteristic in phage hydrogels made with other crosslinkers (such as EDC) is still understudied. Further clinical studies should be conducted to specific applied phages and crosslinkers. Moreover, removing excessive crosslinkers should be an essential step in designing preparation protocols of phage hydrogels.[46]

2.4.6 Self-healing

Zhang's labs had demonstrated self-healing characteristics in PBA-M13 hydrogels with Poly (vinyl alcohol).[67] PBA-M13 suspensions and solutions of PVA in a phosphate buffer (5mM) with pH 7.4 were gently vortexed to facilitate mixing. Results from a time-dependent oscillatory rheology characterization revealed that the hydrogel self-heals right after mixing, which is given by the fact that the elastic modulus (G') and loss modulus (G") become constant and G' is much higher than G".[67] The instant gelation and self-healing properties of the hydrogel occur at physiological pH, which is attributed to the lower pKa of the tailored PBA moieties.

Moreover, our lab investigated the self-healing ability of M13+glutaraldehyge hydrogels.[44] The M13 hydrogels that were cut with a razor blade exhibited repetitive self-healing when incubated at room temperature and put in the presence of Ca^{2+} or phosphate-buffered saline (PBS).[44] The hydrogels were able to completely fuse back together in 24 hours for $CaCl_2$ and 47 hours for PBS. The re-fused hydrogels showed a lower compression modulus (~4.4 and ~6.1) than the intact hydrogels (~9.0), suggesting compromised mechanical strength, which may be due to scars present on the gels as a result of fusion. This self-healing property of M13 hydrogels can be due to the reformation of Schiff's bases, assisted by M13/calcium interactions. The residual aldehydes may be reacting with the amines or re-reacting with new lysins on M13. Since M13 hydrogels heal under physiological calcium concentration, these hydrogels may exhibit similar self-healing properties to biological tissues.

Hybrid M13-BSA hydrogels were observed to exhibit a similar behaviour at room temperature.[45] BSA can be physically cross-linked in the presence of Ca^{2+}, which may explain the self-healing property of our hybrid M13-BSA hydrogels. However, the protein must first be heated to thermally unfold the native BSA protein.

The phage hydrogels composed of M13 phages and gold nanoparticles from Serizawa's lab were also found to self-heal.[68] When comparing the strength of the original hydrogels with the self-healed hydrogel using indentation tests, the original hydrogel required 55 mN for rupture, and the self-healed gel required 45 mN. As the rupture forces are similar, it can be concluded that the hydrogels exhibit self-healing capabilities.[68] Transmission electron

microscopy of the hydrogels before and after self-healing of the rupture points revealed that HA-GNP networks were similar in both scenarios.[68]

2.5 Applications of phage-built gels

2.5.1 Antimicrobial applications

Phage gels are expected to inherit the antimicrobial property of their building blocks, which could be a unique advantage of using phages to construct materials. However, the antimicrobial properties of phage-built gels have scarcely been reported. We think that two main reasons impeded the related research: 1. Our lab found out that the gelation process caused detriments to the bioactivity of phages which might be related to intramolecular crosslinking on the bacteria-binding sites on phage capsids.[46] 2. Some reported preparation methods of phage gels utilized a very high concentration of crosslinkers,[62,63] acid[63], or organic solvents[67], which further aggravated the denaturation of phages. The loss of bioactivity did not affect the proposed biological-irrelevant applications, but it needs to be aware that these methods are not feasible for obtaining bioactive phage hydrogels.

We have found that the hydrogel bulks can still exhibit strong bioactivity because of the high integration of phages (over 10^{13} PFU/cm^3) within.[44] Therefore, macroscale phage bulks can be designed as wound dressings and implant coatings, considering the excellent biocompatibility and low cytotoxicity of phage gels.

Moreover, the phage microgels our lab produced were applied as antimicrobial food spray.[46] This is a unique application scenario for microscale particles where macroscale hydrogel bulks are not feasible. Multiple types of lytic phages were encapsulated into M13 phage microgels to enhance their antimicrobial range and efficiency in order to kill

different pathogens in two distinct food matrices (lettuce and meat bulks). Meanwhile, the hydrous environment in the microgels protected these desiccation-sensitive phages. It was found that hybrid phage microgels decreased the concentration of drug-resistant *E. coli* O157:H7 to below the detection limit (100 CFU/g). The design of phage microgels expanded the applications of phage gels into the food industry.

2.5.2 Template

Aside from antimicrobial ability, another unique property where phages contributed to the composed gels was the inner nanostructures, as we mentioned above. The high surface area of obtained phage hydrogels and films made them excellent candidates as templates to coat or load functional components. The phage films on the substrates from Belcher's lab were designed as a multifunctional and three-dimensional scaffold to load Au nanoparticles and TiO_2 and form nanowire-based photoanodes.[62] This structure enhanced electron diffusion length and improved light harvesting. Furthermore, similar phage films can be applied to bind carbon nanotubes and polyaniline to improve electrical conductivity and electrochemical performance.[63] In the meantime, the phage films can be loaded with gold nanoparticles and quantum dots for optical applications.[64] These composite systems presented the templating ability of phage films.

2.5.3 Three-dimensional cell culture

Cell cultures are an *in vitro* tool used to improve our perception and understanding of cell biology. Three-dimensional cultures have continued to gain attention in drug discovery and development studies, as two-dimensional cultures prove to poorly imitate the conditions *in vivo*.[85] These three-dimensional cell-based assays are a useful tool to help evaluate the

potency of new compounds, and as such, they have been incorporated in disease modeling, target validation, screening, and toxicity assessment.

Previously, a three-dimensional tissue culture was designed based on the magnetic levitation of cells in the presence of gold, magnetic iron oxide nanoparticles, and filamentous bacteriophage-containing hydrogels.[85] The results indicated that magnetically levitated human glioblastoma cells showed similar protein expression profiles to human tumour xenografts. Since three-dimensional tissue cultures quite accurately mimic biological conditions, hydrogels may be immensely useful in future clinical and experimental applications.

2.5.4 Other applications

Phage gels have also exhibited a strong loading capacity of drugs and cells. The hydrogels from Zhang's lab were sugar responsive which led to a glucose-regulated release of insulin.[67] Chen *et al.* reported reversible gelation of phage hydrogels for cell culture and release.[86] Last but not least, Serizawa's lab demonstrated the controllable antibody release from the phage hydrogel matrices.[69]

2.6 Conclusion

In conclusion, various phage-built gels, including hydrogel bulks, spheres, films, microfibers, and microgels, have been established to build a powerful viral material platform. The phage gels exhibited abundant interesting properties, such as bactericidal, birefringence, fluorescence, and self-healing. Consequently, the phage gels have been used as antimicrobial food spray, templates, cell culture substrates, and biosensors. It is noteworthy that all these hydrogels were made with filamentous phages. Other types of

phages, such as tailed phages and spherical phages, can be explored. The challenge is that it will require a higher concentration of phage because they do not form networks as easily as nanofilaments. However, it could potentially bring different nanostructures and optical properties. Finally, another important future direction of phage hydrogels can center on expanding the crosslinkers library, which potentially brings the gels more environmental responses. We believe that phage will play an increasingly vital role as multifunctional bio-nanoparticles in addition to antimicrobial agents.

2.7 References

1. Clokie, M. R. J., Millard, A. D., Letarov, A. V. & Heaphy, S. Phages in nature. *Bacteriophage* **1**, 31–45 (2011).
2. Ul Haq, I., Chaudhry, W. N., Akhtar, M. N., Andleeb, S. & Qadri, I. Bacteriophages and their implications on future biotechnology: A review. *Virology Journal* vol. 9 9 (2012).
3. Canchaya, C. A., Ventura, M. & van Sinderen, D. Bacteriophage Bioinformatics and Genomics. in *Bacteriophage: Genetics and Molecular Biology* (eds. Mc Grath, S. & van Sinderen, D.) 43–59 (Caister Academic Press, 2007).
4. Novel Phage Therapy Saves Patient with Multidrug-Resistant Bacterial Infection. https://health.ucsd.edu/news/releases/Pages/2017-04-25-novel-phage-therapy-saves-patient-with-multidrug-resistant-bacterial-infection.aspx.
5. Félix d' Hérelle | Canadian microbiologist | Britannica. https://www.britannica.com/biography/Felix-d-Herelle.
6. Summers, W. C. Félix Hubert d'Herelle (1873–1949): History of a scientific mind. *Bacteriophage* **6**, e1270090 (2016).
7. Kutateladze, M. INSIGHT Experience of the Eliava Institute in bacteriophage therapy. *VIROLOGICA SINICA* **30**, 80–81 (2015).
8. Żaczek, M., Weber-Dąbrowska, B., Międzybrodzki, R., Łusiak-Szelachowska, M. & Górski, A. Phage Therapy in Poland – a Centennial Journey to the First Ethically Approved Treatment Facility in Europe. *Frontiers in Microbiology* **11**, 1056 (2020).
9. Wittebole, X., de Roock, S. & Opal, S. M. A historical overview of bacteriophage therapy as an alternative to antibiotics for the treatment of bacterial pathogens. *Virulence* **5**, 226 (2014).
10. Aswani, V. H. & Shukla, S. K. An Early History of Phage Therapy in the United States: Is it Time to Reconsider? *Clinical Medicine & Research* **19**, 82 (2021).
11. Summers, W. C. The strange history of phage therapy. *Bacteriophage* **2**, 130 (2012).
12. Burnham, J. P. Climate change and antibiotic resistance: a deadly combination. *Ther Adv Infect Dis* **8**, 2049936121991374 (2021).
13. McCallin, S., Sacher, J. C., Zheng, J. & Chan, B. K. Current State of Compassionate Phage Therapy. *Viruses* **11**, (2019).
14. Phage banks around the world. https://phage.directory/capsid/phage-banks#article.
15. Canadian Antimicrobial System Report Resistance Surveillance.
16. Council of Canadian Academies | CCA | When Antibiotics Fail. https://cca-reports.ca/reports/the-potential-socio-economic-impacts-of-antimicrobial-resistance-in-canada/.
17. Hospital stays in Canada | CIHI. https://www.cihi.ca/en/hospital-stays-in-canada.
18. Holmes, A. H. *et al.* Understanding the mechanisms and drivers of antimicrobial resistance. *The Lancet* **387**, 176–187 (2016).
19. Klein, E. Y. *et al.* Global increase and geographic convergence in antibiotic consumption between 2000 and 2015. *Proceedings of the National Academy of Sciences* **115**, E3463–E3470 (2018).
20. Rousham, E. K., Unicomb, L. & Islam, M. A. Human, animal and environmental contributors to antibiotic resistance in low-resource settings: integrating behavioural,

epidemiological and One Health approaches. *Proceedings of the Royal Society B: Biological Sciences* **285**, (2018).
21. Vikesland, P. *et al.* Differential Drivers of Antimicrobial Resistance across the World. (2019) doi:10.1021/acs.accounts.8b00643.
22. Thomas, M. K. *et al.* Estimates of Foodborne Illness-Related Hospitalizations and Deaths in Canada for 30 Specified Pathogens and Unspecified Agents. *Foodborne Pathogens and Disease* **12**, 820–827 (2015).
23. Thomas, M. K. *et al.* Estimates of the burden of foodborne illness in Canada for 30 specified pathogens and unspecified agents, Circa 2006. *Foodborne Pathogens and Disease* **10**, 639–648 (2013).
24. Schooley, R. T. *et al.* Development and use of personalized bacteriophage-based therapeutic cocktails to treat a patient with a disseminated resistant Acinetobacter baumannii infection. *Antimicrobial Agents and Chemotherapy* **61**, (2017).
25. Nouraldin, A. A. M., Baddour, M. M., Harfoush, R. A. H. & Essa, S. A. M. Bacteriophage-antibiotic synergism to control planktonic and biofilm producing clinical isolates of Pseudomonas aeruginosa . *Alexandria Journal of Medicine* **52**, 99–105 (2016).
26. Jo, A., Kim, J., Ding, T. & Ahn, J. Role of phage-antibiotic combination in reducing antibiotic resistance in Staphylococcus aureus. *Food Science and Biotechnology* **25**, 1211–1215 (2016).
27. Valério, N. *et al.* Effects of single and combined use of bacteriophages and antibiotics to inactivate Escherichia coli. *Virus Research* **240**, 8–17 (2017).
28. Uchiyama, J. *et al.* Piperacillin and ceftazidime produce the strongest synergistic phage–antibiotic effect in Pseudomonas aeruginosa. *Archives of Virology* **163**, 1941–1948 (2018).
29. Coulter, L. B., McLean, R. J. C., Rohde, R. E. & Aron, G. M. Effect of bacteriophage infection in combination with tobramycin on the emergence of resistance in Escherichia coli and Pseudomonas aeruginosa biofilms. *Viruses* **6**, 3778–3786 (2014).
30. Jackson, K., Peivandi, A., Fogal, M., Tian, L. & Hosseinidoust, Z. Filamentous Phages as Building Blocks for Bioactive Hydrogels. *ACS Applied Bio Materials* **4**, 2262–2273 (2021).
31. Chung, W. J. *et al.* Biomimetic self-templating supramolecular structures. *Nature* **478**, 364–368 (2011).
32. Luong, T., Salabarria, A. C., Edwards, R. A. & Roach, D. R. Standardized bacteriophage purification for personalized phage therapy. *Nature Protocols* **15**, 2867–2890 (2020).
33. Brödel, A. K., Jaramillo, A. & Isalan, M. Intracellular directed evolution of proteins from combinatorial libraries based on conditional phage replication. *Nature Protocols* **12**, 1830–1843 (2017).
34. Leung, V. *et al.* Long-Term Preservation of Bacteriophage Antimicrobials Using Sugar Glasses. *ACS Biomaterials Science and Engineering* **4**, 3802–3808 (2018).
35. Leung, V., Groves, L., Szewczyk, A., Hosseinidoust, Z. & Filipe, C. D. M. Long-Term Antimicrobial Activity of Phage-Sugar Glasses is Closely Tied to the Processing Conditions. *ACS Omega* **3**, 18295–18303 (2018).
36. Dixon, D. v., Hosseinidoust, Z. & Tufenkji, N. Effects of environmental and clinical interferents on the host capture efficiency of immobilized bacteriophages. *Langmuir* **30**, 3184–3190 (2014).

37. Jabrane, T. & Griffiths, M. W. *Towards a commercial production of phage-based bioactive paper*. *J-FOR Journal of Science & Technology for Forest Products and Processes* vol. 1 https://www.researchgate.net/publication/261615346 (2011).
38. Smith, G. P. & Petrenko, V. A. Phage Display. *Chem Rev* **97**, 391–410 (1997).
39. Bernard, J. M. L. & Francis, M. B. Chemical strategies for the covalent modification of filamentous phage. *Frontiers in Microbiology* vol. 5 (2014).
40. Bar, H., Yacoby, I. & Benhar, I. Killing cancer cells by targeted drug-carrying phage nanomedicines. *BMC Biotechnology* **8**, 1–14 (2008).
41. Yacoby, I., Bar, H. & Benhar, I. Targeted drug-carrying bacteriophages as antibacterial nanomedicines. *Antimicrobial Agents and Chemotherapy* **51**, 2156–2163 (2007).
42. Ju, Z. & Sun, W. Drug delivery vectors based on filamentous bacteriophages and phage-mimetic nanoparticles. *Drug Delivery* vol. 24 1898–1908 (2017).
43. Suthiwangcharoen, N. *et al.* M13 bacteriophage-polymer nanoassemblies as drug delivery vehicles. *Nano Research* **4**, 483–493 (2011).
44. Peivandi, A., Tian, L., Mahabir, R. & Hosseinidoust, Z. Hierarchically Structured, Self-Healing, Fluorescent, Bioactive Hydrogels with Self-Organizing Bundles of Phage Nanofilaments. *Chemistry of Materials* **31**, 5442–5449 (2019).
45. Peivandi, A. *et al.* Inducing Microscale Structural Order in Phage Nanofilament Hydrogels with Globular Proteins. *ACS Biomaterials Science & Engineering* In press (2021).
46. Tian, L. *et al.* Self-Assembling Nanofibrous Viral Microgels as Sprayable Antimicrobials Targeting Multidrug Resistant Bacteria. *Submitted to Nature Communications* **NCOMMS-22-00018A-Z**, (2022).
47. Li, Y. *et al.* Selectively Suppressing Tumor Angiogenesis for Targeted Breast Cancer Therapy by Genetically Engineered Phage. *Advanced Materials* **32**, (2020).
48. Zheng, X., Liu, W., Liu, Z., Zhao, Y. & Wu, C. Biocompatible and Rapid Cyclization of Peptides with 2,4-Difluoro-6-hydroxy-1,3,5-benzenetricarbonitrile for the Development of Cyclic Peptide Libraries. *Bioconjugate Chemistry* **31**, 2085–2091 (2020).
49. Lee, D. Y. *et al.* Phage as versatile nanoink for printing 3-D cell-laden scaffolds. *Acta Biomaterialia* **29**, 112–124 (2016).
50. Zuppi, M., Hendrickson, H. L., O'Sullivan, J. M. & Vatanen, T. Phages in the Gut Ecosystem. *Frontiers in Cellular and Infection Microbiology* **11**, (2022).
51. Ackermann, H. W. Bacteriophage Electron Microscopy. in *Advances in Virus Research* vol. 82 1–32 (Academic Press Inc., 2012).
52. Yan, W. *et al.* Development of thermosensitive hydrogel wound dressing containing Acinetobacter baumannii phage against wound infections. *International Journal of Pharmaceutics* **602**, (2021).
53. Barros, J. A. R. *et al.* Encapsulated bacteriophages in alginate-nanohydroxyapatite hydrogel as a novel delivery system to prevent orthopedic implant-associated infections. *Nanomedicine: Nanotechnology, Biology, and Medicine* **24**, (2020).
54. Fu, W. *et al.* Bacteriophage cocktail for the prevention of biofilm formation by Pseudomonas aeruginosa on catheters in an in vitro model system. *Antimicrobial Agents and Chemotherapy* **54**, 397–404 (2010).

55. Kaur, P., Gondil, V. S. & Chhibber, S. A novel wound dressing consisting of PVA-SA hybrid hydrogel membrane for topical delivery of bacteriophages and antibiotics. *International Journal of Pharmaceutics* **572**, (2019).
56. Zhang, J. *et al.* Bioactive multi-engineered hydrogel offers simultaneous promise against antibiotic resistance and wound damage. *International Journal of Biological Macromolecules* **164**, 4466–4474 (2020).
57. Meireles Gouvêa Boggione, D., Boggione Santos, I. J., Menezes de Souza, S. & Santos Mendonça, R. C. Preparation of polyvinyl alcohol hydrogel containing bacteriophage and its evaluation for potential use in the healing of skin wounds. *Journal of Drug Delivery Science and Technology* **63**, (2021).
58. Smith, G. P., Petrenko, V. A. & Matthews, L. J. Cross-linked filamentous phage as an affinity matrix. *Journal of Immunological Methods* **215**, 151–161 (1998).
59. Souza, G. R. *et al.* Networks of gold nanoparticles and bacteriophage as biological sensors and cell-targetting agents. *Proc Natl Acad Sci U S A* **103**, 1215–1220 (2006).
60. Souza, G. R. *et al.* Bottom-up assembly of hydrogels from bacteriophage and Au nanoparticles: The effect of Cis- and trans-acting factors. *PLoS ONE* **3**, 1–5 (2008).
61. Hosoya, H. *et al.* Integrated nanotechnology platform for tumor-targeted multimodal imaging and therapeutic cargo release. *Proceedings of the National Academy of Sciences* **113**, 1877–1882 (2016).
62. Chen, P. Y. *et al.* Versatile three-dimensional virus-based template for dye-sensitized solar cells with improved electron transport and light harvesting. *ACS Nano* **7**, 6563–6574 (2013).
63. Chen, P. Y. *et al.* Assembly of viral hydrogels for three-dimensional conducting nanocomposites. *Advanced Materials* **26**, 5101–5107 (2014).
64. Courchesne, N. M. D. *et al.* Assembly of a bacteriophage-based template for the organization of materials into nanoporous networks. *Advanced Materials* **26**, 3398–3404 (2014).
65. Jung, S. M., Qi, J., Oh, D., Belcher, A. & Kong, J. M13 Virus Aerogels as a Scaffold for Functional Inorganic Materials. *Advanced Functional Materials* **27**, 1603203 (2017).
66. Cao, J., Liu, S., Chen, Y., Shi, L. & Zhang, Z. Polymer Chemistry Synthesis of end-functionalized boronic acid containing copolymers and their bioconjugates with rod-like viruses for multiple responsive. *Polymer Chemistry* **5**, 5029–5036 (2014).
67. Zhi, X. *et al.* Nanofilamentous Virus-Based Dynamic Hydrogels with Tunable Internal Structures, Injectability, Self-Healing, and Sugar Responsiveness at Physiological pH. *Langmuir* **34**, 12914–12923 (2018).
68. Sawada, T. & Serizawa, T. Antigen-Antibody Interaction-Based Self-Healing Capability of Hybrid Hydrogels Composed of Genetically Engineered Filamentous Viruses and Gold Nanoparticles. *Protein & Peptide Letters* **25**, 64–67 (2017).
69. Sawada, T., Yanagimachi, M. & Serizawa, T. Controlled release of antibody proteins from liquid crystalline hydrogels composed of genetically engineered filamentous viruses. *Materials Chemistry Frontiers* **1**, 146–151 (2017).
70. Sawada, T., Kang, S., Watanabe, J., Mihara, H. & Serizawa, T. Hybrid Hydrogels Composed of Regularly Assembled Filamentous Viruses and Gold Nanoparticles. *ACS Macro Letters* **3**, 341–345 (2014).

71. Sawada, T., Otsuka, H., Yui, H. & Serizawa, T. Preparation and characterization of hybrid hydrogels composed of physically cross-linked gelatin and liquid-crystalline filamentous viruses. *Polymer Bulletin* **72**, 1487–1496 (2015).
72. Johnson, E. R. *et al.* Revealing Noncovalent Interactions. *J Am Chem Soc* **132**, 6498–6506 (2010).
73. Dougherty, D. A. Cation-π interactions in chemistry and biology: A new view of benzene, Phe, Tyr, and Trp. *Science (1979)* **271**, 163–168 (1996).
74. Cosic, I. Macromolecular Bioactivity: Is It Resonant Interaction Between Macromolecules?—Theory and Applications. *IEEE Transactions on Biomedical Engineering* **41**, 1101–1114 (1994).
75. Park, J. *et al.* Polydopamine-Based Simple and Versatile Surface Modification of Polymeric Nano Drug Carriers. *ACS Nano* **8**, 3347–3356 (2014).
76. Meng, H. M. *et al.* Aptamer-integrated DNA nanostructures for biosensing, bioimaging and cancer therapy. *Chemical Society Reviews* vol. 45 2583–2602 (2016).
77. Shin, Y. C. *et al.* Cell-adhesive RGD peptide-displaying M13 bacteriophage/PLGA nanofiber matrices for growth of fibroblasts. *Biomaterials Research* **18**, 14 (2014).
78. Ghosh, D. *et al.* M13-templated magnetic nanoparticles for targeted in vivo imaging of prostate cancer. *Nature Nanotechnology* **7**, 677–682 (2012).
79. Marvin, D. A. Filamentous phage structure , infection and assembly. 150–158 (1998).
80. Fukunaga, K. & Taki, M. Practical tips for construction of custom peptide libraries and affinity selection by using commercially available phage display cloning systems. *Journal of Nucleic Acids* vol. 2012 (2012).
81. Loh, B., Kuhn, A. & Leptihn, S. The fascinating biology behind phage display: filamentous phage assembly. *Molecular Microbiology* vol. 111 1132–1138 (2019).
82. Sawada, T. *et al.* Regular assembly of filamentous viruses and gold nanoparticles by specific interactions and subsequent chemical crosslinking. *Polymer Journal* **46**, 511–515 (2014).
83. Chiang, C. Y. *et al.* Weaving genetically engineered functionality into mechanically robust virus fibers. *Advanced Materials* **19**, 826–832 (2007).
84. Kashiwagi, K. & Shiba, K. Filamentous phage-based extra cellular matrix. *2008 International Symposium on Micro-NanoMechatronics and Human Science, MHS 2008* 392–395 (2008) doi:10.1109/MHS.2008.4752484.
85. Souza, G. R. *et al.* Three-dimensional tissue culture based on magnetic cell levitation. *Nature Nanotechnology* **5**, 291–296 (2010).
86. Chen, L., Zhao, X., Lin, Y., Su, Z. & Wang, Q. Dual stimuli-responsive supramolecular hydrogel of bionanoparticles and hyaluronan. *Polymer Chemistry* **5**, 6754–6760 (2014).
87. Samoylova, T. I. *et al.* Phage matrix for isolation of glioma cell membrane proteins. *Biotechniques* **37**, 254–260 (2004).
88. Niu, Z., Bruckman, M. A., Harp, B., Mello, C. M. & Wang, Q. Bacteriophage M13 as a scaffold for preparing conductive polymeric composite fibers. *Nano Research* **1**, 235–241 (2008).
89. Anany, H. *et al.* Print to detect: a rapid and ultrasensitive phage-based dipstick assay for foodborne pathogens. *Analytical and Bioanalytical Chemistry* **410**, 1217–1230 (2018).

90. Jabrane, T., Jeaidi, J., Dubé, M. & Mangin, P. J. Gravure Printing of Enzymes and Phages. *Advances in Printing and Media Technology* **35**, 279–288 (2008).
91. Schmitt, C. *et al.* Internal structure and colloidal behaviour of covalent whey protein microgels obtained by heat treatment. *Soft Matter* **6**, 4876–4884 (2010).
92. Phan-Xuan, T. *et al.* On the crucial importance of the ph for the formation and self-stabilization of protein microgels and strands. *Langmuir* **27**, 15092–15101 (2011).
93. Nicolai, T. Formation and functionality of self-assembled whey protein microgels. *Colloids and Surfaces B: Biointerfaces* **137**, 32–38 (2016).
94. Brugger, B. & Richtering, W. Magnetic, thermosensitive microgels as stimuli-responsive emulsifiers allowing for remote control of separability and stability of oil in water-emulsions. *Advanced Materials* **19**, 2973–2978 (2007).
95. An, H. Z., Helgeson, M. E. & Doyle, P. S. Nanoemulsion composite microgels for orthogonal encapsulation and release. *Advanced Materials* **24**, 3838–3844 (2012).
96. Sawada, T. & Serizawa, T. Filamentous viruses as building blocks for hierarchical self-assembly toward functional soft materials. *Bulletin of the Chemical Society of Japan* vol. 91 455–466 (2018).
97. 23.3: Liquid Crystals - Chemistry LibreTexts. https://chem.libretexts.org/Bookshelves/General_Chemistry/Map%3A_Principles_of_Modern_Chemistry_(Oxtoby_et_al.)/UNIT_6%3A_MATERIALS/23%3A_Polymeric_Materials_and_Soft_Condensed_Matter/23.3%3A_Liquid_Crystals.
98. Wu, S. T. Birefringence dispersions of liquid crystals. *Physical Review A* **33**, 1270–1274 (1986).
99. Purdy, K. R. & Fraden, S. Influence of charge and flexibility on smectic phase formation in filamentous virus suspensions. *Physical Review E - Statistical, Nonlinear, and Soft Matter Physics* **76**, 011705 (2007).
100. Sawada, T. Filamentous virus-based soft materials based on controlled assembly through liquid crystalline formation. *Polymer Journal* **49**, 639–647 (2017).
101. NEWTON, R. H., HAFFEGEE, J. P. & HO, M. W. Polarized light microscopy of weakly birefringent biological specimens. *Journal of Microscopy* **180**, 127–130 (1995).
102. Ma, X. *et al.* A Biocompatible and Biodegradable Protein Hydrogel with Green and Red Autofluorescence: Preparation, Characterization and in Vivo Biodegradation Tracking and Modeling. *Scientific Reports* **6**, 1–12 (2016).

Chapter 3: Bacteria repellent protein hydrogel decorated with tunable, isotropic, nano-on-micro hierarchic microbump array

In this chapter, we focus on designing a new method to address the challenges (cost and efficiency) on creating microstructures on protein hydrogels. Multiple microstructures were controllably achieved. As to our knowledge, this is the first report of an antifouling protein hydrogel. Meanwhile, It builds the foundation of the next chapter where honeycomb templates are extended to making microgels composed of phages with proteinous capsid.

In this chapter, experiments were performed by Lei Tian and two undergraduate researchers, Leon He and Kyle Jackson. All data was analyzed by Lei Tian. The chapter was drafted by Lei Tian and subsequently edited by the academic supervisor, Dr. Zeinab Hosseinidoust. This chapter and the supporting information are reprinted as they appear in *Chemical Communications*, with permission from the Royal Society of Chemistry.

Bacteria repellent protein hydrogel decorated with tunable, isotropic, nano-on-micro hierarchic microbump array

Lei Tian, Leon He, Kyle Jackson, Randi Mahabir, Zeinab Hosseinidoust

Chemical Communications, **2021**, 57(*83*), p. 10883-10886.

https://doi.org/10.1039/D1CC03741B.

3.1 Abstract

We report the development of ordered shape-controllable microbump structures on protein hydrogels using polystyrene honeycomb templates. Addition of protein nanogels results in the formation of hierarchical nano-on-micro structures and increases surface hydrophilicity over 55%, exhibiting bacteria repellency 100 times stronger than a flat hydrogel surface composed of the same protein.

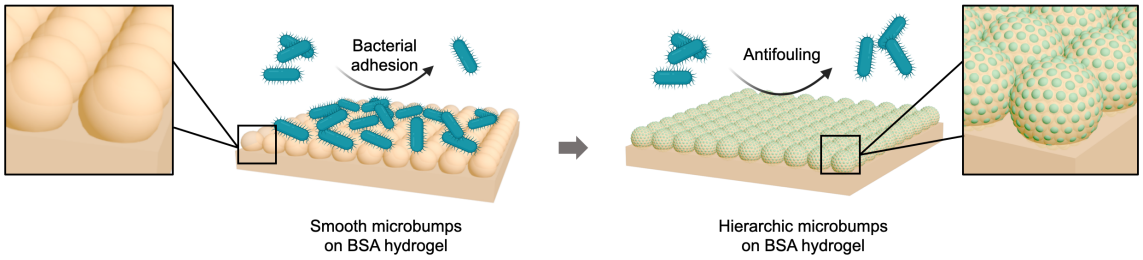

Graphic abstract. Antifouling hierarchical microbumps on BSA hydrogels are fabricated by inducing homogeneous nanogels inside the microbumps. The resulting hierarchical surface exhibits bacteria repellency 100 times stronger than a flat hydrogel surface or a reverse-microbump structure.

3.2 Introduction

Substrates with nano-on-micro hierarchical structures have demonstrated superior performance for applications in biosensing,[1] hard tissue implants,[2] and clotting/fouling mitigation,[3] owing partially to the increase in surface area and change in surface energy. For most biomedical applications, where the structured substrate interfaces living tissue, there is increasing evidence that the stiffness of the bio-interface can affect the intracellular molecular processes of cells such as regulation of gene expression and protein secretion, which could in turn impact physiological processes such as tissue regeneration or even

response to drugs.[4] Hydrogels have thus become very popular for biomedical applications because of their hydrated, soft, and flexible nature,[5] which can be tuned to closely resemble that of living tissue. Motivated by the performance boost observed in hard materials, recent attempts on applying hierarchical nano-on-micro structures to hydrogels and microgels have expanded the range of applications of these soft, structured substrates to electrode,[6] tissue engineering scaffolds for regenerative medicine,[7] and microparticles for enhanced inhalable or systemic drug delivery.[8]

Published reports on hydrogels decorated with micro/nanostructure have disproportionately focused on synthetic polymers such as polyethylene glycol[9] and polyoligo(ethylene glycol) methyl ether methacrylate[10]. However, for most biomedical engineering applications, the existing body of literature supports the distinct advantages of protein hydrogels, especially albumin-based hydrogels. Aside from natural biocompatibility, biodegradability, and lack of toxicity from unreacted monomers remained in the gel,[11] albumin-based hydrogels can be designed to specifically interact with the surrounding tissue by inserting sequences associated with promoting cellular adhesion or cell growth.[12] Manufacturing protein hydrogels with hierarchical structure, however, is far from trivial. To date, the only method that has been demonstrated to achieve hierarchical nano-on-micro structures on hydrogels has been the shrinking method. In this method, a thermo-sensitive substrate is heat-shrunk, which in-turn creates wrinkle micropatterns on the hydrogel coated on the substrate.[10] The shrinking method is fairly simple and is not dependent on specialized infrastructure. However, this method cannot be applied to protein hydrogels or polymer hydrogels containing heat-sensitive biological

agents, *e.g.,* proteins, peptides, VLP's (virus like particles), antibodies, or even antibiotics and most drugs. Furthermore, the wrinkles are anisotropic and disordered,[10] which may reduce consistency/reproducibility especially if the substrate were to be used for sensing applications. Alternatively, methods demonstrated for micropatterning a hydrogel might, in principle, be applicable to making hierarchical structures on hydrogels. Photolithography combined with *in situ* photopolymerization is a versatile micropatterning method and allows for design of hydrogel microstructures such as cylinders,[9] stars[13] and shallow dots,[14] but that too is incompatible with proteins and other heat-sensitive molecules. Indirect use of photolithography, namely designing reverse structures on PDMS[15] or using ready-made microfluidic channels (with 3D printing),[16] is in theory compatible with proteins and biological molecules, although no instance of the use of this method has been demonstrated for making hierarchical structures on hydrogels. A simpler, more robust, templating method is the use honeycomb films with ordered micropores as the template. The honeycomb template can be prepared through the breath figure method by exposing a polymer solution to a humid environment,[17] and can provide an ordered array of over 100,000 pores in a 1-cm^2 film.[18] This method has been demonstrated for micropatterning polymeric hydrogels such as P(NIPAAM),[19] or PMMA-PEG hydrogels.[20] As with other methods, the published reports have been entirely focused on synthetic polymers and even there, no hierarchical structuring has been reported.

We developed the breath figure templating technique to create protein hydrogels with hierarchically ordered, isotropic, nano-on-micro structures. Furthermore, our method allows for tunable sphericity and roughness of the microbumps using a single template. We

demonstrated all this with bovine serum albumin (BSA), a water soluble protein which binds drugs or inorganic substances noncovalently,[21] but the method is applicable to any hydrogel with heat-sensitive components. Serum albumin is synthesized by the liver and aids in molecular transport of a variety of metabolites including cholesterols, fatty acids, bilirubin, thyroxine, drugs, and toxins.[22] Hydrogels formed from albumin exhibit numerous desirable properties such as high biocompatibility, cell adherence, autofluorescence, and self-healing.[12] We demonstrate that the BSA hydrogels decorated with the hierarchical microbump arrays are more hydrophilic than smooth microbumps, but exhibit remarkable bacteria repellency, mitigating adhesion of *Staphylococcus aureus* by 100×, which makes our hydrogels a suitable choice for applications prone to bacterial contamination, such as advanced wound care products.

3.3 Results and discussion

Templates of polystyrene honeycomb films were prepared with the static breath figure method (**Fig. 1a**). A stable humid environment (relative humidity≈76%) was established inside a sealed chamber (**Fig. 1a**-i). In the breath figure method, as a result of chloroform evaporation, the surface temperature of a liquid polystyrene film (5 wt% polystyrene, M_w=650 000) drops drastically, resulting in the condensation of water vapor into water microdroplets at the liquid-air interface. The microdroplets then sink into the polystyrene solution and self-assemble. In our experiments, after complete evaporation of water and chloroform, a polystyrene film with a diameter of 2.5 cm was obtained and subsequently peeled off from the glass slide. As shown in **Fig. 1b** (inset), the polystyrene film had a round shape and white opaque color. Scanning electron micrographs showed the film had

micropores with a circular opening, distributed over the film homogeneously at a surface density of 1820 ± 140 pores/mm^2. The average surface pore size of the film was 10.8 ± 0.9 μm (**Fig. 1c**). The internal pore shape was open spheres with the average inside diameter of 23.3 ± 2.8 μm (along the direction of cross-section) and the aspect ratio of 0.83 ± 0.02 (**Fig. 1d**).

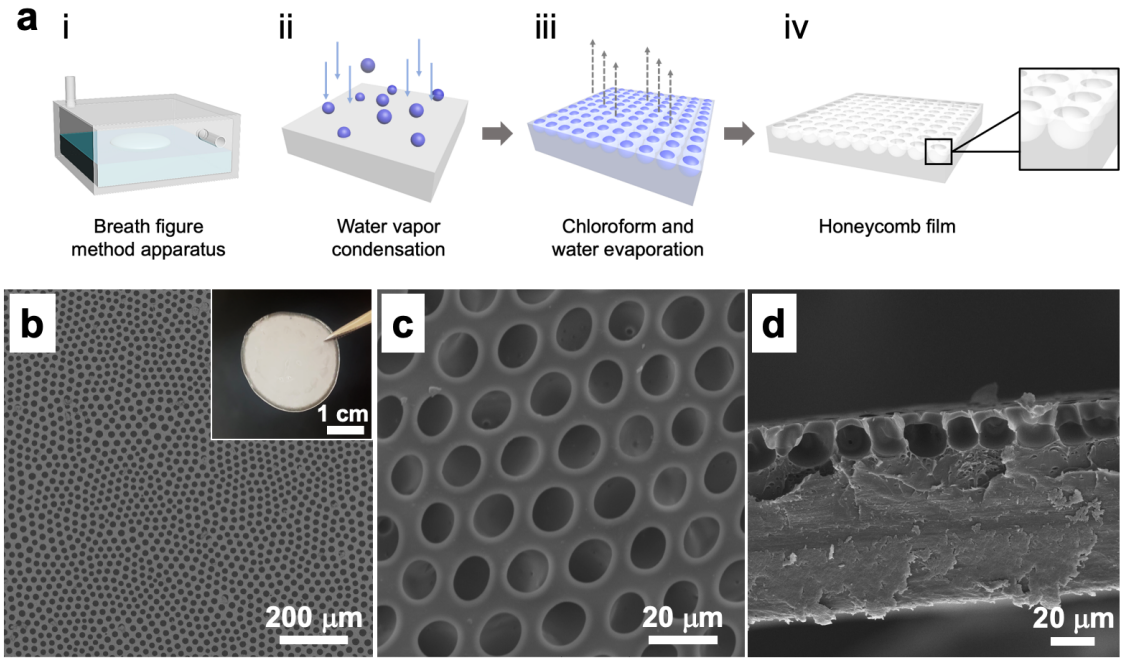

Figure 1. Preparation of honeycomb template. a. schematic of breath figure method: (i) Apparatus of breath figure method: a sealable chamber containing saturated sodium chloride and a platform above the liquid surface; (ii) Water vapor condenses into microdroplets on the polystyrene chloroform solution; (iii) Water droplets self-assemble and sink into the polymer solution, followed by the evaporation of water and chloroform; (iv) Polystyrene honeycomb film with spherical pores. **b,** Scanning Electron Micrograph of polystyrene film surface showing homogeneous circular pores, inset: optical image of

the round polystyrene film exhibiting white color, removed from the glass slide. **c,** A higher magnification view the honeycomb template demonstrating homogeneous pore size. **d,** Cross-sectional SEM images of polystyrene honeycomb films, showing spherical pores of uniform depth.

To fabricate BSA hydrogel films with microbumps, a mixture of 5% BSA solution and 1% glutaraldehyde (GA) was cast on a plasma-treated polystyrene honeycomb film, as illustrated in **Fig. 2a**. The honeycomb film was hydrophobic, as prepared, with a contact angle of 98.4° ±3.2° (**Fig. 2b**). CO_2 plasma is known to place abundant carboxyl groups on the surface of the polystyrene honeycomb film,[23] and so this was used to increase hydrophilicity of the surface and enable the BSA solution to fully occupy the pores. As a result of plasma treatment, the contact angle of water droplets on the polystyrene honeycomb film decreased to 8.2° ± 2.8° (**Fig. 2c**). The BSA and GA mixture was added to the plasma-treated polystyrene honeycomb mold under vacuum, which helped the reaction mixture to better fill in the spherical pores of the honeycomb film. After dissolving the polystyrene template in toluene, a stand-alone BSA hydrogel film with microbumps was achieved. The film exhibited a yellow hue (**Fig. 2d**), typical of BSA crosslinked with GA,[12] with close-packed microbumps (**Fig. 2e**) and an aspect ratio of 0.85 ± 0.09, close to the value obtained for the pores of the honeycomb film. The SEM image of the insert in **Fig. 2f** further confirms the sphericity of the microbumps. Characterization of the storage (G') and loss (G") moduli of the BSA/GA mixture before and after crosslinking confirmed the gelation of BSA (**Supplementary Fig. 1**).

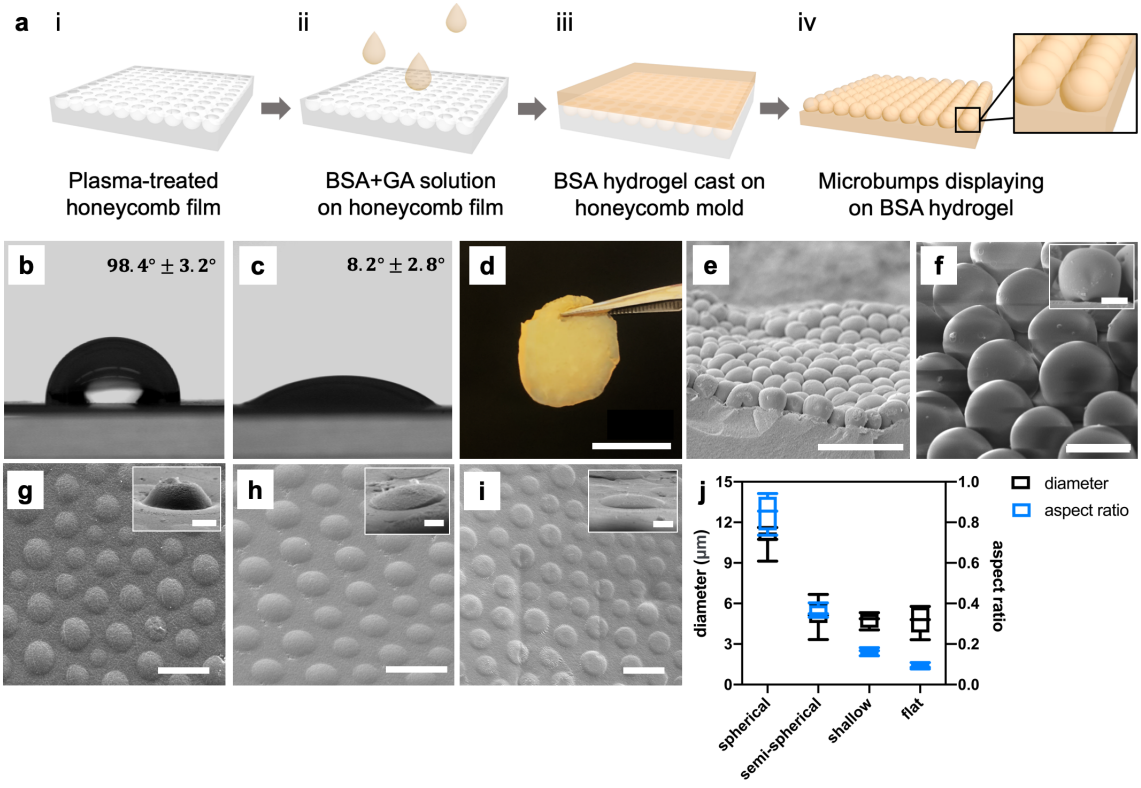

Figure 2. Preparation of hydrogels with arrays of sphericity-controlled microbumps. **a,** Schematic diagram of the process of preparing BSA hydrogel films with microbumps: (i) Honeycomb film is plasma-treated to increase hydrophilicity; (ii) BSA solution, mixed with glutaraldehyde, is added to the polystyrene honeycomb film; (iii) BSA solution gels and form a hydrogel cast on honeycomb mold; (iv) Once BSA is crosslinked into a hydrogel, the polystyrene template is dissolved off to reveal a free standing hydrogel decorated with microbumps. **b,** Water contact angle on untreated polystyrene honeycomb film. **c,** Water contact angle on plasma-coated polystyrene honeycomb film. **d,** Photo of prepared BSA hydrogel using a honeycomb film as template (scale bar 1 cm). **e,** Large-scale cross-sectional SEM image of microbumps prepared using plasma-coated substrate in the presence of vacuum (scale bar 100 μm). SEM image of microbumps (scale bar 10

μm) prepared using: **f,** plasma-coated substrate with vacuum; **g,** plasma-coated substrate with no vacuum; **h,** none plasma-coated substrate in the presence of vacuum; **i,** none plasma-coated substrate with no vacuum. Insert in image **f-i** shows cross-sectional SEM image of the same hydrogel (scale bar 5 μm). **j,** Diameter and aspect ratio of the microbumps with different sphericity.

We further demonstrated that by changing two parameters, namely plasma coating of the template and using vacuum on the template during the crosslinking reaction, we could control the sphericity of microbumps. In the absence of vacuum, the shape of microbumps was a shallow arch, even in the presence of the plasma-coated template, with an aspect ratio of 0.36 ± 0.03 (**Fig. 2g**). When the template was not plasma coated, and hence was hydrophobic, an aspect ratio of 0.17 ± 0.02 was observed when we used vacuum (**Fig. 2h)** and an aspect ratio of 0.09 ± 0.01 (**Fig. 2i**) in the absence of vacuum. These microbumps with different sphericity provide 2-dimensional surface (flat), 2.5-dimensional surface (shallow microbumps), and ultimately 3-dimensional surface (spherical microbumps), providing different substrate candidates for diverse scenarios in cell culture and sensing.

We demonstrated that BSA microbumps can display nanostructure on their surface after embedding BSA nanogels, which are made of the same components (BSA and glutaraldehyde), inside the bumps during the gelation process. This was achieved by filling BSA nanogels (353.7 nm, ζ potential=-33.8 mV, **Supplementary Fig. 2**) into the template pores first, followed by adding BSA and glutaraldehyde mixture to the template (**Fig. 3a**). Interestingly, no obvious hierarchic structure was observed when a plasma-coated template

was used (**Fig. 3b**), which suggests that the BSA solution completely filled the template pores and encapsulated the nanogels. A nano-on-micro hierarchic structure appeared after omitting vacuum during the crosslinking reaction (**Fig. 3c**). The surface roughness of the hydrogel microbumps increased further when a none plasma-treated template (hydrophobic template) was used (**Fig. 3d**), and the highest surface roughness was achieved when both processes were omitted (**Fig. 3e**). It is noteworthy that the microbumps under all these conditions remained spherical, and the shallow microbumps observed in **Fig. 2** were absent. This may be a result of BSA solution filling the gaps between nanogels that had already lined the inside of the micropores as result of capillarity action. **Fig. 3f** shows a cross section of the microbumps in **Fig. 3e** (highest roughness); the BSA nanogels appear integrated with the body of the hydrogel, and not as separate layer around the edges of the microbump, yet the microbump surface is visually rough.

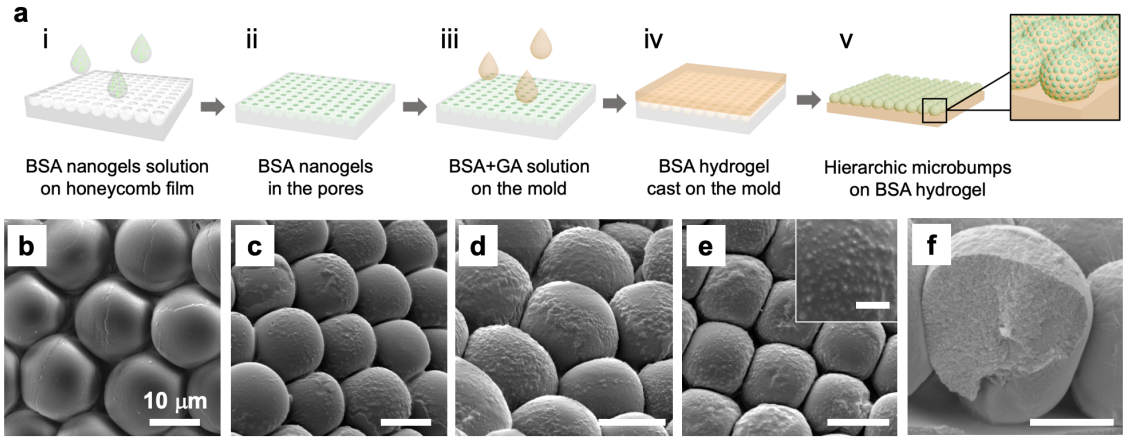

Figure 3. Controlling the surface roughness of BSA hydrogel microbumps. a, Schematic diagram of the process of preparing BSA hydrogel films with hierarchical microbumps; (i) BSA nanogel suspension is first added to the polystyrene honeycomb film; (ii) once the nanogels have settled into the micropores, (iii) BSA solution mixed with

glutaraldehyde is added to the on top. (iv) when the gel has solidified, (v) the polystyrene template is dissolved off. SEM images of microbumps of a 5% BSA hydrogel film containing 100 μL of nanogels achieved using: **b,** plasma-coated substrate in the presence of vacuum; **c,** plasma-coated substrate and no vacuum; **d,** none plasma-coated substrate in the presence of vacuum; **e,** none plasma-coated substrate and no vacuum; **f,** cross-sectional SEM image of microbumps in part **e**. The scale bar for panels **b-f** is 10 μm. The scale bar for Insert in panel **e** is 2 μm.

In addition to microbumps, reverse microstructures (honeycomb micropores) on BSA hydrogel films were prepared using Ecoflex microbumps as a secondary template derived from polystyrene honeycomb films (**Supplementary Fig. 3a**). The honeycomb hydrogels were prepared as an additional control for investigating the bacterial repellency of the hierarchical microbumps by checking for the effect of reverse microstructures. The material for the secondary template is a silicone elastomer, Ecoflex, which shows excellent flexibility and stretchability.[24] As shown in **Supplementary Fig. 3b**, the Ecoflex microbumps are comparable in size to the BSA microbumps, with a size of 27.1 $\pm$ 2.3 μm. The BSA hydrogel film was then made by adding BSA and glutaraldehyde solution on the Ecoflex template and peeling off the film after gelation (**Supplementary Fig. 3c**). The Ecoflex template was plasma-coated in advance and vacuum was used during the crosslinking reaction, which resulted in a hydrogel film with very shallow pores (**Supplementary Fig. 3d**). We believe this to be a result of the gaps between the microbumps being too narrow. As a result, the BSA hydrogel at the bottom of the

microbumps were still trapped in the template during the peeling process. The distance between the microbumps can be changed by stretching the Ecoflex film. We first stretched the Ecoflex template in all 4 directions to 2 times its original length. Afterwards, the casting and separation of BSA hydrogel film are same as using upstretched Ecoflex template (**Supplementary Fig. 3e**). The obtained BSA hydrogel film showed deeper pores with an aspect ratio of 0.57 ± 0.04 (**Supplementary Fig. 3f**). To measure hydrophilicity, we tested the contact angle of water droplets on BSA hydrogel films. The flat BSA hydrogel film had a contact angle of $79.1° \pm 3.2°$ (**Fig. 4a**), while smooth microbumps had a lower contact angle of $58.0° \pm 4.8°$(**Fig. 4b**). The hierarchical nano-on-micro structure provides a significantly stronger wettability with a contact angle of $25.2° \pm 4.4°$(**Fig. 4c**). Therefore, the microbumps resulted in a more hydrophilic hydrogel surface, with the hierarchical nano-on-micro structure resulting in the most hydrophilic BSA hydrogel surface. We hypothesized that the increased hydrophilicity of the hierarchical nano-on-micro structure could lead to the formation of a hydration layer, which in turn can exhibit strong bacterial-repellent ability comparing to flat hydrogel surface. This hypothesis was based on a similar effect observed in surfaces coated with microgels.[25] The nanostructured BSA microbumps are expected to reach an highly hydrated state in an aqueous environment, forming a water barrier and preventing the adhesion of the bacteria. To test this hypothesis and to understand the effect of the designed microstructures on bacterial adhesion onto protein hydrogels, we incubated *S. aureus* MZ100 for 2 days with BSA hydrogel films displaying a flat surface, smooth spherical microbumps, and hierarchical microbumps. The selected *S.*

aureus strain is a multidrug resistant strain and has been reported to be a good biofilm former,[26] which was independently confirmed in our lab.

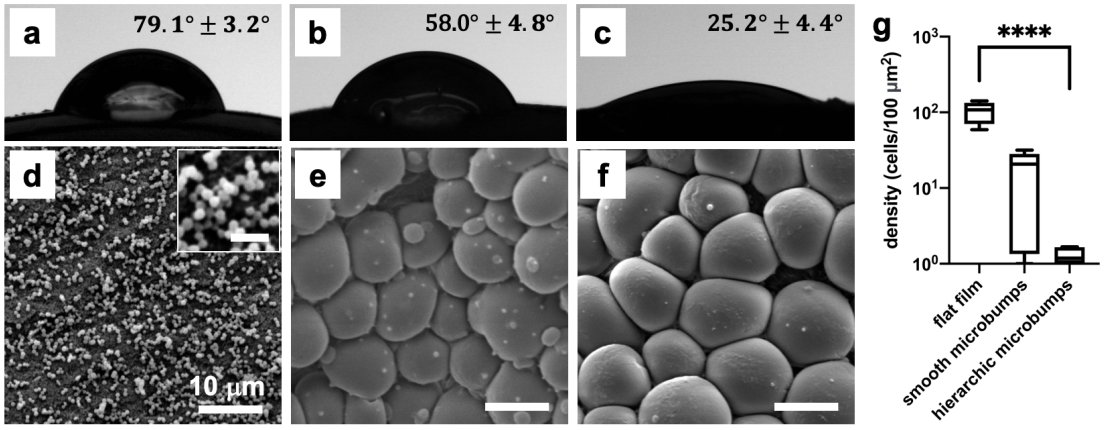

Figure 4. a-c, Wetting behavior of a water droplet on BSA hydrogel films with different surfaces: **a,** flat surface; **b,** smooth microbumps; **c,** nano-on-micro hierarchical bumps. **d-f** SEM images of *S. aureus* on BSA hydrogel films with different surfaces after incubating 2 days: **d,** flat surface; **e,** smooth microbumps; **f,** nano-on-micro hierarchical bumps. **g,** *S. aureus* distribution density on BSA hydrogel films after incubating for 2 days, $p<0.0001$. The scale bar for panels **d-f** is 10 μm. The scale bar for insert in **d** is 5 μm.

As shown in **Fig. 4d**, the entire flat BSA hydrogel was covered with *S. aureus* after 2 days of incubation. On the contrary, the bacterial number was visibly less on the smooth spherical microbumps (**Fig. 4e**). Meanwhile, there were only sporadic occurrences of bacteria adhesion on the hierarchical microbumps (**Fig. 4f**). The bacterial densities on each surface are presented in **Figure 4g**. The distribution density of *S. aureus* decreased from an average of ~100 cells/100 μm^2 for a flat hydrogel surface to ~1 cells/100 μm^2 for hierarchical hydrogel microbumps, indicating that bacterial adhesion decreased by 98.9%.

We also tested the bacterial adhesion on two types of BSA honeycomb films to rule out the effect of surface heterogeneity on bacteria repellency (**Supplementary Fig. 4**). The bacterial density on honeycomb hydrogels is difficult to count because some bacterial cells are sheltered in the pores. However, the bacterial density on the reversed structure is visibly high and on par with flat hydrogel.

3.4 Conclusion

In conclusion, we report the development of hierarchically-structured protein hydrogels that significantly inhibit long term attachment of multidrug resistant Staphylococcus *aureus* up to 100× over a flat hydrogel. Reports on bacteria repellent hydrogels are scarce and the few published are based on microstructured (not hierarchically structured) synthetic polymer hydrogels.[25] Furthermore, none of the previous reports achieved long term repellency and of the magnitude we observed in this work. By developing a method that enables decorating protein hydrogels with nano-on-micro hierarchical structures, we were able to develop a hydrogel that exhibits bacteria repellency surpassing anything reported in the literature, to date. Therefor the major contribution of our work is the development of a method for decorating hydrogels with an ordered array of hierarchical structures that is also compatible with protein hydrogels. Our method can be extended to polymer hydrogel that contain heat-sensitive molecules, such as antibiotics and most drugs that could in principal be loaded in hydrogels for enhanced delivery. The simple method we designed to fabricate uniform hydrogel microstructures, and nano-on-micro structures is much simpler compared to traditional photolithographic or molding methods, which require expensive and complex equipment. This method also allows us to design hydrogel with different

microstructures using the same template. Hydrogels with those microscale patterns, especially with hierarchic structures, provide expanded surface area and hydrophilic surface which are uniquely suited for biosensing as well as antifouling applications.

3.5 Conflicts of interest

The authors declare no conflict of interest.

3.6 References

1. Soleymani, L. *et al.* Hierarchical nanotextured microelectrodes overcome the molecular transport barrier to achieve rapid, direct bacterial detection. *ACS Nano* **5**, 3360–3366 (2011).
2. Wang, F. *et al.* Bioinspired micro/nano fabrication on dental implant-bone interface. *Appl. Surf. Sci.* **265**, 480–488 (2013).
3. Zhao, X. *et al.* Hierarchically engineered membrane surfaces with superior antifouling and self-cleaning properties. *J. Memb. Sci.* **441**, 93–101 (2013).
4. Zhu, Y., Zhang, Q., Shi, X. & Han, D. Hierarchical Hydrogel Composite Interfaces with Robust Mechanical Properties for Biomedical Applications. *Adv. Mater.* **31**, 1–5 (2019).
5. Peivandi, A., Tian, L., Mahabir, R. & Hosseinidoust, Z. Hierarchically Structured, Self-Healing, Fluorescent, Bioactive Hydrogels with Self-Organizing Bundles of Phage Nanofilaments. *Chem. Mater.* **31**, 5442–5449 (2019).
6. Pan, L. *et al.* Hierarchical nanostructured conducting polymer hydrogel with high electrochemical activity. *Proc. Natl. Acad. Sci. U. S. A.* **109**, 9287–9292 (2012).
7. Liu, K. *et al.* Coordination-triggered hierarchical folate/zinc supramolecular hydrogels leading to printable biomaterials. *ACS Appl. Mater. Interfaces* **10**, 4530–4539 (2018).
8. Sagbas, S. & Sahiner, N. Modifiable natural gum based microgel capsules as sustainable drug delivery systems. *Carbohydr. Polym.* **200**, 128–136 (2018).
9. Lv, C. *et al.* Humidity-responsive actuation of programmable hydrogel microstructures based on 3D printing. *Sensors Actuators, B Chem.* **259**, 736–744 (2018).
10. De France, K. J. *et al.* 2.5D Hierarchical Structuring of Nanocomposite Hydrogel Films Containing Cellulose Nanocrystals. *ACS Appl. Mater. Interfaces* **11**, 6325–6335 (2019).
11. Ma, X. *et al.* A Biocompatible and Biodegradable Protein Hydrogel with Green and Red Autofluorescence: Preparation, Characterization and in Vivo Biodegradation Tracking and Modeling. *Sci. Rep.* **6**, 1–12 (2016).
12. Peivandi, A. *et al.* Inducing Microscale Structural Order in Phage Nanofilament Hydrogels with Globular Proteins. *ACS Biomater. Sci. Eng.* In press (2021).
13. Levalley, P. J. *et al.* Fabrication of Functional Biomaterial Microstructures by in

Situ Photopolymerization and Photodegradation. *ACS Biomater. Sci. Eng.* **4**, 3078–3087 (2018).
14. Liu, J., Gao, D., Li, H. F. & Lin, J. M. Controlled photopolymerization of hydrogel microstructures inside microchannels for bioassays. *Lab Chip* **9**, 1301–1305 (2009).
15. Franzesi, G. T., Ni, B., Ling, Y. & Khademhosseini, A. A controlled-release strategy for the generation of cross-linked hydrogel microstructures. *J. Am. Chem. Soc.* **128**, 15064–15065 (2006).
16. Kim, D. N., Lee, W. & Koh, W. G. Micropatterning of proteins on the surface of three-dimensional poly(ethylene glycol) hydrogel microstructures. *Anal. Chim. Acta* **609**, 59–65 (2008).
17. Widawski, G. & Rawiso, M. Self-organized honeycomb morphology of star-polymer polystyrene films. *Nature* **369**, 387–389 (1994).
18. Zhu, C., Tian, L., Liao, J., Zhang, X. & Gu, Z. Fabrication of Bioinspired Hierarchical Functional Structures by Using Honeycomb Films as Templates. *Adv. Funct. Mater.* **28**, 1–8 (2018).
19. Kyoung, J. & Basavaraja, K. C. Preparation and characterization of smart hydrogel nanocomposites sensitive to oxidation – reduction. *Polym. Bull.* **70**, 207–220 (2013).
20. Online, V. A., Jang, J. H., Orba, M., Wang, S. & Huh, D. S. Adsorption–desorption oscillations of nanoparticles on a honeycomb-patterned pH-responsive hydrogel surface in a closed reaction system. *Phys. Chem. Chem. Phys.* **16**, 25296–25305 (2014).
21. Bronze-Uhle, E. S., Costa, B. C., Ximenes, V. F. & Lisboa-Filho, P. N. Synthetic nanoparticles of bovine serum albumin with entrapped salicylic acid. *Nanotechnol. Sci. Appl.* **10**, 11–21 (2017).
22. Caraceni, P., Tufoni, M. & Bonavita, M. E. Clinical use of albumin. *Blood Transfus.* **11**, s18 (2013).
23. Guruvenket, S., Rao, G. M., Komath, M. & Raichur, A. M. Plasma surface modification of polystyrene and polyethylene. *Appl. Surf. Sci.* **236**, 278–284 (2004).
24. Chan, Y. *et al.* Solution-processed wrinkled electrodes enable the development of stretchable electrochemical biosensors. *Analyst* **144**, 172–179 (2019).
25. Keskin, D., Mergel, O., Van Der Mei, H. C., Busscher, H. J. & Van Rijn, P. Inhibiting Bacterial Adhesion by Mechanically Modulated Microgel Coatings. *Biomacromolecules* **20**, 243–253 (2019).
26. Shanks, R. M. Q. *et al.* Genetic evidence for an alternative citrate-dependent biofilm formation pathway in Staphylococcus aureus that is dependent on fibronectin binding proteins and the grars two-component regulatory system. *Infect. Immun.* **76**, 2469–2477 (2008).

Chapter 3 Appendix: Supplementary Information

3.7 Experimental section

3.7.1 Materials

Polystyrene (M_w=650 000), chloroform, ethanol and toluene were purchased from MilliporeSigma. Bovine serum albumin (lyophilized, powder), glutaraldehyde solution (50%) and LB broth were obtained from fisher scientific. Ecoflex was purchased from Sculpture Supply Canada. All chemicals were used as received. *Staphylococcus aureus* MZ100 is generously provided by Dr. Michael Surette, McMaster University.

3.7.2 Preparing polystyrene honeycomb film

A sealed chamber with a removable lid was set up within saturated NaCl solution and a platform above the liquid level to maintain a stable humid environment. 5 wt% of polystyrene (M_w= 650 k) in chloroform was dropped on a glass slide placed on the platform and the chamber lid was sealed thereafter. The polystyrene solution was allowed to evaporate and turn solid for 20 mins before being taken out, peeled off the glass slide, and stored for imaging and use in further experiments.

3.7.3 Preparing BSA hydrogel film with microbumps

A final concentration of 5% BSA and 1% GA solution was added on to the surface of a plasma-treated polystyrene honeycomb film and left incubating for 30 mins at room temperature to solidify and form a gel. The polystyrene honeycomb film was removed from the BSA hydrogel by submerging the sample in a glass vial of toluene for 20 mins in a shaking incubator. This step was repeated 2 more times with new glass vials of toluene. The sample was dried with Kimwipes. The sample was then stored in MilliQ water for

future imaging and experimentation. BSA hydrogel with flat surface was obtained using a flat polystyrene film as the template where the procedure of removing flat polystyrene film was same as removing polystyrene honeycomb films.

3.7.4 Control the sphericity of microbumps on BSA hydrogel film

To achieve varied sphericity of the microbumps, the polystyrene honeycomb films underwent a combination of either plasma treatment with CO_2 for 10 minutes to increase hydrophilicity or no plasma treatment, and the addition of 5% BSA and 1% GA under vacuum conditions or normal atmospheric conditions.

3.7.5 Synthesizing and characterizing BSA nanogels

The preparation of BSA nanogels followed a classic desolvation method, described by Weber et al.[1] Briefly, 150 mg of BSA was dissolved in 2 mL of 10 mM NaCl solution, and then 10 μL of NaOH was added to adjust the pH to 7-9. 8 mL of ethanol was added continuously dropwise using a syringe pump (1 mL/min) while stirring for 500 rpm at room temperature. After all the ethanol is added, 176.25 μL of 8% GA (1.175 μL GA/mg BSA) was added to the solution to induce particle crosslinking. The reaction was performed while stirring at 500 rpm for 24 hrs. Once the crosslinking reaction was completed, the sample was centrifuged at $25{,}000 \times g$ for 10 mins. The supernatant was discarded, and the nanoparticles were dispersed in water for characterization and further experiments. Average particle size was measured using dynamic light scattering (DLS) using a Malvern Zeta Sizer Nano ZSP. Zeta potential of BSA nanogels was measured in 1 mM KCl.

3.7.6 Controlling the roughness of microbumps on BSA hydrogel films

To achieve varied surface roughness of the microbumps, the polystyrene honeycomb films underwent a combination of plasma treatment with CO_2 for 10 mins or no plasma treatment, the addition of the BSA solution in vacuum conditions or normal atmospheric conditions, the addition of BSA nanogels, and the addition of 5% BSA with 1% GA as the chemical crosslinker.

3.7.7 Preparing Ecoflex film with microbumps

To prepare Ecoflex film with microbumps, a polystyrene honeycomb film was firstly placed inside a well of a twelve-well plate. Ecoflex components A and B were mixed together in a 1:1 ratio and dropped on top of the polystyrene honeycomb film. Then the plate was placed in vacuum for 20 mins. After 10 mins, the 12-well plate was taken out. The honeycomb film was pushed to the bottom of the well and left on the bench for 4 hrs to solidify. After solidifying, the Ecoflex film was taken out of the 12-well plate. The polystyrene film was peeled off to obtain an Ecoflex microbump film and stored at room temperature for future imaging and experimentation.

3.7.8 Preparing BSA honeycomb films

A Ecoflex microbump film was either unstretched or stretched using an apparatus containing twine, clamps, and an empty petri dish. BSA solution was placed on the surface of the Ecoflex microbump film and placed in a vacuum desiccator for 20 mins or until there were visually no more air pockets in the solution. GA was added to the BSA solution to a final concentrations of 1% GA and 5% BSA, and the solution was gently mixed. The sample was put under vacuum for another 30 mins and was then taken out and left on the

bench for an additional 1 hr to continue gelation. Once gelled, the BSA hydrogel was peeled and kept in MilliQ water for future imaging and experimentation.

3.7.9 Bacterial adhesion test

Overnight culture of *S. aureus* was diluted 1000× (10 μL of overnight culture in 10 mL of LB media), added to 3 BSA hydrogel films with or without microbumps and incubated at 37 ºC, 180 rpm for 48 hrs. Then the hydrogels were taken out and washed for electron microscopy. 8 images were counted for bacteria quantification.

3.7.10 Hydrogel characterization

The morphologies of the honeycomb films and microstructured hydrogels were coated with a 15 nm layer of gold and imaged by a scanning electron microscopy (TESCAN VP, SEM) under 10 kV. The hydrogels were processed critical-point drying before imaging. The water contact angles of hydrogel surfaces were measured by a contact angle instrument (KRUSS, Drop Shape Analysis System DSA 10) with water droplets (5 μL) dispensed by automated syringe.

3.8 Supplementary figures

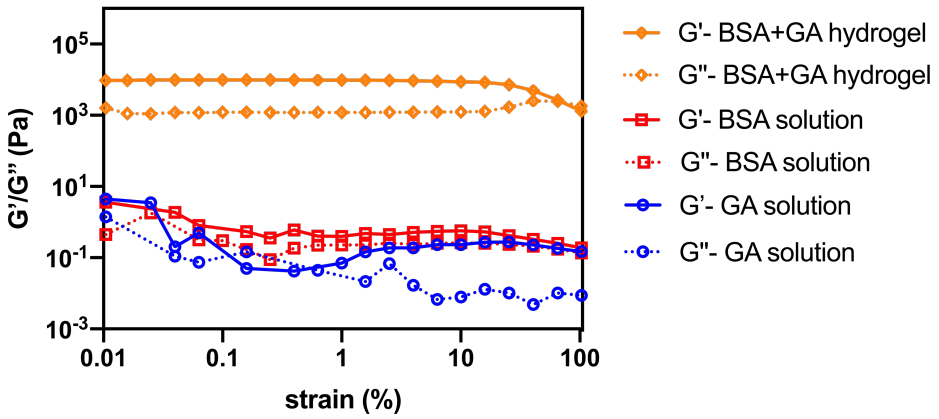

Supplementary Figure 1. Strain sweep test indicating the storage modulus (G', filled) and loss modulus (G", unfilled) for BSA hydrogel and the pre-gelling components (BSA solution and glutaraldehyde solution).

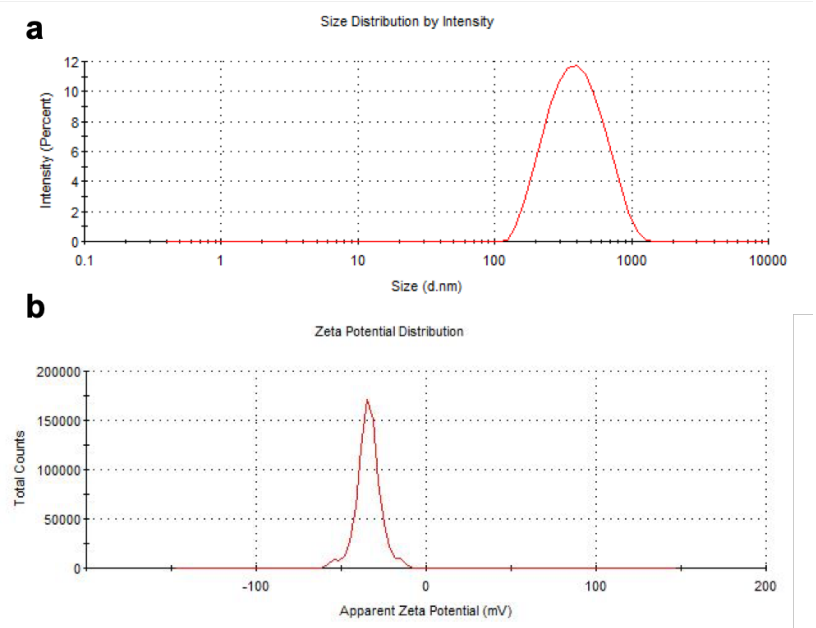

Supplementary Figure 2. a, Size distribution and **b,** zeta potential distribution of BSA nanogels in 1 mM KCl solution.

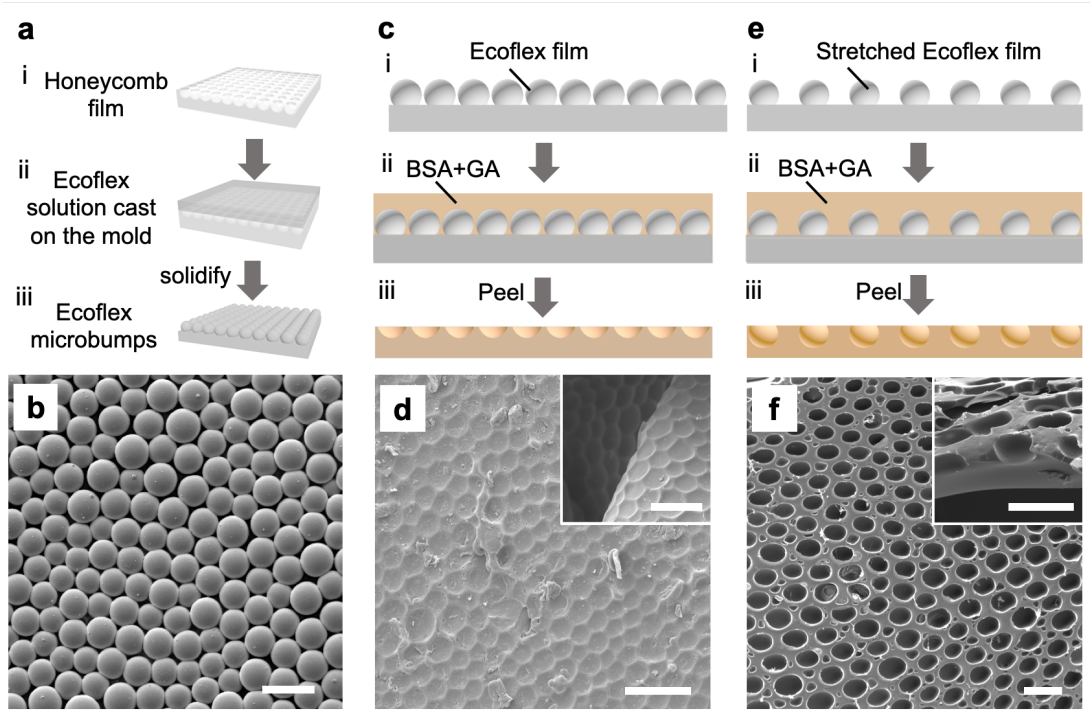

Supplementary Figure 3. The preparation of BSA honeycomb hydrogel films: **a,** Schematic diagram of the process of casting Ecoflex secondary template with microbumps; (i) a polystyrene honeycomb film is prepared; (ii) Ecoflex solution is cast on polystyrene honeycomb film under vacuum; (iii) After Ecoflex solution turns solid, the Ecoflex film can be peeled off from the template. Then the Ecoflex film with microbumps can be peeled from the honeycomb film. **b,** SEM image of Ecoflex film with microbumps (scale bar 50 μm). **c,** Schematic diagram of the process of preparing BSA honeycomb film with shallow pores; (i, ii) BSA solution mixed with glutaraldehyde is added to the top of Ecoflex microbumps, (iii) and the Ecoflex template is subsequently peeled off. **d,** SEM image of BSA honeycomb film with shallow pores (scale bar 20 μm). **e,** Schematic diagram of the process of preparing BSA honeycomb film with deep pores; (i) the Ecoflex template is first stretched to 1.5 times its original length and then (ii) BSA solution mixed with

glutaraldehyde is added on top. (iii) Independent BSA film is obtained by simply peeling off from the template. **f,** SEM image of BSA honeycomb film with deep pores (scale bar 20 μm). Insert in D and F show cross-sectional SEM image of the same hydrogel (scale bar 50 μm).

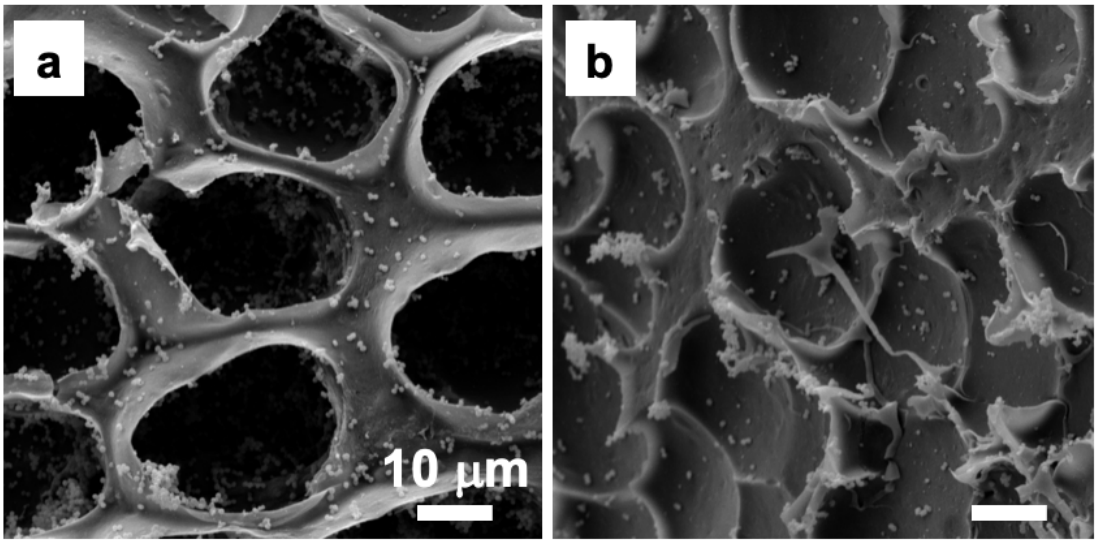

Supplementary Figure 4. SEM images of BSA honeycomb hydrogel films with different microstructural surface incubated with *Staph. aureus* for 2 days in LB media: **a.** deep pores; **b,** shallow pores.

3.9 References

1. Weber, C., Coester, C., Kreuter, J. & Langer, K. Desolvation process and surface characterisation of protein nanoparticles. *Int. J. Pharm.* **194**, 91–102 (2000).

Chapter 4: Self-Assembling Nanofibrous Viral Microgels as Sprayable Antimicrobials Targeting Multidrug- Resistant Bacteria

In this chapter, we report the first viral-exclusive microparticle. Herein, bacteriophages serve not only as strong natural antimicrobial agents, but also as self-replicated, consistent nanoparticles to construct hierarchical biomaterials. Based on the experience of utilizing honeycomb templates in the previous chapter, we further adapt the molding method and produce bioactive phage beads. It demonstrates the importance of microscale phage materials and encourages us to construct diverse microstructured phage particles which will be illustrated in the next chapter.

In this chapter, experiments were performed by Lei Tian and two undergraduate researchers, Leon He and Kyle Jackson. All data was analyzed by Lei Tian. The chapter was drafted by Lei Tian and subsequently edited by Dr. Zeinab Hosseinidoust and Dr. Tohid Didar. This chapter and the supporting information were submitted to *Nature Communications*.

Self-Assembling Nanofibrous Viral Microgels as Sprayable Antimicrobials Targeting Multidrug-Resistant Bacteria

Lei Tian, Leon He, Kyle Jackson, Ahmed Saif, Shadman Khan, Zeqi Wan, Tohid Didar, Zeinab Hosseinidoust

Nature Communications, **2022**, *under minor revision*, NCOMMS-22-00018A-Z.

4.1 Abstract

Bacteriophages, or bacterial viruses, are naturally antimicrobial proteinous nanoparticles. We packed *half a million* self-organized phages, as the sole structural component, to construct soft microparticles, thus creating a virus-exclusive microgel platform that preserved and amplified the natural antimicrobial activity of their nano building blocks. We further developed a high-throughput template method to manufacture superintegrated, single-layered, pure and hybrid phage microgel arrays (at a density of 35,000 microgels/cm^2, equivalent to 13-billion phages per unit area) as antimicrobial patches, which can be optionally detached to independent microgels offering applications as high-load delivery vehicles for sprayable phage antimicrobials. The crosslinked phages in each phage-exclusive microgel self-organized to exhibit a highly-aligned nanofibrous texture and emit tunable fluorescence that can expand potential applications beyond biocontrol to theranostics and biosensing. Sprays of hybrid microgels loaded with potent virulent phage effectively reduced heavy loads of multidrug resistant *Escherichia coli* O157:H7 on food products, leading to up to 6 logs reduction in 9 hours and rendering food contaminant free.

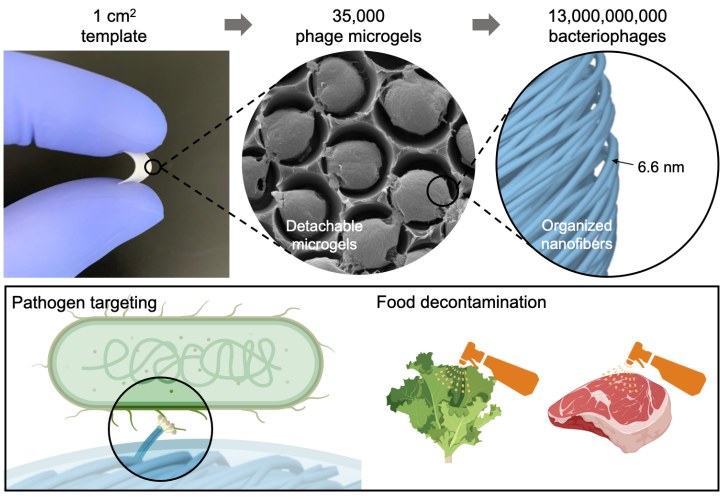

Graphic abstract. Every square centimeter of the template produces over 35,000 separable phage microgels, constituting a 13 billion phage community. This high density of phages self-assemble in a highly aligned manner in the microgels and still retain bioactivity. The microgel suspension can be sprayed on food to prevent contamination from drug-resistant bacteria.

4.2 Introduction

Bacteriophages, also known as phages, are natural bacterial predators and their job in nature is to keep bacterial populations in check.[1,2] Phages infect bacteria in a highly targeted manner - some are able to identify and kill a single strain of bacteria in a heterogeneous population. It follows that when used for biocontrol in environments with a pre-existing commensal bacterial populations, such as certain food products or applications in agriculture, farming or human therapeutic use, phages are less likely to disturb the delicate balance of such communities while still being able to eliminate harmful bacteria.[3] Foodborne diseases result in hundreds of thousands of deaths each year, almost a third of whom are young children.[4] Phage products have been approved by the US Food and Drug Administration for control of dangerous bacterial contaminants such as *Escherichia coli*, *Salmonella*, or *Listeria* in food products.[5,6] The use of phage for food safety has the distinct advantage that, unlike most antimicrobials, it will not impact the taste, texture, and nutritional quality of the food, and can thus be safely applied to decontaminate food products from farm to market to consumer plates.[7,8] However, widespread use is still limited. This is at least partly due to challenges in delivery and stability, which in turn limit the efficacy of the phage products.[9]

Nature makes phages in a variety of shapes and sizes.[10] Phages are, in essence, proteinous nanoparticles that encase a genome, enabling the propagation of wild-type or genetically modified virions into a suspension of identical and monodisperse nanoparticles.[11] In addition, the phage surface chemistry can be customized with atomic precision via genetic engineering or chemical conjugation, making phage virions a powerful building block for multifunctional antimicrobial material.[12–14]

We have previously reported a simple chemistry that was effective at crosslinking filamentous phage, yielding bulk soft material displaying the basic properties of a hydrogel.[15–17] Herein, we reinvented phage gels by developing a high throughput manufacturing method that not only enabled generation of microgels made up entirely of viral nanoparticles, but also preserved the bioactivity of the phage building blocks in the process. Compared to polymeric microgels such as poly(N-isopropylacrylamide)[18] and poly(ethylene glycol),[19] phage microgels remain unexplored, partly because of challenges in manufacturing such microgels. Common microgel preparation methods such as microfluidics[20] or emulsion method[21] are not suitable for microgels encapsulated with or made from heat/solvent sensitive chemicals or biomolecules (such as proteins and viruses) that must retain their bioactivity through the preparation process.

Microgels offer major distinct advantages over bulk material. Namely, they have larger surface areas and thus more contact points for phage with contaminating bacteria as well as enhanced flow properties in suspensions, allowing for delivery via spray or injection, all of which make them a more versatile option for biocontrol in environmental, food, and medical applications.[22–24] Packing phages into soft, hydrated material further has the

advantage of preservation against desiccation and harsh environments.[25,26] The hydrated structure of microgels offers the advantage of preserving desiccation-sensitive biomolecules.

We report a biomolecule-friendly, high-throughput method to synthesize detachable phage microgel arrays, where a microporous mold, made through the breath figure method, was used without the need for large equipment or complex infrastructure. Two crosslinkers each effectively assisted the gelation and nanoscale alignment of phages nanofilaments, with different crosslinking reactions leading to vastly different fluorescence profiles, expanding potential application scenarios beyond food safety. The phage nanofilaments in these virus-exclusive microparticles self-assembled into an orderly, highly aligned nanofibrous structure that served as a high-load delivery vehicle for strong virulent *E. coli* phages and proved highly effective for controlling multidrug resistant *E. coli* O157:H7 in food products.

4.3 Results and discussion

4.3.1 Generation of bacteriophage microgels

The gelation of phage aqueous suspension is based on the crosslinking reaction between M13 filamentous phage and a small molecule chemical crosslinker. The crosslinker, glutaraldehyde (GA), can react with multiple functional groups on the phage coat protein, notably amino groups on the lysine residues.[15] As shown in **Fig. 1a**, reaction 1, a GA molecule reacts with 2 amino groups on two phage capsids and forms Schiff bases connecting these two phages. It is worth mentioning that GA in aqueous solution is not limited to regular monomeric formation. For example, cyclic hemiacetal and cyclic

hemiacetal oligomer are common forms of GA which can react with amine as well and form ether groups (**Supplementary Fig. 1)**. All these possible reactions proceed simultaneously leading to a crosslinked network of phage nanofilaments. The formation of these side products, in addition to the well-documented self-polymerization of GA and the strong autofluorescence of the final gel,[15] make GA a non-ideal choice for certain applications. Therefore, we explored a second small molecule crosslinker 1-Ethyl-3-(3-dimethylaminopropyl) carbodiimide (EDC), which proved capable of crosslinking phage through a different crosslinking mechanism. An EDC molecule first reacts with a carboxyl group on the phage coat protein and forms an amine-reactive intermediate that quickly reacts with an amine group on another phage coat protein to form an amide bond between two phages (**Fig. 1a**, reaction 2).[27,28] It is noteworthy that EDC molecule was not incorporated into the final crosslinked product. Instead, EDC took oxygen atoms from carboxyl groups on phages and formed water-soluble isourea by-product which can be easily washed out. This intermediate role of EDC is the fundament of fabricating phage-exclusive microgels. This mechanism was found to be effective at controlling the optical properties of the microgels, as will be discussed in **Fig. 3**, which potentially brings different applications to phage microgels.

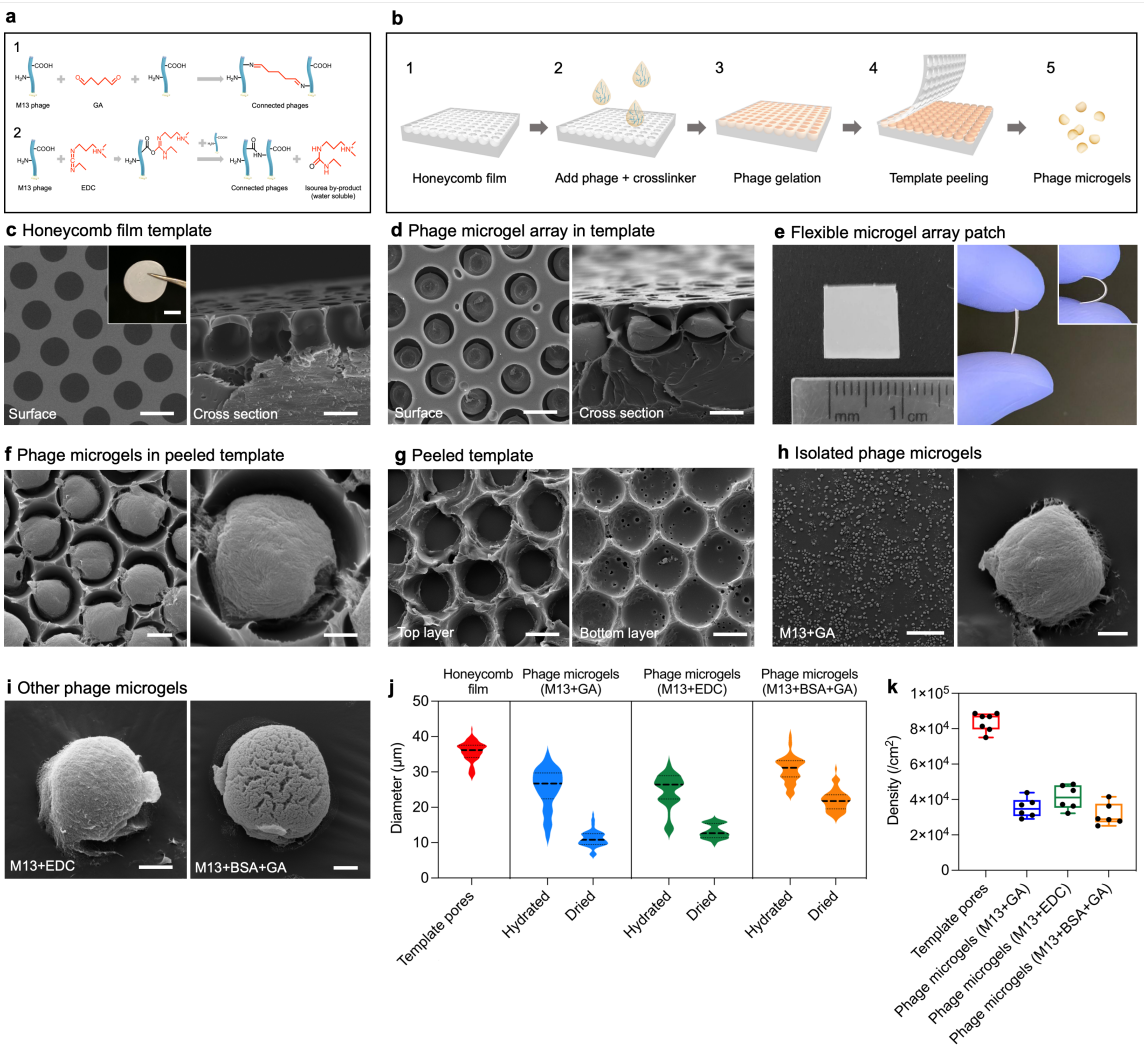

Figure 1. Preparation of bacteriophage microgels using honeycomb film as template: **a**, Crosslinking reactions of M13 bacteriophages with 1. GA and 2. EDC. **b**, Schematic image of preparing phage microgels: 1. Honeycomb film is plasma-coated to turn hydrophilic; 2. Phage and crosslinker mixture solution is cast on the film and placed in the vacuum for 10 mins; 3. The film is placed in a humid environment in 4 °C for 2 days; 4. The top layer of the film is peeled off using adhesive tape; 5. The phage microgels are isolated after removing the film; **c**, Surface and cross-section image of the polystyrene

honeycomb film surface (scale bar 20 μm). Insert: photo of the round polystyrene honeycomb film (scale bar 1 cm). **d**, Surface and cross-section SEM images of M13 crosslinked by GA inside the pores of honeycomb film (scale bar 20 μm). **e**, A flexible honeycomb film containing phage microgel array. Left: photo of an independent composite film tailored into a 1 cm^2 square. Right: photo of the film easily bent by hand. **f**, SEM images of phage microgel array left on a peeled honeycomb film (left, scale bar 10 μm) and zoom-in SEM image of a single phage microgel in this array (right, scale bar 5 μm). **g**, SEM image of the permeable pore network on adhesive tape after peeling (left) and the honeycomb film after peeling and sonication (right). Scale bar 20 μm. **h**, SEM images of the isolated phage microgels (left, scale bar 500 μm) and a single phage microgel made with M13 phages and GA (right, scale bar 5 μm). **i**, SEM images of a phage microgel made with M13 crosslinked with EDC (left) and GA+BSA (right). Scale bar 10 μm. **j**, Size distribution of the template pores and the phage microgels prepared with GA, EDC and BSA at hydrated and dried status. **k**, Pore density of the template and the produced microgel count from every square centimeter of the template.

A single M13 phage exhibits abundant amine and carboxyl groups (5,400 and 10,800, respectively) on its protein coat,[29] providing rich reaction sites for crosslinking reactions. The crosslinked phage virions form a network, resulting in the gelation of the phage aqueous suspension. We observed that M13 and EDC mixture needs less than 12 hrs to gel completely while same concentration of GA takes about 24 hrs to gel.

It is noteworthy that heat and organic solvents are commonly involved during microparticle preparation or isolation,[23,30] which have irreversible detriments for biomaterials. Therefore, manufacturing viral microgels without losing bioactivity would have been exceptionally challenging without developing a suitable microgel manufacturing method. Herein, we proposed a biomaterial-friendly approach for the parathion of pure and hybrid phage microgel. The phage microgels were gelled in and isolated from a polystyrene honeycomb film containing uniform open-ended spherical micropores throughout the film surface, as illustrated in **Fig. 1b**. This is an easy-approachable method to fabricate the large-scale microporous template. The honeycomb films here were prepared via a well-established approach known as the breath figure method.[31,32] A polystyrene chloroform solution (5 wt%, M_w=650,000) was placed on a glass slide inside a stable humid environment (relative humidity≈55%). The evaporation of chloroform created a significantly lower temperature on the solution surface, leading to the condensation of water vapor into microdroplets. The water microdroplets self-assembled and sank into the polymer solution, which was solidified into a white polystyrene honeycomb film and subsequently peeled off from the glass slide. The size of the template can be changed by applying different volumes of polystyrene solution to the glass slide. In the current experiments, 600 μL of polystyrene solution can generate a honeycomb film with a diameter of 2.5 cm. The micropores were uniformly rounded and the cross-sectional Scanning Electron Microscope (SEM) image in **Fig. 1c** indicates that the inner pores exhibited open-ended spherical shape. The inner diameter of the template pores were 35.73±2.86 μm, as measured by electron micrographs.

To fabricate phage microgels, a mixture of M13 suspension and crosslinker (GA/EDC) was cast on a plasma-treated polystyrene honeycomb film (**Fig. 1b**, step 1-2). The film was placed under moderate vacuum for 5 mins to help phage solution fill inside the micropores, followed by removing the redundant phage solution on the template surface by a glass slide. Afterwards, the film was transferred into a sealed humid container at 4 °C for 1 day for gelation (**Fig. 1b**, step 3). As shown in **Fig. 1d**, the original phage suspension inside the pores successfully turned into an ordered array of solid phage microgels. The honeycomb template is a thin round polystyrene film, which means the composite film loading the phage microgel array is flexible. **Fig. 1e** shows a composite film (phage microgels inside the template film) tailored into a 1 cm^2 square and it can easily bend. These properties make the film an excellent patch integrating phage microgels for further antimicrobial and biosensing studies.

Moreover, the microgel array inside the template is detachable. A piece of adhesive tape was used to stick on the composite honeycomb film surface and then peel off the top half of the pores (**Fig. 1b**, step 4**; Supplementary Fig. 2a**). Consequently, the top half of the pores was attached on the tape and the microgels inside the film were exposed on the bottom film layer without damage (**Fig. 1f**). The film was then immersed in 1 mL of sterile water and sonicated for 10 mins to isolate phage microgels out of the template. **Fig. 1g** shows the permeable polystyrene pore network on the tape and the shallow pore structure left on the honeycomb film after peeling and sonication. The microgels were detached successfully and transferred to water phase. **Supplementary Fig. 2b** reveals the edge of the pealing area where the top left of the image is the peeled area of the honeycomb film

showing shallow pores and the bottom right area is the unpeeled deep pores. The peeling procedure effectively separated the honeycomb film (**Supplementary Fig. 2c-d**). Phage microgels were suspended in Millipore water. **Fig. 1h-i** shows the isolated phage aerogel microbeads which are the M13+GA/EDC microgels after critical point drying, proving the microgel array inside the template are detachable. In addition to pure phage microgels, we also added bovine serum albumin (BSA) to M13+GA solution to demonstrate application of the developed method to fabricate hybrid phage microgels, which can further expand the functionality. BSA efficiently provided abundant amino groups and carboxyl groups to consume excessive crosslinker molecules and preserve the bioactivity of M13 phages, which will be illustrated in **Supplementary Fig. 7**. In addition, gelation reaction is accelerated from over 12 hrs to about 30 mins. Although template methods have been used for making microparticles in the past,[32] we essentially reinvented the manufacturing method to enable production of microscale colloidal soft matter, namely phage microgels, in the form of a peelable patch or a suspension. This method is high-throughput, heat-free and solvent-free, which makes it especially advantageous to keep biomolecules active. The size and shape of the microparticles is determined to the template pore shape and size. Fortunately, there are already abundant studies extending the breath figure method to fabricate honeycomb films containing ordered pores at different sizes and shapes.[33–35]

4.3.2 Size distribution, porosity and preparation efficiency of phage microgels

Fig. 1j presents the size distribution of the template pores and phage microgels. The M13 phage microgels crosslinked by GA and EDC separately show a similar size distribution, which is smaller than the template pores (25.34 ± 5.72 μm and 24.39 ± 4.92 μm respectively).

It is noteworthy that the size range of the microgels has a broader distribution compared to the template pores. This might be caused by shrinkage during gelation and possible breakage in the isolation process. Based on the phage concentration used (5×10^{13} PFU/mL) and the average microgel size, we can estimate that each phage microgel is composed of over 7×10^{5} M13 phages. The average size of phage microgels containing BSA is larger (30.77 ± 3.83 μm) and the size range is narrower. The addition of BSA likely makes the microgels denser so the shrinkage and damage during the whole process is lower, which is reflected in the average size and size distribution.

The porosity of these phage microbeads was evaluated by measuring the size change between hydrated and air-dried microbeads. The GA and EDC microgels decreased in diameter to 11.13 ± 2.32 μm and 13.16 ± 1.986 μm, showing 91.5% and 84.3% volume reduction, respectively. The high-volume reduction of phage microgels suggests high porosity. The microgels with added BSA had significantly less shrinkage, maintaining an average size of 21.97 ± 3.04 μm (63.60% volume size reduction), indicating denser, less porous microgels.

The preparation efficiency of the phage microgels was investigated by calculating the microgel count obtained from every square centimeter of the template (details in **Supplementary Note 1, Supplementary Fig. 3**). The honeycomb film template contained 83862 ± 5241 micropores/cm^2. The usage of GA crosslinker produced 35295 ± 5490 phage microgels/cm^2 while EDC crosslinker produced 41226 ± 6878 microgels/cm^2 (**Fig. 1k**). The addition of BSA produced similar results (31431 ± 6185 micropores/cm^2). The number of microgels produced from the template is lower than the template pore density (42.1%,

49.2% and 37.5%). This could be a result of partial filling of phage suspension into the pores or the loss during isolation process. In summary, based on this preparation method, we can obtain over 3.5×10^4 phage microgels from every square centimeter of our template. Each microgel contains more than 3.8×10^5 phage particles, constituting a phage community of 10^{10} in total.

4.3.3 Highly aligned nanofibrous texture of phage microgels

As shown in **Fig. 2a**, M13 phages are high aspect ratio nanofilaments (length = 880 nm, width = 6.6 nm) with a relatively large tip, where five copies of the bacterium-binding protein (g3p) protrude from one end. The size of the small molecule crosslinker GA (M_w=100.11 g/mol) and EDC (M_w=191.70 g/mol) is negligible in comparison. We hypothesized that the phage microgels have nanofibrous texture which are crosslinked filamentous phages, as shown in the schematic image in **Fig. 2b**.

To investigate the nanostructure of phage microgels, the obtained microgels were dehydrated through critical point drying to avoid disrupting the nanostructure and then characterized using a Field Emission SEM. The M13 aerogel microparticles crosslinked by GA showed a sophisticated thread pattern (**Fig. 2c**, image 1). At higher magnification, we observed nanofibers aligning at a single orientation overall where these nanofibers (width between 7 nm and 20 nm) fit the width of a single M13 phage (**Fig. 2c**, image 2-4). The uneven width of fibers could likely be a result of the inevitable 3-nm Pt coating for SEM or the occasional lateral binding of multiple phages. The M13 aerogel microparticles crosslinked by EDC showed a similar ordered nanostructure (**Fig. 2d**). The bright dots in these images are the g3p bacterium-binding sites; these are large protruding proteins that

stand out in electron micrographs. In summary, FE-SEM imaging showed densely packed, self-assembled nanofilaments that formed highly-ordered nanofibrous network during the gelation process.

It is noteworthy that the phage alignment in the hybrid phage-protein (M13+BSA) microgels crosslinked by GA was distinct. The phage nanofilaments in the hybrid microgels were partially embedded in BSA with no particular order (**Fig. 2e**). Adding BSA to the microgel system accelerated the gelation process from 12 hrs to 30 mins, leaving insufficient time for phages to self-assemble. The g3p proteins are still exposed on the microgel surface, providing bacterium-binding sites. Moreover, we investigated pure BSA protein microgels crosslinked by GA to compare the nanostructure with that of phage microgels and confirm that the observed order in the M13 microgels was caused by the M13 nanofilaments and not by the crosslinker or the dehydration procedures. The BSA microgels were processed by same preparation and dehydration procedures and showed no sign fibrous nanostructures. The SEM images of these microgels (**Supplementary Fig. 4**) shows irregularly rough surface, unlike the nanofibrous texture of the phage microgels. In conclusion, the pure phage microgels exhibit a homogenous nanofibrous texture along the same orientation, which is direct evidence that the microgels are composed by phages solely crosslinked by small molecules.

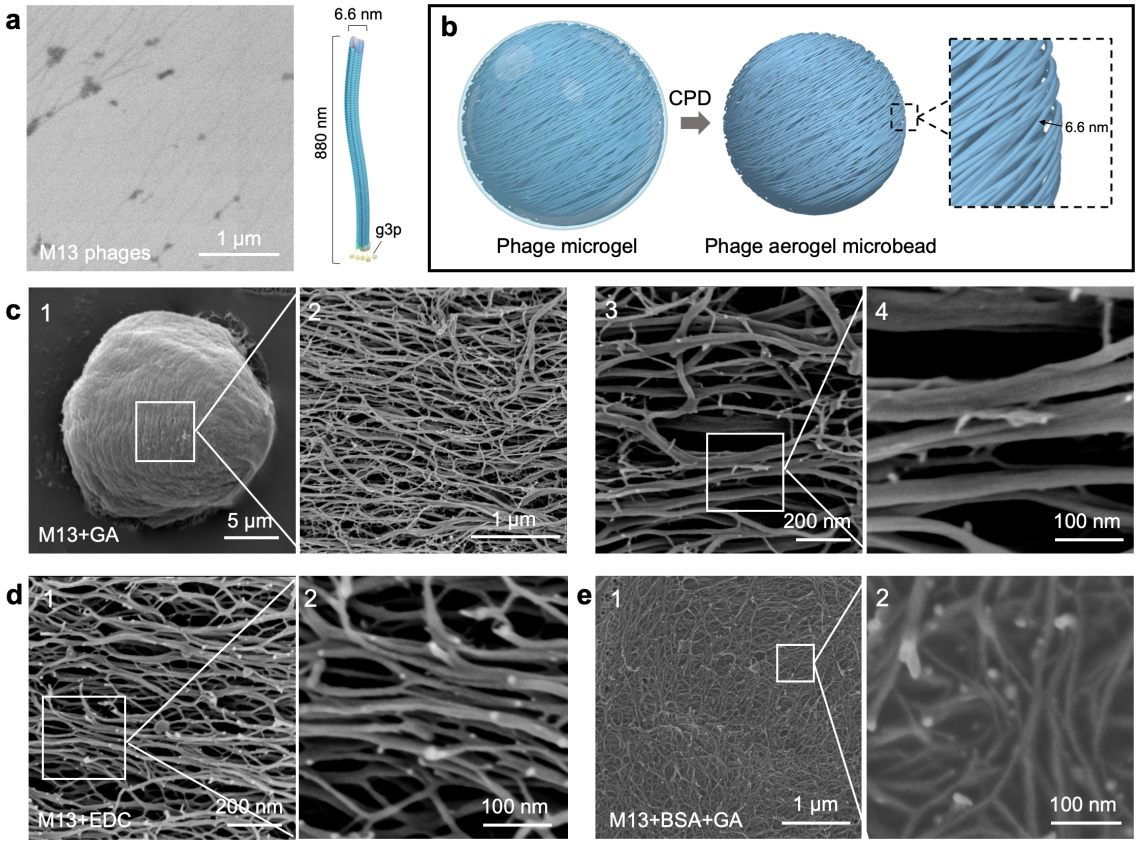

Figure 2. Aligned nanofibrous texture of phage microgels. a, Left: SEM image of non-crosslinked M13 phage nanofibers. Right: Schematic image of a filamentous M13 phage showing high aspect ratio. **b,** Schematic image of a hydrated phage microgel composed of crosslinked filamentous M13 phages turning into a phage aerogel microbead by critical point drying, showing a nanofibrous texture. **c,** SEM images of a M13 phage microgel crosslinked by GA and the highly-aligned nanofibrous texture on the microgel surface. **d,** SEM images of the orderly-aligned nanofibrous texture on a M13 phage microgel crosslinked by EDC; **e,** SEM images of the nanofibrous texture on a M13+BSA microgel crosslinked by GA.

4.3.4 Autofluorescence of phage microgels can be tuned by using different crosslinkers

As shown in **Fig. 3a**, the phage microgels made with GA showed significant autofluorescence in four channels. This phenomenon is associated with electronic transitions such as the $n-\pi^*$ transitions of C=N in the Schiff's base generated from crosslinking reactions.[15,36] This autofluorescence potentiates non-destructive imaging capability of the microgels. However, fluorescence of phage microgels can be troublesome in some application scenarios, for example certain biosensing applications that rely on fluorescence to detect the target analytes. For this reason, we explored microgels of phage crosslinked with an alternative small molecule crosslinker, namely EDC, that do not exhibit autofluorescence (**Fig. 3b**). The amide bonds formed between M13 phage and EDC cause a much weaker fluorescent signal, thus expanding the range of applications for the microgels. In the green and orange channels, the fluorescence of M13+GA and M13+BSA+GA microgels was 294.7% and 320.9% higher than M13+EDC microgels. The largest difference appeared in the red channel where GA-crosslinking microgels had fluorescent signal but the fluorescence of EDC-crosslinking microgels was not observed. Both GA- and EDC-crosslinking phage microgels showed low-fluorescence in the blue channel, and the strongest fluorescence was observed in the orange channel (94.7% and 82.5% higher than their second strongest channel, green).

For scenarios where a strong fluorescence signal is anticipated to be advantageous, we can add BSA to M13+GA microgels to participate the gelation to enhance the fluorescent signal (**Fig. 3c**). The quantified fluorescent intensity of those microgels is illustrated in **Fig. 3d**. The addition of BSA followed the same trend at different channels as pure phage microgels,

and enhanced the fluorescent intensity compared to the GA microgels (23.5% higher at green channel and 26.1% higher at orange channel). Fourier transform infrared (FTIR) spectra further confirmed the functional groups on different phage microgels (**Fig. 3e**). The spectra of M13+GA, M13+EDC and M13+BSA+GA microgels are very similar because of the abundant functional groups on the proteinous capsid of phages. All three spectra showed typical peaks at 1660, 1530 and 1230 cm^{-1}, representative for the amide I, II and III bonds on protein capsids. The three unique peaks showing in GA-crosslinking microgels rather than EDC-crosslinking microgels are at around 3050, 2950 and 1450 cm^{-1} corresponding to sp^2 C-H stretch, aldehyde C-H stretch and imine (C = N) bonds respectively.

In addition, we monitored the gelation procedure using fluorescence microscopy to confirm that the fluorescence signal is the result of gelation, not inherited from the phage building blocks, templates or crosslinkers. During the gelation process, a distinct change in fluorescence was observed using microscopy with four different optical filter sets. As shown in **Fig. 3f-h**, 5×10^{13} PFU/mL of M13 phage suspension with 0.1 M of either crosslinker inside the honeycomb film showed no fluorescence. After the gelation of phage with GA was complete (with or without the addition of BSA), the composite films emitted obvious fluorescent signal at green, orange and red channels. The signal in blue channel was very weak. This change is also observed in the composite film with EDC where its fluorescence signal at these four channels is significantly lower (**Fig. 3i-k)**. This observation confirms that the crosslinking reactions are the sole reason for

autofluorescence and suggests that using different crosslinkers can aid in fine-tuning the fluorescence signal to match the requirements of different application scenarios.

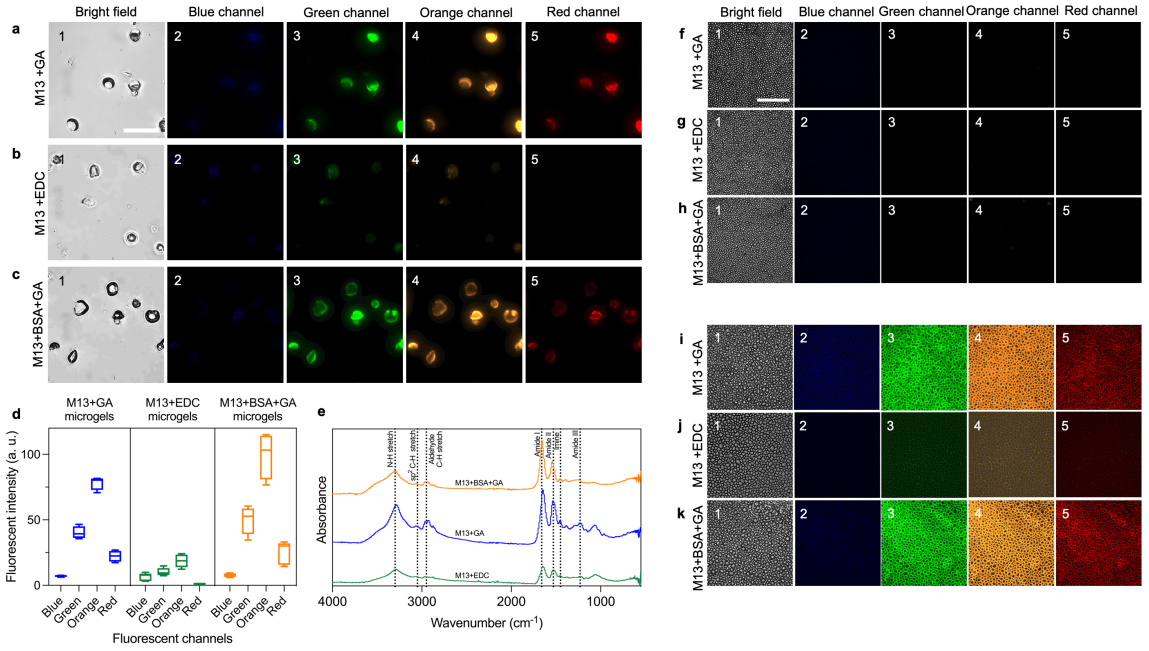

Figure 3. Fluorescence profile of M13 phage microgels and fluorescence profile of the template before and after the microgel formation. a-c, Fluorescent images of three types of phage microgels made of 5×10^{13} PFU/mL of M13 phage with **a,** 0.1 M GA, **b,** 0.1 M EDC, and **c,** 2% BSA + 0.1 M GA. Scale bar: 100 μm. **d,** Quantified fluorescent intensity of 3 types phage microgels under four different channels. **e,** FTIR spectra of phage microgels. **f-h,** fluorescent images of honeycomb template filled with the mixture solution corresponding to **a-c**. Scale bar: 500 μm. **i-k,** fluorescent images of corresponding honeycomb films after the gelation of phage solution inside. Scale bar: 500 μm. Different fluorescent channels are: 1, bright field; 2, film excited at 340 nm and imaged using a λ = 435 nm optical filter (blue channel); 3, film excited at 465 nm and imaged using a λ = 515 nm optical filter (green channel); 4, film excited at 528 nm and imaged using a λ = 590 nm

optical filter (orange channel) and 5, film excited at 625 nm and imaged using a $\lambda = 670$ nm optical filter (red channel).

4.3.5 Targeted antimicrobial functions of phage microgel patches and sprays

We hypothesized that the phage microgels inherited the antimicrobial activity of their phage building blocks and are able to specifically target host bacteria. To investigate the antimicrobial performance of pure and potentially hybrid phage microgels, we used M13 along with two virulent *E. coli* phages, namely T7 and HER262 which have strong and specific killing action but different geometric shapes and mechanisms of infection (details in **Fig. 4a**, **Supplementary Note 2**, **Supplementary Fig. 5a**). Further, we demonstrated that the hydrated environment in microgels can protect desiccation-sensitive phages. As shown in **Supplementary Fig. 5b**, the titers of phages M13, HER262 and T7 all decreased about 4 logs after drying for 1 hr at room temperature and rehydrating.

We demonstrated antimicrobial activity of phage microgels in three biocontrol scenarios: undetached microgel array in the template as an antimicrobial patch, microgel sprayer (**Supplementary Fig. 6a**), and adding microgels directly to a bacterial-contaminated liquid. The microgel spray directly used our microgels suspension, containing over 3×10^4 microgels/mL and all microgels were washed twice. Free phage was not detectable in the eluent after this point. Initially, we evaluated the infectivity of pure M13 phage microgels. It was found out that these two types of microgels did not show obvious infectivity to *E. coli* ER2738 (M13 phage's natural host), neither as a patch or spray (**Supplementary Fig. 6b,** 1-4). The lack of obvious bioactivity stems mainly from the fact that M13 has a low

bactericidal activity even in free suspension form.[10] Intramolecular crosslinking can further decrease this already low activity. On the contrary, M13+BSA+GA hybrid microgels maintained their infectivity and the corresponding patch formed lysis zone around the edges on a lawn of *E. coli* ER2738 and sprayed microgels formed plaques on the bacteria lawn (**Supplementary Fig. 6b,** 5-6), clearly indicating antimicrobial activity. The non-infectivity of BSA+GA microgels confirmed that the bioactivity of M13+BSA+GA microgels is not bound to BSA or reacted crosslinker (**Supplementary Fig. 6b,** 7-8). Therefore, it is possible that the abundant amino groups and carboxyl groups offered by BSA, consumed excessive crosslinker molecules, minimizing the intramolecular crosslinking within phages and eventually protecting the bioactivity of phages. FE-SEM imaging showed the bacterial-binding sites, g3p, were displayed on the surface of phage microgels, so these microgels were expected to bind multiple *E. coli* ER2738 as shown in the schematic image **Fig. 4a**. Even though M13+BSA microgels successfully retained the bactericidal ability, the hybrid phage microgels cannot kill *E. coli* sufficiently considering that M13 is a weakly antimicrobial phage to begin with.[37] **Supplementary Fig. 6c** shows that adding M13+BSA microgels to a ER2738-contaminated nutrient environment cannot prevent the growth of *E. coli*, again indicating that a stronger virulent phage should be used for bactericidal activity. It is noteworthy that M13 is an attractive phage for use as structural component (mainly due to its shape and readily available toolkits for genetic engineering) but is not commonly the phage of choice for biocontrol of bacterial contamination/infections where bactericidal activity is desired.

Integrating phages as microgels was expected to offer four main advantages compared to applying a phage suspension for biocontrol. One is the desiccation control. Another is that microgels can achieve very high local concentration. We calculated that based on the titer of phage suspension needed to fabricate microgels (5×10^{13} PFU/mL), each microgel contains more than 3.8×10^{5} of M13 phages. This not only benefits the antimicrobial application, but also provides massive recognition sites when using modified phages to construct microgel biosensors. Additionally, the nanofibrous structure of M13 phage microgels provides strong loading capacity to load other antimicrobial factors, such as antibodies, small molecule inhibitors or other bacteriophages. Finally, microgels offer a higher surface area compared to a bulk microgel, thus increasing the contact area between phage and its bacterial host which is expected to increase the antibacterial potency of the microgel over the same weight of bulk hydrogel.

4.3.6 Hybrid phage microgels targeting multidrug-resistant bacteria

We embedded our microgels with strong virulent phages to enhance the bactericidal ability of our microgels. Virulent phages, a class of phage with strong antimicrobial action, are different in physical structure and mechanism of antibacterial action than filamentous phage. Preserving the antibacterial action of virulent phages inside the gels, however, is a major challenge because their host recognition/binding sites are often located asymmetrically on tip of their tail fibers (such as phage HER262 and T7 which were previously shown in **Fig. 4a**). The relatively fragile tail fibers can be easily damaged through processing, or blocking. We addressed this challenge by not only optimizing the

chemistry, but also by working at the microscale, thus increasing the surface area for phage action.

To minimize the intramolecular crosslinking within phages, we decreased the concentration of GA from 0.1 M to 0.02 M. At this low concentration of crosslinker, the phage suspension cannot gel without the presence of BSA. The first virulent phage we added to the M13+BSA microgels was phage HER262 (1×10^{10} PFU/mL) that targets multidrug-resistant *E. coli* O157:H7, a common bacterial contaminant on meats and lettuces[38,39]. The SEM images confirmed the formation of hybrid microgels (**Supplementary Fig. 7**). Comparing to the capsulated nanofibrous structure of M13+BSA+GA microgels (**Fig. 2e**), the surface nanostructure of M13+HER262+BSA+GA microgels displayed nanodots matching the capsid size of phage HER262 (~50 nm), supporting retention of HER262 antimicrobial activity through its ability to target *E. coli* O157:H7. As shown in **Fig. 4b**, the unseparated hybrid phage HER262 microgels in the patch formed lysis zones on the lawns of both *E. coli* ER2738 and *E. coli* O157:H7. The microgel formed clear plaques, indicative of antimicrobial activity, when sprayed on both lawns (**Fig. 4c**).

To evaluate the bacteria-killing ability of our microgels in liquid, we incubated *E. coli* O157:H7 and phage microgels together in two environments: phosphate-buffered saline (PBS) simulating a nutrient-deficient environment, and nutrient tryptic soy broth (TSB) simulating a nutrient-rich environment.

For the nutrient-deficient environment, we used PBS to dilute the pre-culture into 10^8, 10^7, 10^6, and 10^5 CFU/mL. Phage microgels were then added to the diluted bacterial

suspensions at a final concentration of ~1500 microgels/mL. As shown in **Fig. 4d**, *E. coli* O157:H7 maintained the same concentration level in PBS without microgels after 9 hrs. On the contrary, when microgels were added, they killed all bacteria within 9 hrs when the initial concentration of *E. coli* O157:H7 was below 10^7 CFU/mL, and decreased the concentration 6 logs when initial concentration was high, 10^8 CFU/mL.

In nutrient TSB, phage microgels also showed the ability to prevent bacterial growth, but at a much faster rate. This is expected because the phage antimicrobial activity is closely tied to the physiological state of the host bacteria. We used TSB to dilute the pre-culture into 10^8, 10^7, 10^6 CFU/mL and monitored the optical density at a wavelength of 600 nm (OD_{600}) in the suspension to evaluate bacterial growth. As shown in **Fig. 4e**, the phage microgels restrained the increase of OD_{600} in 4 hrs regardless at high and low contamination loads. We further quantified the bacterial titers after 9 hrs (**Fig. 4f**). Phage microgels prevented the growth of *E. coli* O157:H7, maintaining the bacterial titer between 10^6 and 10^7 CFU/mL while all the controls reached 10^9 CFU/mL.

In summary, phage microgels displayed excellent antimicrobial ability regardless of nutrient in the environment, especially in the nutrient-deficient environment where bacterial propagation was inhibited. Moreover, to demonstrate specific bactericidal activity of our microgels, we incubated phage microgels with ER2738 and BL21 at the initial titer of 10^6 CFU/mL and the bacterial solutions showed same strong growing trend regardless of the participation of microgels (**Supplementary Fig. 8**), illustrating the specific targeting of these microgels.

We confirmed that the antimicrobial activity was independent of the phage used, as long as a virulent phage was used, by demonstrating the results with the virulent phage T7 (**Supplementary Fig. 9a**). The patch and spray made with T7-embedded phage microgels showed lysis zones on the lawn of BL21 (**Supplementary Fig. 9b**). And the microgels can decrease the titer of BL21 by at least 6 logs (**Supplementary Fig. 9c**). In nutrient TSB solution, T7-embedded phage microgels can still prevent the bacterial growth and caused a 5 log difference (**Supplementary Fig. 9d-e**), which proved the strong function of phage microgels as delivery vehicle.

4.3.7 Phage microgel spray for food product safety

After verifying the antimicrobial activity of HER262-embedded phage microgels against *E. coli* O157:H7, we used these microgels to inhibit bacterial contamination in two completely different food matrices. As illustrated in **Fig. 4g**, the lettuce was first contaminated with *E. coli* O157:H7 at 10^6 CFU/g, followed by spraying with phage microgels. The lettuce was then covered with food wrap and placed in room temperature for 9 hrs. The second day, the lettuce was immersed in 10 mL of PBS and vortexed for 2 mins to collect the live bacteria. As shown in **Fig. 4h**, we cannot visually differentiate between the lettuce leaves with different treatment, but the bacterial concentration in the collected solution is significantly different. The contaminated lettuce with no microgel treatment reached an average contaminant load of 3.3×10^7 CFU/g after 9 hrs. For the contaminated lettuce sprayed with microgels, the bacterial titer dropped to undetectable level (<100 CFU/g, up to 6 log reduction). The same antimicrobial phenomenon was observed when testing artificially contaminated meat samples with a similar treatment. The

meat samples showed no visual difference. The O157:H7-contaminated meat sprayed with water reached 2.5×10^8 CFU/g, For the contaminated meat sprayed with microgels, the bacterial titer dropped to 1.4×10^5 CFU/g, indicating that the microgels killed 99.94% of the drug-resistant bacteria.

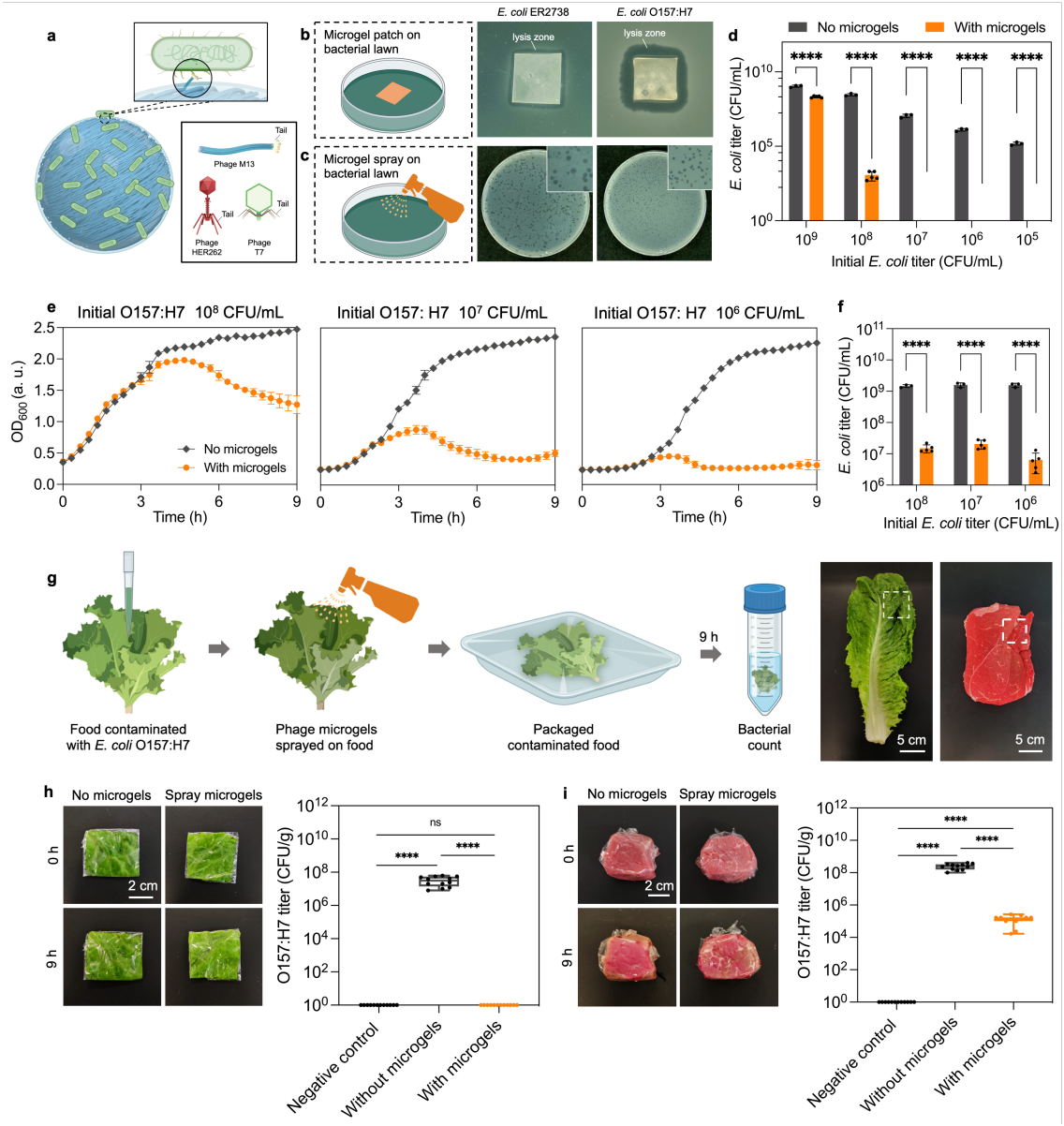

Figure 4. Antimicrobial activity of hybrid phage microgels. a, Schematic image of a phage microgel where the M13 g3p is binding to the tip of the F pilus on the host *E. coli*. Box on the bottom right: Comparison of the shapes of phage M13 (filamentous), HER262 (long tailed), T7 (short tailed). **b,** Photos of the HER262-embedded hybrid phage microgels patch arrays forming lysis zones on the lawn of both *E. coli* ER2738 and *E. coli* O157:H7. **c,** HER262-embedded hybrid phage microgels sprayed on the lawn of both *E. coli* ER2738 and O157:H7, showing clearing zones on both lawns. **d,** Titer count of *E. coli* O157:H7 incubated in PBS after 9 hrs at different initial concentration with and without HER262 microgels. **e,** Kill curves for *E. coli* O157:H7 suspension, incubated in TSB for 9 hrs at different initial concentration with and without HER262 microgels. **f,** Final titer count of the *E. coli* O157:H7 incubated in TSB after 9 hrs in part e. **g,** Left: Schematic image of microgel sprays decontaminating multidrug-resistant *E. coli* O157:H7 in lettuce. Right: pictures of lettuce and meat. White boxes indicate where we cut the lettuce and meat into small pieces. **h,** Left: pictures of wrapped artificially contaminated lettuces sprayed with water and microgels, respectively at 0 and 9 hours. Right: bacterial titer count of the collected bacterial suspension from contaminated meat. **i,** Left: pictures of wrapped artificially contaminated meats sprayed with water and microgels respectively at 0 and 9 hours. Right: bacterial titer count of the collected bacterial solution from the contaminated lettuces. (****$P<0.0001$. Statistical significance in all panels is derived from one-way analysis of variance (ANOVA). Schematics created with BioRender.com)

4.4 Conclusion

The main contribution of our work is (1) development of a high throughput method for generation of microgels and microgel arrays of pure phage, (2) the development of monodisperse phage microgels that retained the antimicrobial activity of phage, and (3) the application of the microgel patch and microgel sprays for biocontrol. The high-throughput method we propose here combined with honeycomb template casting with peel isolation, produced over 35,000 phage microgels in every square centimeter template with each microgel containing half a million phages. This method can be extended to prepare most types of microgels efficiently, but it is particularly suited to heat/solvent sensitive microgels, as it is simple, heat-free and solvent-free, which is especially useful to keep biomolecules and proteinouse materials functional. Our nanofilamentous building blocks self-assembled forming a highly aligned nanofibrous structure where single phage filaments could be observed using an electron microscope. Addition of BSA protein in microgels added additional flexibility in design, namely to tune the fluorescence and preserve M13 bioactivity. Furthermore, strong virulent phages were combined into the microgels and the resulting microgel patch, microgel spray and microgel suspension were proven highly effective in their antimicrobial action. Specifically, the contaminant load of the multidrug resistant *Escherichia coli* O157:H7 in food products were reduced by 6 logs after spraying phage microgels. We further demonstrated that aside from packing a high density of antimicrobial virions, the microgels also protected against desiccation. Every year, it is estimated that 600 million people fall ill due to the consumption of contaminated food. This attributes to 420,000 annual deaths globally and *E. coli* contamination is

considered a major factor.[40] Incorporating our antimicrobial microgels or patches into packaging, sprays in grocery store produce sections, and in household decontaminating products can effectively inhibit bacterial contamination in a human-friendly manner that will ultimately reduce foodborne illnesses, deaths and associated economic loss.

4.5 Experimental methods

4.5.1 Preparing polystyrene honeycomb film

Honeycomb films were prepared using the breath figure method, as described in detail elsewhere.[32,41] Briefly, 600 μL of 5 wt% of polystyrene (Mw=650 000, Millipore Sigma) in chloroform was cast and spread circularly on a clean glass slide in a humid chamber. The chamber was sealed immediately after adding the polystyrene solution to maintain humidity. After 20 mins, the polystyrene solution had solidified, forming a white film on the glass slide. The slides were then taken out of the chamber. After 1 h, the honeycomb film was easily peeled off and stored at room temperature.

4.5.2 Phage propagation, purification and concentrating

M13 bacteriophage was propagated using its host: *Escherichia coli* strain K12 ER2738 (New England Biolabs Ltd., E4104S). A pre-culture of *E. coli* was prepared in LB-Miller broth and placed in a shaking incubator overnight set to 180 rpm and 37 °C. The following day, 2.5 mL of the pre-culture was added to 250 mL of LB broth in a baffled flask. Subsequently, a 10 μL aliquot of M13 phage (10^{12} PFU/mL) was added to the flask to initiate the propagation. The flask was incubated in a shaking incubator set to 180 rpm and 37 °C for 5 hrs. 50 mL aliquots of propagated phage solution were then centrifuged at

7000 × g for 15 mins. The resulting bacteria pellets were discarded, and the phage-containing supernatant was stored at 4 °C.

The purification of the propagated M13 phage supernatant was achieved through an aqueous two-phase polyethylene glycol (PEG) precipitation protocol followed by an ultracentrifugal filtration, as described previously by Sambrook.[42] A 20 (w/v) % PEG solution was aseptically prepared and supplemented with 2.5 M NaCl solution. The sterile PEG solution was added in a 1:6 ratio to the propagated phage supernatant and incubated in a fridge overnight at 4°C. Subsequently, the incubated PEG-phage solutions were centrifuged at 4°C and 5000×g for 45 mins to obtain pelleted phage. The resulting phage was then resuspended in 5 mL of sterilized water and incubated overnight on a roller at 4°C. The resuspended phage was then centrifuged at 5000×g for 15 mins to remove the remaining bacterial contaminants. The described PEG/NaCl purification procedure was subsequently repeated a second time to ensure all contaminants were removed. The resulting PEG-purified phage solution was then filtered through centrifugal filters (MWCO 100 KDa and 30 KDa, Millipore Sigma, Ultra-15) to remove excess water. The final concentration was titered using plaque assay method.[43]

4.5.3 Phage microgel preparation

A polystyrene honeycomb film was used as the template to prepare the phage microgels. The film was initially plasma-coated with O_2 for 5 mins and then covered with 100 µL of the mixture of M13: 5×10^{13} PFU/mL with GA or EDC: 0.1 M. The film was subsequently placed inside a desiccator connected to a vacuum pump. The pump was turned on for 5 mins to create a low-pressure environment, which helped the phage solution fill inside the

micropores. The film was then taken out and transferred into a sealed humid container at 4 °C for 2 days.

After 2 days, a glass slide was used to remove the excess phage hydrogel on the template surface. After this cleaning step, a piece of transparent adhesive tape was adhered to the template film surface and then peeled off to remove the top layer of the template. Then the template film was immersed in 1 mL of sterilized water or PBS and sonicated for 10 mins. After the sonication, the film was taken out and discarded. The microgels were suspended in water and stored at 4 °C for further experiments.

4.5.4 Scanning Electron Microscopy

Samples were pre-treated using the critical-point drying method to dehydrate the microgels without disturbing their surface nanostructures. Samples were processed through an ethanol gradient treatment and then placed in a Leica critical point dryer (EM CPD300) for 3.5 hrs.

Two types of Scanning Electron Microscopy (SEM) were used to image the templates and microgels. TESCAN VEGA-II LSU SEM was used to image these samples, where 10 nm layers of gold were coated onto the samples in advance. A field emission scanning electron microscope (FEI Magellan 400) was used to image the nanostructure on the surface of the microgels, where 3 nm layers of Pt were coated onto the samples in advance.

4.5.5 Inverted Fluorescence Microscopy

An inverted microscope (Nikon Eclipse Ti2 inverted microscope) was used to take bright field and fluorescent images of the microgels and their templates. Four different optical filter sets (blue channel: ex/em = 340/435 nm; green channel: ex/em = 465/515 nm; orange

channel: ex/em = 528/590 nm; red channel: ex/em = 625/670 nm) were used for fluorescence imaging. The excitation filter was positioned in front of the LED light source, and the image was captured using the emission filter attached to the camera. The intensity of the light source and the exposure time were consistent.

4.5.6 Size measurement of template pores and microgels

An inverted microscope (Nikon Eclipse Ti2) was used to image the template pores and microgels. The size of pore and microgels were measured using the NIS-Elements AR software. The diameter of a template pore was defined as the diameter of the spherical hole instead of the surface pore. This is because spherical holes determine the microgel size and can easily be measured using emission light mode. For each sample, 9 images from 3 samples were captured randomly, and all pores/particles were measured to collect the diameter data.

4.5.7 Microgel preparation efficiency

The pore density of the honeycomb film was defined as the pore count divided by the film area. 9 images of 3 honeycomb films were taken using a Nikon Eclipse Ti2 inverted microscope at 40×. All pores in the frames were manually counted and the frame areas were measured using the software NIS-Elements AR.

The microgels isolated from the templates were collected in 1 mL of Millipore water. To count the number of microgels in the 1 mL suspension, a 5 μL sample was drop-cast on a glass slide, and a large image covering the entire droplet was taken using an inverted microscope. The number of microgels in this droplet $n_{5\mu L}$ was then manually counted, and

the total amount of microgel was calculated using this equation: $n_{1mL} = n_{5\mu L} \times 200$. For each type of microgel, the procedure was repeated at least 5 times.

4.5.8 Fourier transform infrared (FTIR) spectra

FTIR spectra of the phage microgels were represented under by phage hydrogel bulks made with materials exactly same as corresponding microgels. Phage hydrogels were pre-dehydrated, placed in the FT-IR Spectrometer (Nicolet 6700, Thermo Fisher Scientific) and the spectra were collected in the range of 4000-500 cm^{-1} using 128 scans at a resolution of 4 cm^{-1}.

4.5.9 Desiccation sensitivity test for phage

A 10 μL drop of phage suspension (M13, HER262 and T7, ~10^{10} CFU/mL) was added on a clean, uncovered glass slide at room temperature. The suspension was dried in 10 mins and continued to desiccate afterwards. After 1 hr, 10 μL of sterile PBS was used to resuspend the phage. The final and original concentrations of phages were titered through full plate plaque assays. The procedure was repeated in triplicate for each type of phage. Phage HER262 was purchased from the Félix d'Hérelle Reference Center for bacterial viruses of the Laval University, and T7 was from Leibniz Institute DSMZ-German Collection of Microorganisms and Cell Cultures.

4.5.10 Antimicrobial test of phage microgel patches on bacterial lawn

In this experiment, the phage microgels were not isolated from the template. Instead, the composite films were regarded as flexible antimicrobial patches, representing an ordered monolayer of phage microgels. After microgel gelation, the composite patches were washed in sterile water for 20 mins to remove free phages.

Luria-Bertani (LB) agar plates were prepared by suspending LB powder (25g/L, Fisher Scientific) in sterile water and supplemented with agar (1.5% w/v, 15g/L, Fischer Scientific) and dispensed into petri dishes (100mm x 15mm, sterile, polystyrene, Fisher Scientific) using a sterile serological pipette. Soft agar overlays were prepared by boiling sterile water supplemented with LB Broth powder (25g/L) and agar (0.6% w/v, 6g/L). A 3 mL aliquot of boiled media was dispensed into glass test tubes. Test tubes were then autoclaved to ensure sterility.

Lawns of bacterial overlay were prepared by suspending 100 μL of bacterial suspensions (*E. coli* ER2738, O157:H7, or BL21) in 3 mL of liquefied soft LB -agar, which was vortexed and poured on LB agar plates. After the soft agar was solidified, the washed patches were gently placed on top of the bacterial lawn. The double layer plates were incubated in a stationary incubator (37 ℃, VWR International Co.) overnight and subsequently imaged.

4.5.11 Antimicrobial test for phage microgel sprays on bacterial lawn

1 mL of the fresh-made phage microgel suspension was transferred into a sprayer. Phage microgel solution was then sprayed on bacterial lawns (prepared as previously described). The double layer agar plates were then incubated in a stationary incubator (37 ℃) overnight and subsequently imaged.

4.5.12 Antimicrobial test for phage microgel suspensions

Two different media, Tryptic Soy Broth (TSB) and nutrient-deficient PBS, were prepared to evaluate the bactericidal ability of phage microgels in different liquid environments.

(1) Nutrient-rich environment

Overnight bacterial cultures (*E. coli* O157:H7 or BL21, ~10^9 CFU/mL), grown in TSB, were diluted to 1:10, 1:100 and 1:1000 in fresh TSB media. For each dilution and the original overnight culture, 10 replicates of 200 μL bacterial solution were added to a sterile 96-well plate. A 10 μL aliquot of the phage microgel suspension was then added to each of the first five replicates as the sample group (labelled "With microgels"). A 10 μL drop of sterile PBS was added to the remaining five replicates as the control group (labelled "No microgels"). Subsequently, the 96-well plate was placed in a microplate reader (Synergy Neo2 Hybrid Multi-Mode Reader, 37 ℃, 180 rpm) to measure optical density at a wavelength of 600 nm (OD_{600}) every 20 mins for 9 hrs. Bacterial CFU counts of each replicate were obtained at the end point.

(2) Nutrient-deficient environment

Overnight bacterial cultures (*E. coli* O157:H7 or BL21, ~10^9 CFU/mL) grown in TSB were diluted to 1:10, 1:/100, 1:1000 and 1:10000 in PBS. For each dilution and the original overnight culture, 10 replicates of 200 μL bacterial solution were added to a sterile 96-well plate. A 10 μL aliquot of the phage microgel suspension was then added to each of the first five replicates as the sample group (named "With microgels"). A 10 μL drop of sterile PBS was added to the remaining five replicates as the control group (named "No microgels"). Afterwards, the 96-well plate was placed in a shaking incubator (Thermo Scientific, 37 ℃, 180 rpm) for 9 hrs, and the bacterial titer count of each sample at the end point was calculated.

4.5.13 Food decontamination test of phage microgels

Lettuce (romaine heart) was purchased at the local supermarket and cut into 6 squares weighing 0.4±0.01 g. Then 4 of those were contaminated with *E. coli* O157:H7, reaching a contamination level of 10^6 CFU/g. A 200 μL aliquot of the phage microgel suspension was then sprayed onto two contaminated leaves directly while the other two contaminated leaves were sprayed with sterile water. The remaining two leaves served as controls and were wrapped by food wraps without treatment. All 6 lettuce squares were wrapped and placed at room temperature for 9 hrs. The lettuce squares were then immersed in 10 mL of sterile PBS. Then, the samples were unwrapped and immersed in 4 mL of sterile PBS. This mixture was vortexed for 2 mins to dislodge bacteria and the titer was determined using standard colony count. MacConkey-Sorbitol ChromoSelect Agar (Millipore Sigma) plates were used for selective O157:H7 titer count[44] (Detection limit: 100 CFU/g).

The decontamination test for beef steaks (Canadian beef, AAA Angus) followed a similar protocol. Beef steaks were cut into 6 cubes weighing 3±0.1 g. A 30 μL aliquot of *E. coli* O157:H7 (10^8 CFU/mL) was added to 4 meat cubes to achieve a contamination level of 10^6 CFU/g. A 200 μL aliquot of the phage microgel suspension was then sprayed onto 2 contaminated meat cubes directly while the other 2 contaminated cubes were sprayed with sterile Millipore water. The remaining 2 cubes served as controls and were wrapped by food wraps without treatment. The 6 meat cubes were placed at room temperature for 9 hrs. The samples were then unwrapped and immersed in 10 mL of sterile PBS. This mixture was vortexed for 2 mins to dislodge the bacteria and bacteria titer was determined using standard colony counts (Detection limit: 34 CFU/mL).

4.6 Acknowledgements

This research was undertaken, in part, thanks to funding from the Canada Research Chairs Program (TFD and ZH).L.T., K.J., and Z.H. acknowledge funding from Natural Sciences and Engineering Research Council of Canada (NSERC) Discovery Grants Program and the Boris Family Fund for Health Research. S.K. is funded by a Vanier Canada Graduate Scholarship awarded by the Natural Sciences and Engineering Research Council.

4.7 Author contributions

L.T. conceived the study, designed and executed the experiments, analyzed the data, prepared the figures, and contributed to writing the manuscript. L.H. and K.J. made important contributions to phage purification, microgel preparation and antimicrobial tests. A.S. and Z.W. performed some antimicrobial tests and contributed to data analysis. S.K. and T.D. contributed to the food tests. Z.H. conceptualized and supervised the project, and guided the experimental design, data analysis and manuscript writing.

4.8 Competing interests

Authors declare no competing interest.

4.9 References

1. Salmond, G. P. C. & Fineran, P. C. A century of the phage: Past, present and future. *Nat. Rev. Microbiol.* **13**, 777–786 (2015).
2. Meng, R. *et al.* Structural basis for the adsorption of a single-stranded RNA bacteriophage. *Nat. Commun.* **10**, (2019).
3. Hsu, B. B. *et al.* Dynamic Modulation of the Gut Microbiota and Metabolome by Bacteriophages in a Mouse Model. *Cell Host Microbe* **25**, 803-814.e5 (2019).
4. World Health Organization. WHO's first ever global estimates of foodborne diseases find children under 5 account for almost one third of deaths. (2015). Available at: https://www.who.int/news/item/03-12-2015-who-s-first-ever-global-estimates-of-foodborne-diseases-find-children-under-5-account-for-almost-one-third-of-deaths. (Accessed: 7th February 2022)

5. Food and Drug Administration. GRAS notice 755, Preparation containing two bacterial phages specific to *Escherichia coli* O157. (2018). Available at: https://www.fda.gov/media/117249/download. (Accessed: 24th August 2021)
6. Food and Drug Administration. GRAS Notice 834, Preparation containing bacterial phages specific to shiga-toxin producing *Escherichia coli*. (2019). Available at: https://www.fda.gov/media/133519/download. (Accessed: 24th August 2021)
7. Lucera, A., Costa, C., Conte, A. & Del Nobile, M. A. Food applications of natural antimicrobial compounds. *Front. Microbiol.* **3**, 1–13 (2012).
8. Wang, X. *et al.* Phage combination therapies for bacterial wilt disease in tomato. *Nat. Biotechnol.* **37**, 1513–1520 (2019).
9. Moye, Z. D., Woolston, J. & Sulakvelidze, A. Bacteriophage applications for food production and processing. *Viruses* **10**, 1–22 (2018).
10. Bayat, F., Didar, T. F. & Hosseinidoust, Z. Emerging investigator series: bacteriophages as nano engineering tools for quality monitoring and pathogen detection in water and wastewater. *Environ. Sci. Nano* **8**, 367–389 (2021).
11. Smith, G. P. Filamentous Fusion Phage : Novel Expression Vectors that Display Cloned Antigens on the Virion Surface. *Science* **228**, 1315–1317 (1985).
12. Souza, G. R. *et al.* Three-dimensional tissue culture based on magnetic cell levitation. *Nat. Nanotechnol.* **5**, 291–296 (2010).
13. Chung, W. J. *et al.* Biomimetic self-templating supramolecular structures. *Nature* **478**, 364–368 (2011).
14. Oh, J. W. *et al.* Biomimetic virus-based colourimetric sensors. *Nat. Commun.* **5**, 1–8 (2014).
15. Peivandi, A., Tian, L., Mahabir, R. & Hosseinidoust, Z. Hierarchically Structured, Self-Healing, Fluorescent, Bioactive Hydrogels with Self-Organizing Bundles of Phage Nanofilaments. *Chem. Mater.* **31**, 5442–5449 (2019).
16. Peivandi, A. *et al.* Inducing Microscale Structural Order in Phage Nanofilament Hydrogels with Globular Proteins. *ACS Biomater. Sci. Eng.* In press (2021).
17. Jackson, K., Peivandi, A., Fogal, M., Tian, L. & Hosseinidoust, Z. Filamentous Phages as Building Blocks for Bioactive Hydrogels. *ACS Appl. Bio Mater.* **4**, 2262–2273 (2021).
18. Guan, Y. & Zhang, Y. PNIPAM microgels for biomedical applications: From dispersed particles to 3D assemblies. *Soft Matter* **7**, 6375–6384 (2011).
19. Rossow, T. *et al.* Controlled synthesis of cell-laden microgels by radical-free gelation in droplet microfluidics. *J. Am. Chem. Soc.* **134**, 4983–4989 (2012).
20. Seiffert, S. & Weitz, D. A. Microfluidic fabrication of smart microgels from macromolecular precursors. *Polymer (Guildf).* **51**, 5883–5889 (2010).
21. Yun, Y. H., Goetz, D. J., Yellen, P. & Chen, W. Hyaluronan microspheres for sustained gene delivery and site-specific targeting. *Biomaterials* **25**, 147–157 (2004).
22. Mao, A. S. *et al.* Deterministic encapsulation of single cells in thin tunable microgels for niche modelling and therapeutic delivery. *Nat. Mater.* **16**, 236–243 (2017).
23. Headen, D. M., Aubry, G., Lu, H. & García, A. J. Microfluidic-based generation of size-controlled, biofunctionalized synthetic polymer microgels for cell encapsulation. *Adv. Mater.* **26**, 3003–3008 (2014).

24. Li, F., Lyu, D., Liu, S. & Guo, W. DNA Hydrogels and Microgels for Biosensing and Biomedical Applications. *Adv. Mater.* **32**, 1–9 (2020).
25. Leung, V., Groves, L., Szewczyk, A., Hosseinidoust, Z. & Filipe, C. D. M. Long-Term Antimicrobial Activity of Phage-Sugar Glasses is Closely Tied to the Processing Conditions. *ACS Omega* **3**, 18295–18303 (2018).
26. Hsu, B. B. *et al.* In situ reprogramming of gut bacteria by oral delivery. *Nat. Commun.* **11**, 1–11 (2020).
27. Grabarek, Z. & Gergely, J. Zero-length crosslinking procedure with the use of active esters. *Anal. Biochem.* **185**, 131–135 (1990).
28. Timkovich, R. Detection of the stable addition of carbodiimide to proteins. *Anal. Biochem.* **79**, 135–143 (1977).
29. Chung, W. J., Lee, D. Y. & Yoo, S. Y. Chemical modulation of M13 bacteriophage and its functional opportunities for nanomedicine. *Int. J. Nanomedicine* **9**, 5825–5836 (2014).
30. Li, X. *et al.* A Bottom-Up Approach To Fabricate Patterned Surfaces with Asymmetrical TiO2 Microparticles Trapped in the Holes of Honeycomblike Polymer Film. 3736–3739 (2011). doi:10.1021/ja1106767
31. Widawski, G. & Rawiso, M. Self-organized honeycomb morphology of star-polymer polystyrene films. *Nature* **369**, 387–389 (1994).
32. Zhu, C., Tian, L., Liao, J., Zhang, X. & Gu, Z. Fabrication of Bioinspired Hierarchical Functional Structures by Using Honeycomb Films as Templates. *Adv. Funct. Mater.* **28**, 1–8 (2018).
33. Daly, R., Sader, J. E. & Boland, J. J. Taming Self-Organization Dynamics to Dramatically Control Porous Architectures. *ACS Nano* **10**, 3087–3092 (2016).
34. Takehiro Nishikawa, † *et al.* Fabrication of Honeycomb Film of an Amphiphilic Copolymer at the Air−Water Interface. *Langmuir* **18**, 5734–5740 (2002).
35. Wang, W. *et al.* Deterministic Reshaping of Breath Figure Arrays by Directional Photomanipulation. *ACS Appl. Mater. Interfaces* **9**, 4223–4230 (2017).
36. Wei, W. *et al.* Preparation and application of novel microspheres possessing autofluorescent properties. *Adv. Funct. Mater.* **17**, 3153–3158 (2007).
37. Waldor, M. K. & Mekalanos, J. J. Lysogenic conversion by a filamentous phage encoding cholera toxin. *Science (80-.).* **272**, 1910–1913 (1996).
38. Schroeder, C. M. *et al.* Antimicrobial resistance of *Escherichia coli* O157 isolated from humans, cattle, swine, and food. *Appl. Environ. Microbiol.* **68**, 576–581 (2002).
39. Rafiq Ahmed , Cheryl Bopp, Al Borczyk, S. K. Phage-Typing Scheme for Escherichia coli O157:H7. *J. Infect. Dis.* **155**, 806–809 (1987).
40. World Health Organization. Food safety. (2020). Available at: https://www.who.int/news-room/fact-sheets/detail/food-safety. (Accessed: 24th August 2021)
41. Tian, L., He, L., Jackson, K., Mahabir, R. & Hosseinidoust, Z. Bacteria repellent protein hydrogel decorated with tunable, isotropic, nano-on-micro hierarchical microbump array. *Chem. Commun.* **57**, 10883–10886 (2021).
42. McCuen, R. Molecular cloning: a laboratory manual. *Cold spring Harb. Lab. Press* **186**, 182–183 (1990).

43. Kropinski, A. M., Mazzocco, A., Waddell, T. E., Lingohr, E. & Johnson, R. P. Enumeration of bacteriophages by double agar overlay plaque assay. *Bacteriophages: Methods and Protocols, Volume 1: Isolation, Characterization, and Interactions* **501**, (2009).
44. March, S. B. & Ratnam, S. Sorbitol-MacConkey medium for detection of *Escherichia coli* O157:H7 associated with hemorrhagic colitis. *J. Clin. Microbiol.* **23**, 869–872 (1986).

Chapter 4 Appendix: Supplementary Information

4.10 Supplementary notes

4.10.1 Evaluating preparation efficiency of phage microgels

Firstly, the size of honeycomb film Stemplate was measured before microgel isolation (Supplementary Fig. 3a). After collecting all the microgels into 1 mL of water from the peeled template, we dropped 5 μL of microgel suspension on the glass slide and snapped high-resolution images (Supplementary Fig. 3b-c). Then the amount of microgels in that droplet (Nmicrogel) was counted, and the microgel preparation efficiency was calculated: $\eta = N_{microgel} \times 200/S_{template}$.

4.10.2 Test of specific targeting ability and desiccation sensitivity of phages

For example, phages M13 (*Inoviridae*, filamentous), HER262 (*Myoviridae*, long tailed), and T7 (*Podoviridae*, short tailed), are all *E. coli* phages and they cannot infect other bacterial species such as *Staphylococcus aureus* (**Supplementary Fig. 5**). From the three *E. coli* strains we evaluated, M13 phage formed mild clearing zones on the lawns of *E. coli* ER2738 and *E. coli* BL21, while phage HER262 showed lysis zones on strains ER2738 and O157:H7. Phage T7 was able to significantly lyse *E. coli* ER2738 and *E. coli* BL21. It is noteworthy that the highly specific bactericidal action of phages means that to control the population of multiple species, a mixture of phages has to be used.[1] However, the advantage of this specific killing action is preserving the beneficial bacteria in food that are responsible for maintaining the taste and texture of many food products.[2,3]

4.11 Supplementary figures

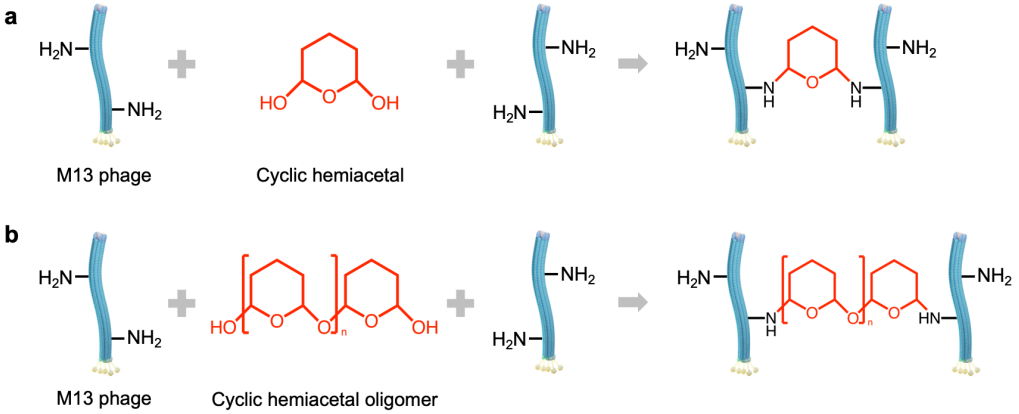

Supplementary Figure 1. The crosslinking reactions between M13 phage and the other formations of GA in aqueous solution. a, Two M13 phages react with cyclic hemiacetal and incorporate. **b**, Two M13 phages react with cyclic hemiacetal and incorporate.

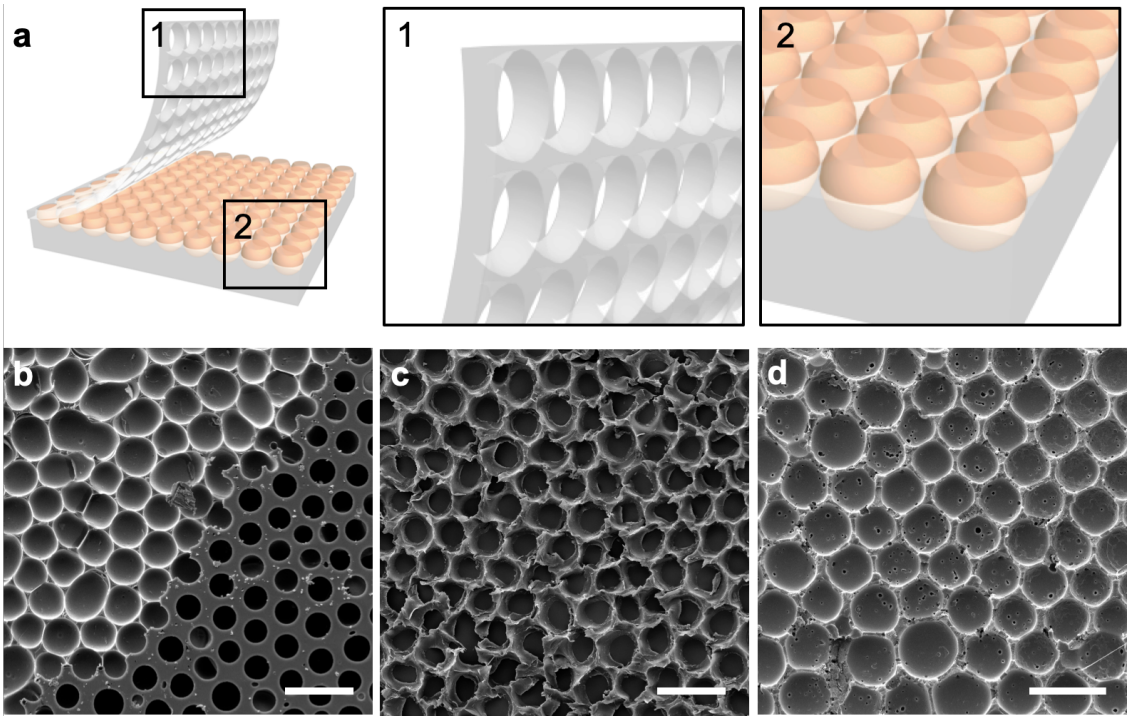

Supplementary Figure 2. The isolation of phage microgels. a, Detailed Schematic image of the peeling process: the top half of the pores was removed and the microgels inside the film were exposed on the bottom film layer without damage. **b**, SEM image of the edge of peeling area of the honeycomb film: The peeled area is on the top left presenting shallow pores and the unpeeled area is on the bottom right showing deep spherical pores. **c**, large-scale SEM image of the adhesive tape after peeling. Scale bar: 50 μm. **d**, large-scale SEM image of the honeycomb film after peeling; Scale bar: 50 μm.

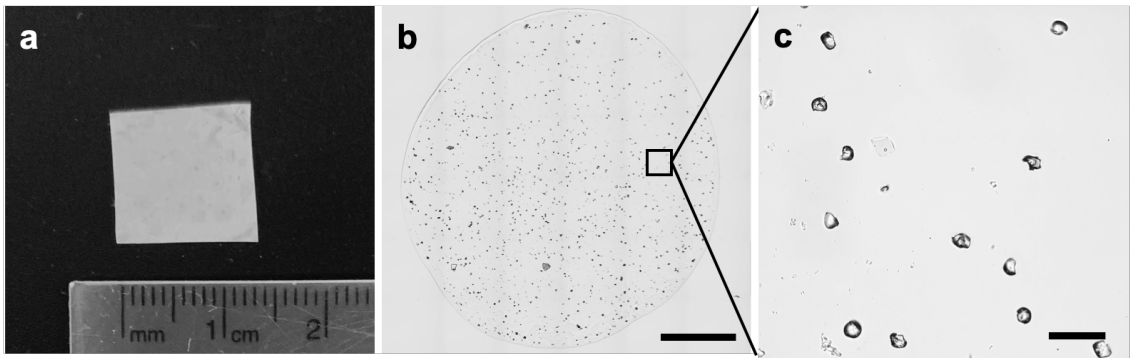

Supplementary Figure 3. The evaluation of microgel preparation efficiency. a, Image of the honeycomb film with microgels inside with rule for film area measurement. **b**, Bright field image of 5 μl of phage microgel suspension for microgel count. Scale bar: 1 mm. **c**, Zoom-in bright field image of **b** showing free-stand microgels. Scale bar: 100 μm.

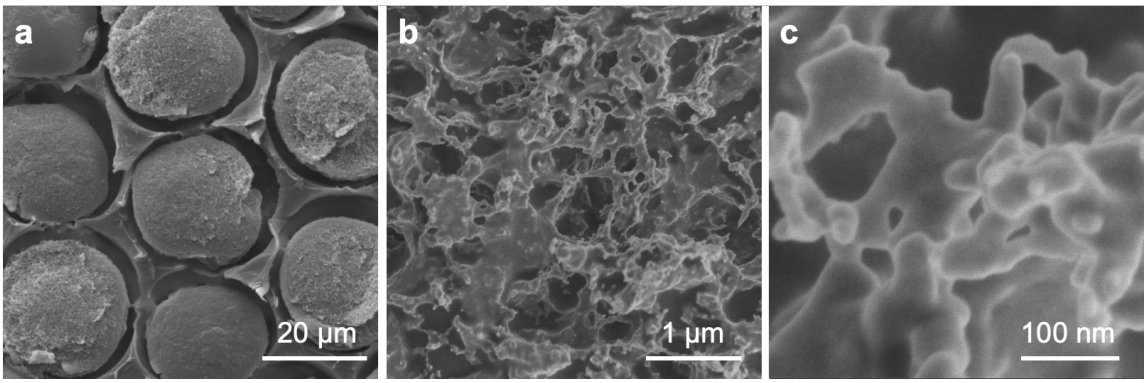

Supplementary Figure 4. Nanostructure of the BSA microgel. a, SEM image of BSA microgels crosslinked by GA in peeled honeycomb template. **b,** Nanostructure on the surface of a BSA microgel. **c,** Zoom-in image of image **b**.

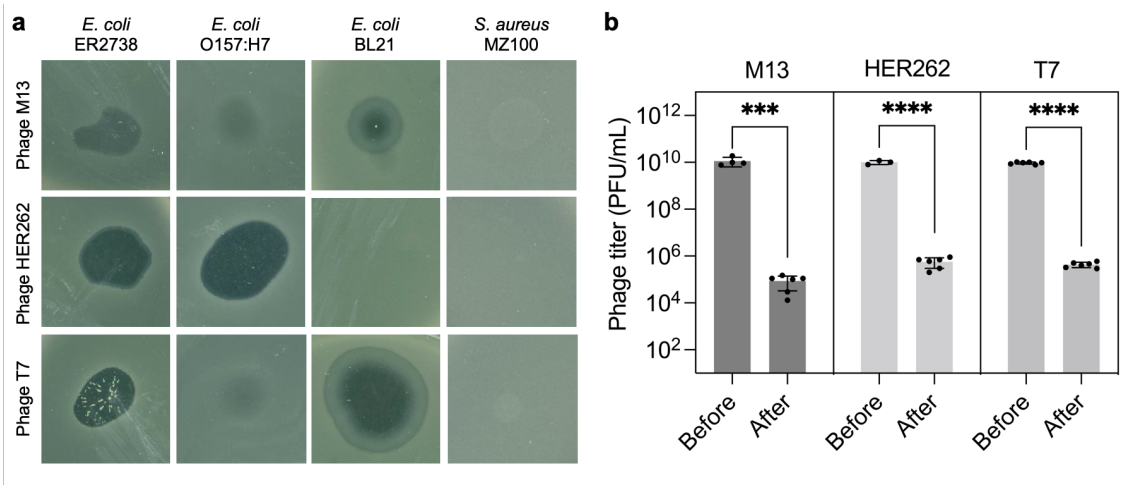

Supplementary Figure 5. Specific infectivity and desiccative sensitivity of phage M13, HER262 and T7. a, Infectivity of phage M13, HER262 and T7 to four types of bacterial strains. **b,** Titer count of phage M13, 8 and T7 before and after desiccation for 1 h. (***P<0.001, ****P<0.0001)

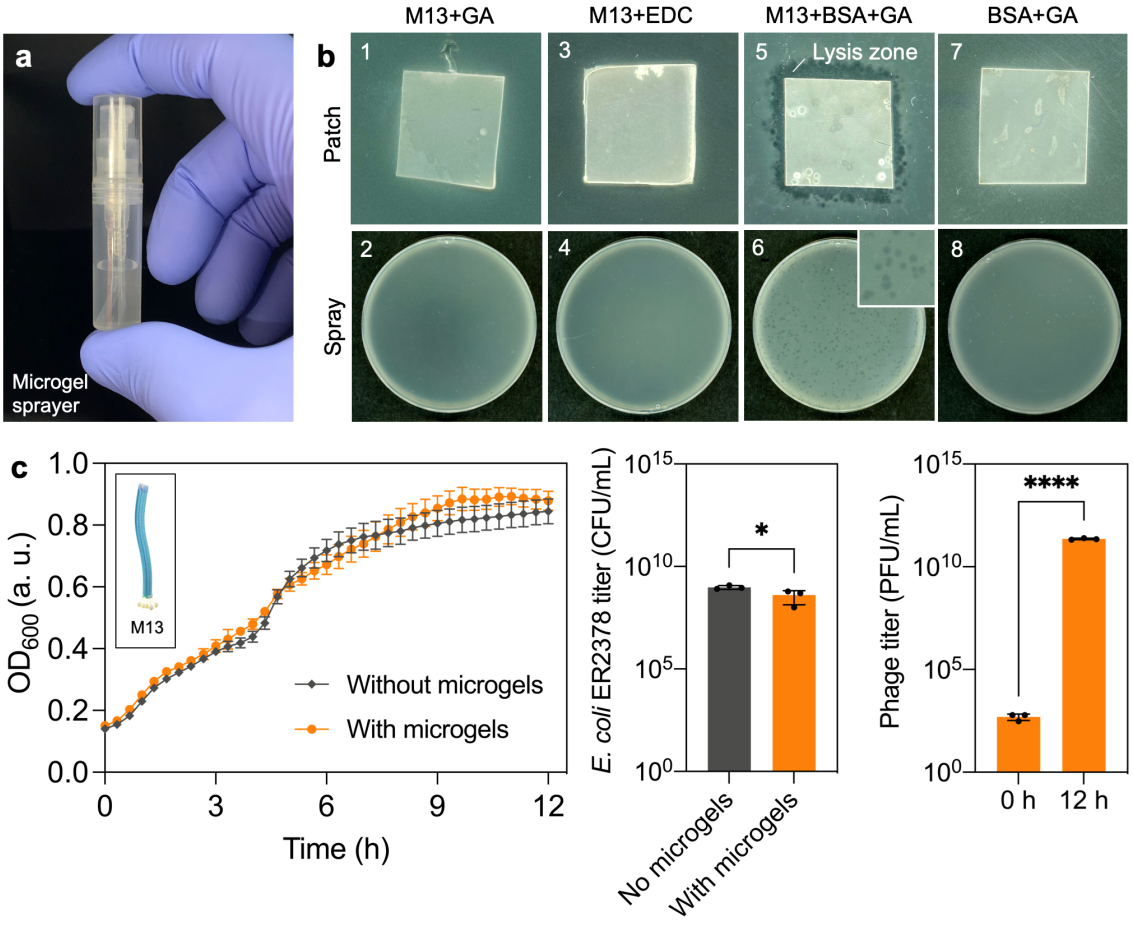

Supplementary Figure 6. Antimicrobial property of 3 types of phage microgels. a, Photo of the sprayer containing phage microgel suspension. **b,** Patches and sprayed microgels on the lawn of *E. coli* ER2738. **c,** Left: Growth curve of *E. coli* ER2738 in LB solution with and without adding microgels. Box on the top left: Schematic of the phage component in these microgels. Middle: Titer count of *E. coli* ER2738 after incubating 12 hours in LB with and without microgels; Right: Titer count of phage M13 in the *E. coli* ER2738 LB solution with microgels at 0 and 12 h. (*P<0.05, ****P<0.0001)

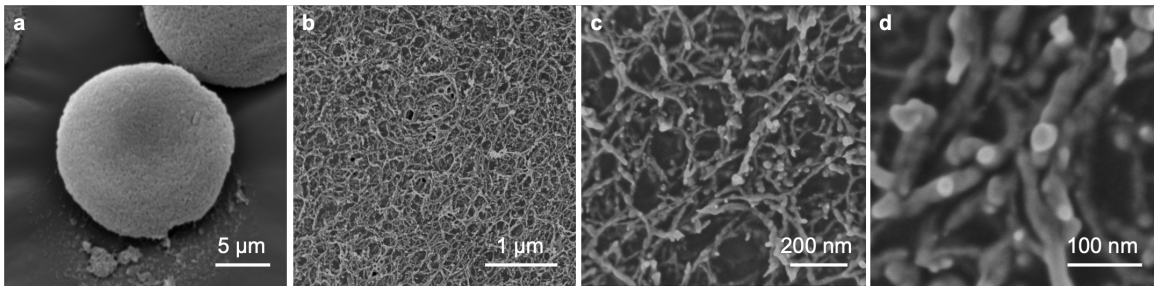

Supplementary Figure 7. Nanostructure of M13+HER262+BSA+GA hybrid phage microgels. a, SEM images of a M13+HER262+BSA+GA microgel. **b-d,** SEM images of nanostructure on the surface of the microgel.

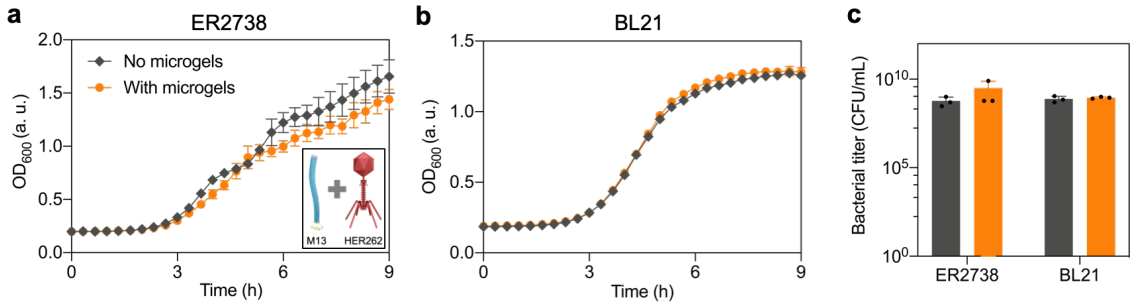

Supplementary Figure 8. M13+HER262+BSA+GA hybrid phage microgels incubating with other *E. coli* strains. a, Optical density growth of *E. coli* ER2738 (10^6 CFU/mL) incubated in TSB during 9 hours with and without phage HER262 microgels. Box on the bottom right: Schematic of the 2 phage components in these microgels. **b,** Optical density growth of *E. coli* BL21 (10^6 CFU/mL) incubated in TSB during 9 hours with and without phage HER262 microgels. **c,** Final titer count of the *E. coli* ER2738 and BL21 incubated in TSB after 9 hours in figure **a-b**.

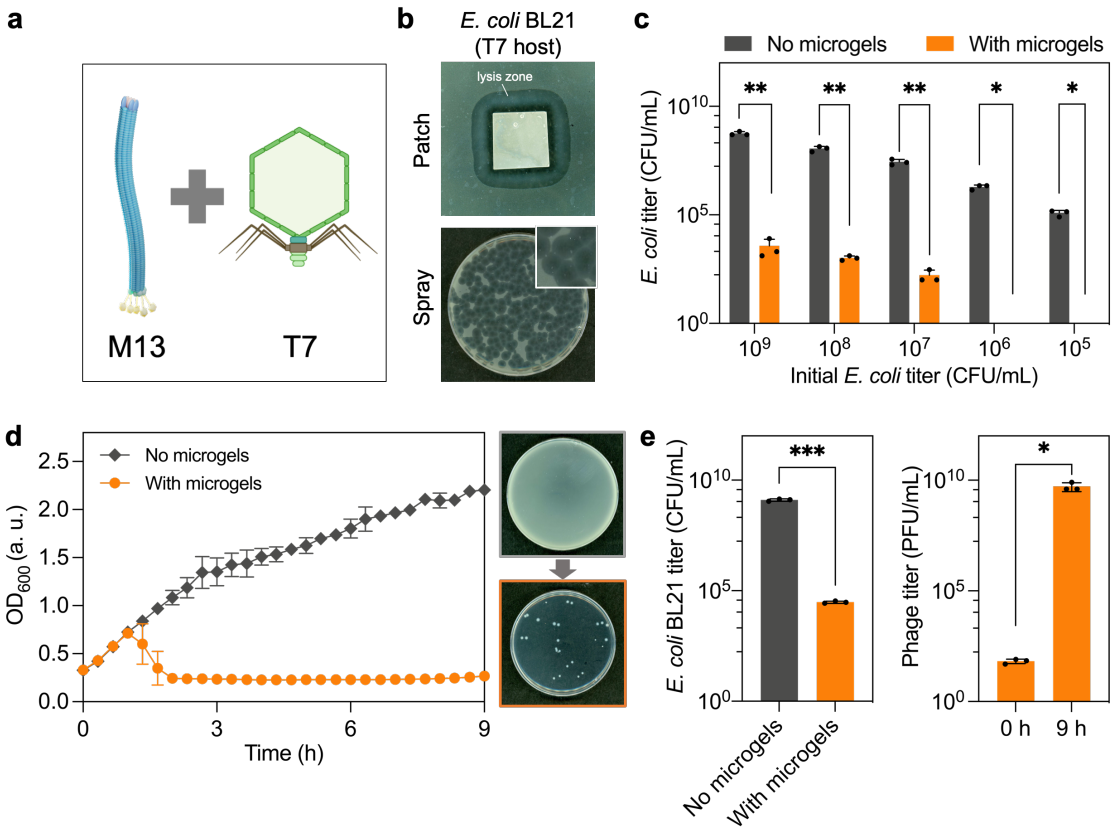

Supplementary Figure 9. Antimicrobial property of M13+T7+BSA+GA hybrid phage microgels. a, Schematic of the 2 phage components in these microgels. **b,** Photos of the hybrid T7 microgels in the patches and spray on the lawn of *E. coli* BL21. **c,** Titer count of *E. coli* BL21 incubated in PBS after 9 hours at different initial concentration with and without T7 microgels. **d,** Left: Optical density growth of *E. coli* ER2738 (10^6 CFU/mL) incubated in TSB during 9 hours with and without T7 microgels. Right: Compact bacterial lawn and sporadic colonies formed by the bacterial solution incubated without and with microgels respectively. **e,** Titer count of the BL21 in TSB after 9 hours incubated with and without microgels. (*P<0.05, **P<0.01, ***P<0.001)

4.12 References

1. Kifelew, L. G. *et al.* Efficacy of phage cocktail AB-SA01 therapy in diabetic mouse wound infections caused by multidrug-resistant *Staphylococcus aureus*. *BMC Microbiol.* **20**, 1–10 (2020).
2. Guenther, S. & Loessner, M. J. Bacteriophage biocontrol of Listeria monocytogenes on soft ripened white mold and red-smear cheeses. *Bacteriophage* **1**, 94–100 (2011).
3. Perera, M. N., Abuladze, T., Li, M., Woolston, J. & Sulakvelidze, A. Bacteriophage cocktail significantly reduces or eliminates Listeria monocytogenes contamination on lettuce, apples, cheese, smoked salmon and frozen foods. *Food Microbiol.* **52**, 42–48 (2015).

Chapter 5: Three-Level Hierarchical Wrinkle Morphologies on Functional Viral Microdot Arrays

In the previous chapter, we demonstrated that microscale phage materials can be produced with honeycomb templates. However, the templates limited the size and shape of obtained phage microgels, and the need remains to develop approaches to construct further micro- and nano- structures on phage microbeads. In this chapter, we focus on fabricating phage microdots through inkjet printing without template. A new pressure-induced method is created to prepare tunable wrinkled morphologies on phage microdots. The unique structural advantages of using phages as building blocks facilitate the understanding of phage-assembling behaviour.

In this chapter, experiments were performed by Lei Tian with the exception of bacteria-sensing evaluation performed by Shadman Khan. The chapter was drafted by Lei Tian and subsequently edited by Dr. Zeinab Hosseinidoust and Dr. Tohid Didar. This chapter and the supporting information will be submitted to Nature Nanotechnology.

Three-Level Hierarchical Wrinkle Morphologies on Functional Viral Microdot Arrays

Lei Tian, Shadman Khan, Ahmed Saif, Kyle Jackson, Amid Shakeri, Tohid Didar, Zeinab Hosseinidoust

Manuscript in preparation

5.1 Abstract

Bacterial viruses (bacteriophages) are an endless source of functional, self-propagating, monodisperse nanoparticles. Among them, filamentous bacteriophages are of particular interest for the bottom-up design of self-assembled virus-based biointerfaces. Here, we present a technology to create diverse functional hierarchically wrinkled morphologies on three-dimensional phage hydrogel microarrays through heat and solvent independent substrate-shrinkage. We printed ordered microarrays of phage bioinks with self-organizing nanofilaments that gelled *in-situ,* forming phage-exclusive and phage-DNAzyme hybrid soft microdots with a three dimensional structure and tunable size and functionality. The already sophisticated nanostructures of the phage microdots was preserved and transformed into an unique three-level hierarchical micro/nano-structure through the proposed heat-free shrinkage approach. The phage nanofilaments (width: 7 nm) self-assembled into nanobundles (width: 100 nm) that were orderly aligned on tunable microscale wrinkles (width: 0.7-5.0 μm). Our shrinking process proved to be a universal method to induce hierarchical structures on three dimensional soft proteinaceous material, as well as the archetypal monolayer of small molecules, but is particularly powerful for proteinaceous macromolecules/nanoparticles with heat sensitive nanoscale order.

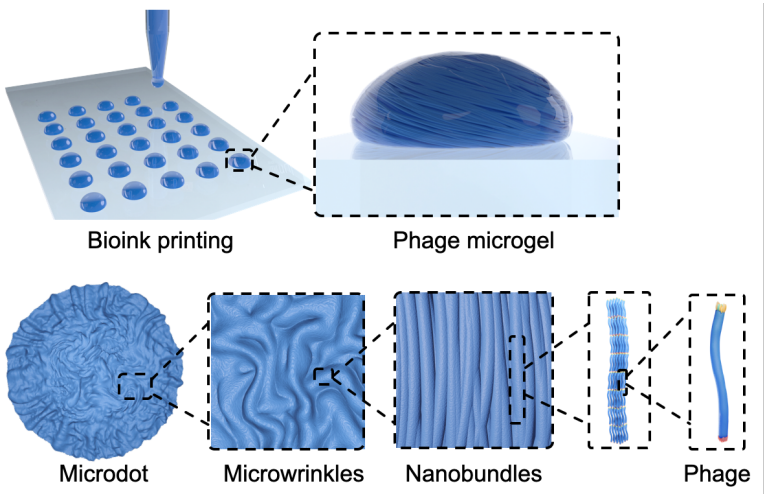

Graphic abstract. Bioink printing to produce ordered arrays of phage microgels which can form three-level hierarchical structures through nanoarchitecture-friendly substrate shrinkage method.

5.2 Introduction

As the largest community of organisms in the biosphere, bacteriophages are specific viral predators of bacteria.[1,2] Discovered over a century ago, bacteriophage have been central to groundbreaking advancements in molecular biology, investigated extensively for the treatment of antibiotic-resistant infectious diseases in humans and animals, and used as a powerful tool for investigation of natural and directed evolution, the latter leading to the Nobel prize winning technology of phage display.[3] However, their capacity as building blocks for advanced materials has been understudied until the last twenty years.[4,5] Phages offer unique properties as bionanoparticles, including monodisperse self-replication, immense diversity in shape and size, and precise control of surface chemistry through chemical and genetic modification.[6,7] In addition, nanofilamentous phages have

demonstrated self-organization at high concentrations, forming liquid crystals[8] and have thus garnered attention as candidates for building blocks of functional biomaterials.[9] Previous work has shown that phages can self-organize into bulk hydrogels[10,11], films[4,12] and microgels.[13] There remains, however, significant untapped potential in phages as self-organizing, functional building blocks for advanced functional interfaces.

A notable area of advancement in design of interfaces in general, and biointerfaces in particular is designing 3D hierarchical structures. Inspired by nature, hierarchically-structured biointerfaces have proven essential for enhancing performance in applications ranging from biosensing[14] to cell culture.[15] As one of the most versatile hierarchical structures, wrinkle structures have far-reaching functional capacities for applications as biosensors,[16,17] flexible electronic devices,[18] and adhesive/repellent surfaces.[19,20] Biointerfaces made from proteins or proteinaceous nanoparticles, however, have been entirely left out of the efforts in hierarchically structured wrinkles. Advancements on this front are partially hindered by the lack of compatible technology, with most technologies designed for inorganic material that are inherently incapable of preserving the nanoarchitecture of proteinaceous bionanoparticles building blocks. This nanoarchitecture is a valuable template for biomimetic design of interfaces.[21] Creating the wrinkled morphology directly on material surfaces requires exposure to unique stimulants,[22] or further alteration of the material's intrinsic properties. Another common method to induce the wrinkles is utilizing the mismatching deformation of the materials and a shrinkable substrate, which is commonly triggered by heat[17,20,23,24] and solvents.[25,26] The heat-induced substrate-shrinkage and solvent-induced swelling-shrinkage can efficiently create wrinkle

patterns, but is known to denature and destruct the structure of the viral capsid. Viral material platforms are the next frontier for creating hierarchical biointerfaces and a universal method to induce wrinkled structure in various biomolecule-based materials, while preserving their, is the bottleneck to achieving phage-built hierarchical biointerfaces. Herein, we developed phage microdots with unique three-level hierarchical wrinkle morphologies by developing a temperature independent substrate shrinkage technology. A phage bioink was used to print three-dimensional soft phage microarrays with controllable size on prestressed polystyrene substrates. We demonstrate a new method to create three-level wrinkled morphologies on the attached phage microdots. Diverse and controlled wrinkle patterns, Diverse wrinkle patterns, from "sunflower" to homogenous wrinkles, were further achieved by adjusting the hydrophilicity of the substrate. More importantly, the phage microdots presented an unique three-level hierarchical micro/nano-structure, proving the strong structure-preserving capability of the developed pressure shrinkage method, as opposed to heat-shrinkage, which destroyed the nanostructure.

5.3 Results and discussion

5.3.1 High-throughput printing of bacteriophage microdot arrays

We fabricated ordered arrays of phage-exclusive and phage-hybrid microdots through high-throughput printing of a simple phage bioink. The bioink consisted of filamentous phage as the building blocks, 1-Ethyl-3-(3-dimethylaminopropyl) carbodiimide (EDC) as the small-molecule crosslinker, and potentially DNAzyme as the functional molecule. While EDC facilitated the crosslinking between phages, it was not coupled into the final phage network but transferred to water-soluble byproducts which can be easily washed out

(details in **Supplementary Note 1** and **Supplementary Fig. 1**). Consequently, phage+EDC bioink led to a phage-exclusive network connected through amide bonds.

As illustrated in **Fig. 1a**, a highly-purified and concentrated suspension of the filamentous phage M13 (1×10^{14} PFU/mL) was mixed with EDC (0.1 M) as the bioink. An inkjet printer applied a small volume (as low as 0.65 nL) of bioink onto the substrate and created microdot arrays precisely and rapidly. Any flat and nonabsorbent film, such as polystyrene sheets and glass slides, are feasible to print phage ink. Herein, we applied prestressed polystyrene sheets as the substrates. After printing phage ink, the films were subsequently transferred to a sealed humid environment (relative humidity above 75%) for 12 hrs where the bioink microdots gelled and solidified into microgels. After washing out the non-reacted crosslinker and the byproducts, the microgels consisting of only crosslinked phages remained attached to the substrate. The polystyrene substrate is at this stage a flexible biochip with ordered arrays of phage-exclusive microgels (**Fig. 1b**).

The gelation of phage bioink was verified through rheological characterization (**Fig. 1c**). After depositing for 12 hrs, the ink behaved as a gel which has a distinctly higher storage modulus (G') than loss modulus (G"). Comparing the original phase, both storage modulus and loss modulus of the gelled bioink increased significantly. In addition to the enhancement of mechanical property, the gelation also assisted the attachment of phages on the substrates. As shown in **Fig. 1d** (left), most phage microgels still stayed at the original spots after shaking in water for 24 hrs, but some detached, as indicated by loss of fluorescence. To achieve a stronger microgel attachment to the substrate, CO_2 plasma treatment was applied on the polystyrene substrate before inkjet printing to load carboxyl

groups on the surface which will participate the crosslinking reaction between phages and EDC molecules. The attachment test confirmed the stability of the phage microdots on the plasma-treated substrate (**Fig. 1d**, right).

Plasma treatment was also utilized along with bioink volume adjustment to control the diameter of phage microgels (**Fig. 1e**). The original polystyrene substrate has a water contact angle of 95.4±3.5°. By dosing the bioink volume for each dot between 3.25 nL and 13 nL, the diameter of the microdots varied from 222.5±7.8 μm to 338.8±6.0 μm. It is worth mentioning that the bioink volume can increase (minimum volume: 0.65 nL) resulting in a broader size range, if necessary. Beside controlling the bioink volume, CO_2 plasma treatment on substrates reduces the contact angle of the polystyrene substrate significantly (to 19.9±1.4°), improving the hydrophilicity of the substrate. Consequently, same volume of bioink spreads larger on the substrate, leading to a broader range of microdot diameter (between 251.5±7.7 μm and 577.65±13.95 μm). Even though adjusting bioink volume can already potentially realize the full-range control of microdot size, plasma treatment is still required because of its effects on the formation of wrinkling morphology which will be illustrated later.

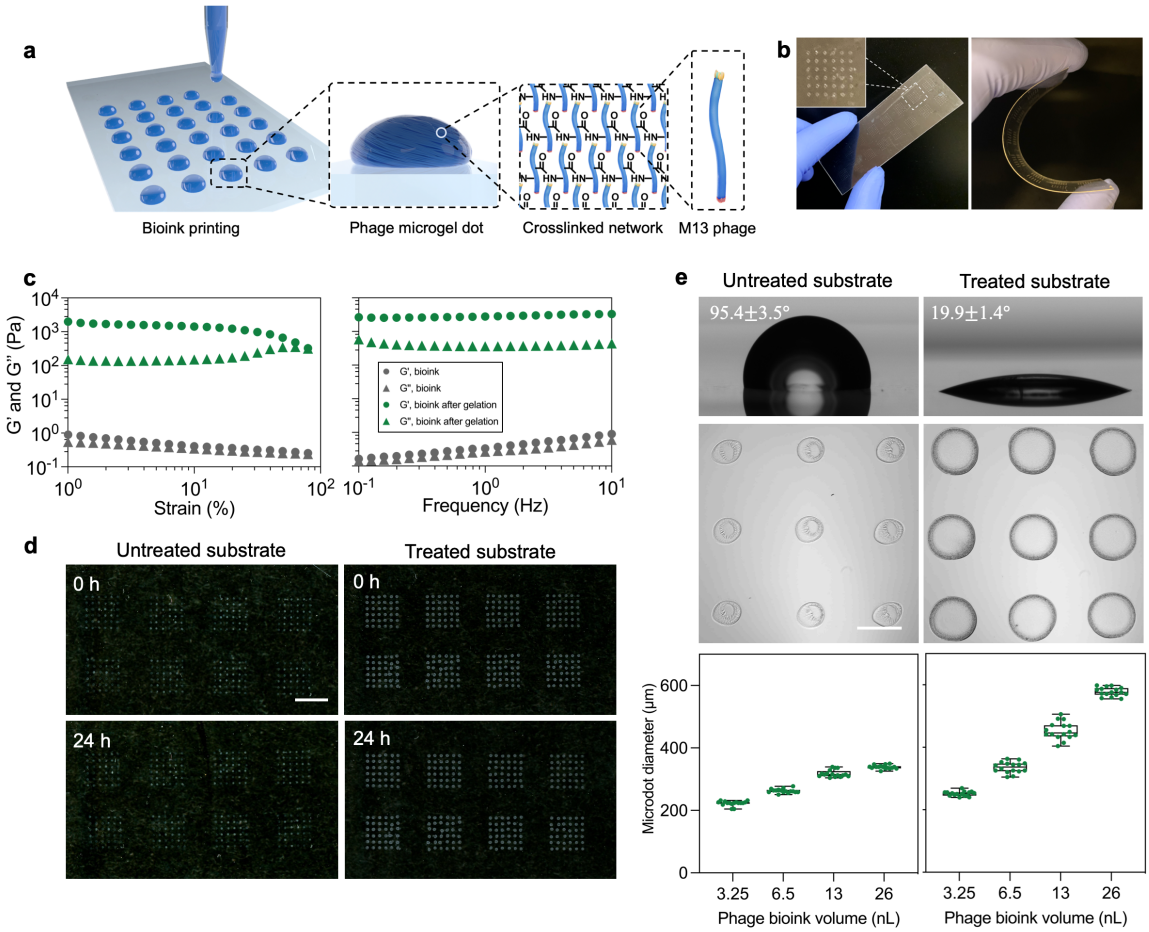

Figure 1. Inkjet printing of phage bioink on polystyrene substrate. a. Schematic of high-throughput printing of phage microgel array. **b.** Pictures of a flexible biochip with phage microdot arrays, visible as white dots. **c.** Rheological characterization of phage bioink before and after gelation. Left: Storage modulus (G') and loss modulus (G") of the bioink during amplitude sweeps with oscillation strain ranging from 1% to 100%. Right: Frequency sweep curves for the bioink with frequencies ranging from 0.1 Hz to 10 Hz with 10% strain. **d.** Photos of phage microgel arrays on the substrates before and after shaking, rehydrated in water for 24 hrs. Scale bar: 5 mm. **e.** Size control of the phage microgels. Top: Wetting behaviours of a water droplet on a untreated polystyrene substrate (left) and

a treated polystyrene substrate (right). Middle: Bright field images of phage microdots printed on corresponding substrate. Scale bar: 500 μm. Bottom: Diameter distribution of phage microgels printed on corresponding substrates at different bioink volume for each dot.

5.3.2 Tunable wrinkle structures on microdots

There has been some research on creating wrinkle structures on non-proteinous hydrogel films by thermal shrinkage.[27] The prestressed polystyrene substrate shrunk at high temperature (above 140 ℃), forcing the deposited hydrogel film to crimp and form wrinkles. We demonstrated that thermal shrinkage can be also applied to create wrinkled morphologies on phage microgels (**Supplementary Fig. 2**). However, thermal shrinkage cannot preserve delicate nanoarchitecture on proteinaceous material. As shown in the SEM images, the phages on microdots melt and the wrinkles were partially blocked. Therefore, a new biomaterial-friendly method to create wrinkles is anticipated.

Herein, we found out that prestressed polystyrene films can shrink drastically during critical point drying (CPD), as shown in **Supplementary Fig. 3**. CPD is a common heat-free dehydrating process for gels with an important capability of preserving their inner nanostructure (maximum temperature: 35 ℃). The mechanism of CPD-induced polystyrene shrinkage is still unknown but we hypothesize that it was related to the high pressure environment in CPD process. Consequently, the polystyrene films shrunk consistently and isotropically (49.9±1.7%) (**Supplementary Fig. 4**) while the surface of shrunk films still stayed flat (**Supplementary Fig. 5**). Additional, the short-term and

removable ethanol phase during CPD is proven to not affect the fiber shape of M13 phages (**Supplementary Fig. 6**).

Considering the structure-preserving ability of CPD, we applied it as a new heat-free approach to create wrinkle structures on phage microdots. As demonstrated in **Fig. 2a**, the phage microgels dehydrated and turned into phage xerogel microdots during CPD process. Meanwhile, the homogeneous shrinkage of polystyrene substrate drove these attached phage microdots to crimp internally and fold. The differences of surface morphology between air-dried and CPD-dried microdots confirmed the effectiveness of CPD shrinkage method. For the air-dried phage microdots (13 nL bioink per dot) on an untreated substrate, the surface was flat on microscale where ordered-aligned phage bundles were observed (**Fig. 2b**). On the contrary, all microdots going through CPD process exhibited consistent flowery folds (**Fig. 2c**). The central area of each dot was highly-folded while the edge area only had several wrinkles. The nanofibrous texture was still clearly visible on every wrinkle, proving the structural preservation of CPD shrinkage.

The wrinkle size of phage microdots can be controlled by adjusting the thickness of materials. As illustrated, substrate treatment led to the broader spread of bioink, resulting in a diameter increase and corresponding thickness reduction on phage microdots. We hypothesized that the thickness reduction of microdots on treated substrates would facilitate internal folding of microdots and generate different wrinkled morphologies. Meanwhile, the attachment enhancement of microdots on treated substrates can also potentially contribute to the drive force from the shrinking substrate. As shown in **Supplementary Fig. 7**, the phage aerogel microdots on treated substrate (also 13 nL bioink

per dot) were larger, indicating a decreased thickness, while still showing flat surface at microscale with ordered nanobundles.

After CPD shrinkage, the microscale morphology was distinctly different compared to the microdots on untreated substrate (**Fig. 2d**). The wrinkles at the central area were narrow and curly while the edge had wider and straight wrinkles, constituting an interesting "sunflower" structure. Furthermore, air-drying microgels before CPD process further decreased the microdot thickness and consequently generated the most homogenous wrinkled morphology (**Fig. 2e**). Quantitatively, the wrinkle width at the central area of microdots turned from 3.16±0.48 μm to 0.95±0.23 μm after switching to treated substrates (**Supplementary Fig. 8** and **9**). Air drying before CPD did not change the central wrinkle morphology significantly (1.06±0.22 μm). Instead, the effect of pre-airdry showed up on the morphology at the edge area of microdots (**Supplementary Fig. 10**), reducing the width from 3.89±1.03 μm to 1.79±0.25 μm (**Supplementary Fig. 11**). In summary, the surface morphology of phage microdots was successfully tuned through substrate treatment and pre-airdry, representing 3 different wrinkled structures where the wrinkle width varied from 5.0 μm to 0.7 μm.

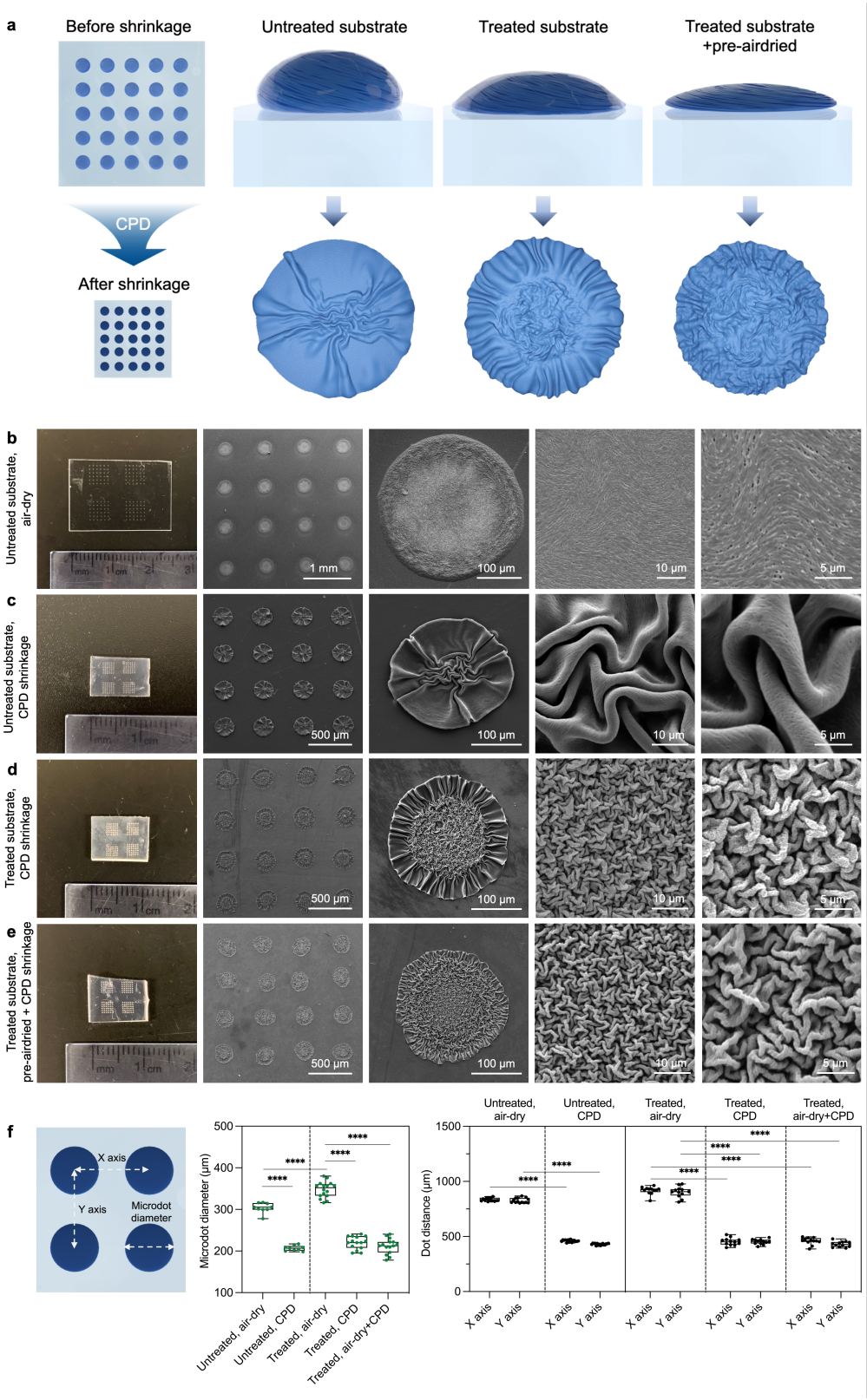
a
Before shrinkage
Untreated substrate
Treated substrate
Treated substrate +pre-airdried
CPD
After shrinkage
b
Untreated substrate, air-dry
c
Untreated substrate, CPD shrinkage
d
Treated substrate, CPD shrinkage
e
Treated substrate, pre-airdried + CPD shrinkage
1 mm
500 µm
100 µm
10 µm
5 µm
f
X axis
Y axis
Microdot diameter
Microdot diameter (µm)
Dot distance (µm)
Untreated, air-dry
Untreated, CPD
Treated, air-dry
Treated, CPD
Treated, air-dry+CPD
X axis
Y axis
****

Figure 2. Tunable hierarchical wrinkle morphologies on phage microgels with microdot array. a. Schematic of the shrinkage of polystyrene substrate driving the crimp of attached phage microdots. Plasma treatment of substrates and pre-airdried process result in different wrinkle morphology. **b-e.** Phage microdot arrays with different substrates and different treatments: **b.** Untreated substrate, air-dry, without shrinkage. **c.** Untreated substrate, CPD shrinkage. **d.** Treated substrate, air-dry, CPD shrinkage. **e.** Treated substrate, pre-airdried, CPD shrinkage. From left to right: Pictures of the phage microdot arrays on the biochip before and after shrinkage. SEM images of phage microdot array, single dot and the microstructures on the dot. **f.** Diameter and distance of microdots before and after shrinkage.

Apart from the wrinkle morphology, the microdot distance also changed corresponding to the substrate shrinkage (**Fig. 2f**). The consistent distance reduction along different directions proved again that the polystyrene shrinkage through CPD is isotropic.

Besides surface treatment on the substrate, other possible strategies to tune wrinkle morphology were investigated. We found that phage microdots made with by 3.25 nL had similar wrinkle morphology as the previous microdots made with 13 nL at the same condition (**Supplementary Fig. 12**). The wrinkle width was only slightly reduced from 3.16 ± 0.48 μm to 2.63 ± 0.41 μm, suggesting that changing bioink volume cannot manipulate the wrinkle structure effectively (**Supplementary Fig. 13**). Last but not least, reducing phage concentration successfully tuned the wrinkles to be more narrow and homogeneous. As shown in **Supplementary Fig. 14a**, reducing phage concentration by

half (5×10^{13} PFU/mL) resulted in the expansion of central wrinkled area and finer wrinkles. This phenomenon was even more significant when the concentration reduced to 2.5×10^{13} PFU/mL (**Supplementary Fig. 14b**). However, the microgels made with phages solely at low concentrations were too soft, causing the missing and deformation of some phage microdots. Therefore, reducing phage concentration is not an efficient method to tune the wrinkling morphology.

5.3.3 Three-level hierarchical structure of wrinkled phage microdots

The nanofibrous texture of the microscale wrinkles on phage microdots promoted further interest. As described above, there were orderly-aligned and closely-adjacent nanobundles on unshrunk phage microdots (**Fig. 2b** and **Supplementary Fig. 3**). Due to the structure-friendly advantage of CPD shrinkage method, the nanobundles were preserved through wrinkle formation. As shown in **Fig. 3a**, when we further magnified electron micrographs of the microscale wrinkles, ordered nanobundles were observed on these wrinkles. The gaps between nanobundles increased because of folding, resulting in a more porous nanostructure. The width of nanobundles was 102.5 ± 16.4 nm which is significantly higher than the width of individual phage nanofibers (width: 6.6 nm, length: 880 nm).

It has been reported that phages are able to self-assemble and form cholesteric structure at high concentrations (above 0.2 mg/mL)[4,12]. Therefore, the phages in our bioink (1×10^{14} PFU/mL, equivalent to around 2.7 mg/mL) were able to self-align and organize as bundles. AFM images confirmed that phages self-assembled orderly and constructed the nanobundles. Based on the observed surface morphology of phage microgels, we want to highlight their 3-level hierarchical structure (**Fig. 3b-d**), containing tunable microscale

wrinkles (width: ~0.7-5.0 μm), orderly-aligned nanobundles (width: ~100 nm) and the self-assembled phage nanofibers (width: ~7 nm). Last but not least, applying CPD shrinkage to create wrinkled morphology on microdots is not limited to microdots. Macroscale phage hydrogel films can also form homogenous microwrinkles through same approach, and the nanofibrous textures on the wrinkles were well-preserved (**Supplementary Fig. 15**). In addition, other biomaterials such as bovine serum albumin (BSA) microgels can acquire same microstructures via this method. As shown in **Supplementary Fig. 16**, microgels made with 2% BSA and EDC printed formed similar "sunflower" morphology after CPD process. It's worth mention that the smooth surface of these wrinkles proved again that the further hierarchical nanostructures of phage microdots was an unique phenomenon generated by phage nanofilaments, not resulted from the CPD process.

5.4 Conclusion

In conclusion, the CPD substrate shrinkage we discovered is a stable and generic approach to create wrinkled morphologies on microdots and films, especially for preserving complicated nanostructures on heat-sensitive materials. Benefiting from the CPD process and the unique consistent nanofiber shape of phages, the phage microdots were able to exhibit 3-level hierarchical micro/nanostructure and can potentially contribute to the applications in biosensing, drug-loading and surface-enhanced Raman spectroscopy. The immediate future directions for this work is investigating the fundamental mechanism of CPD shrinkage and developing bacteria-sensing applications of wrinkled microdots by adding functional recognition molecules.

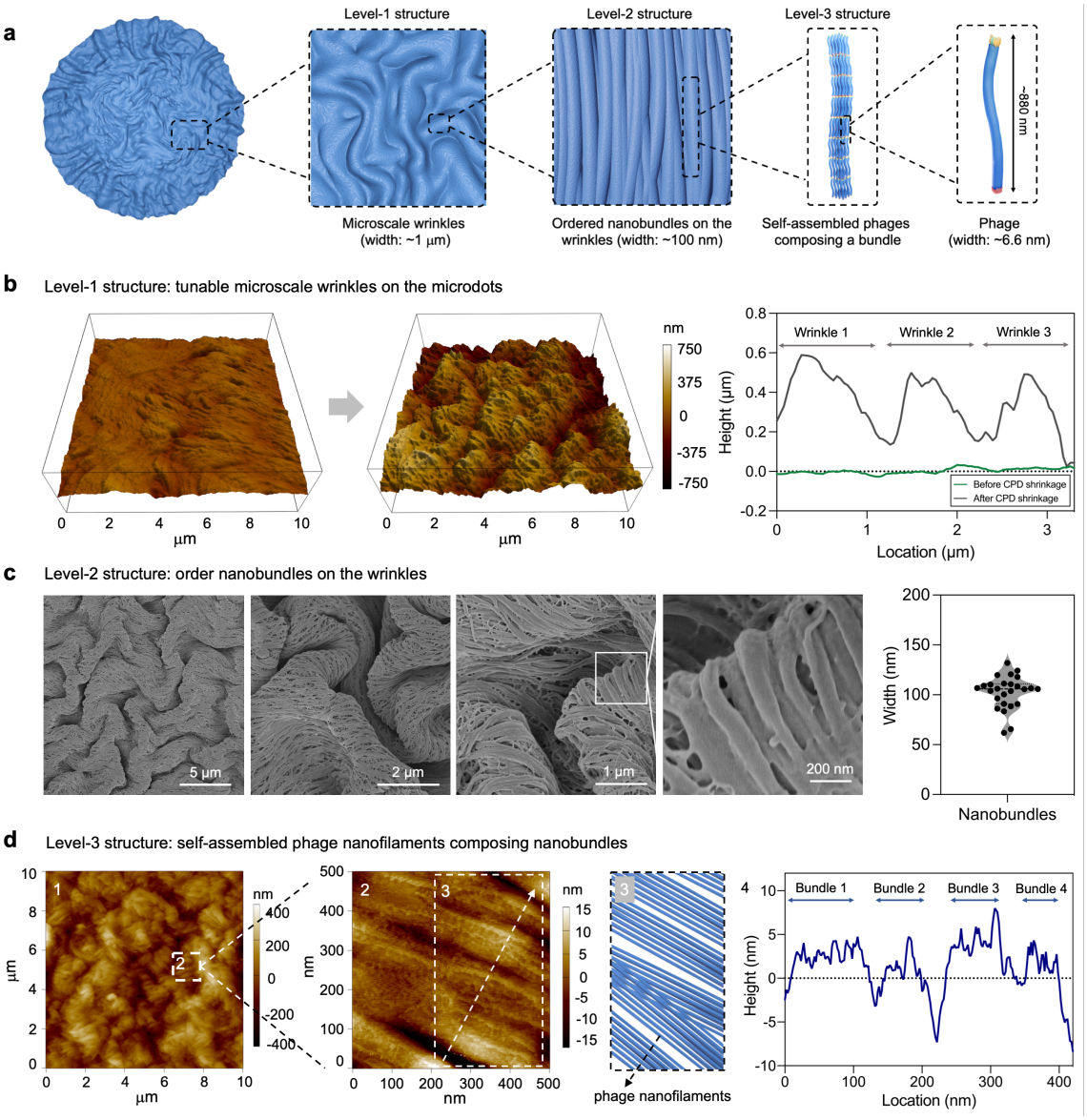

Figure 3. Three-level hierarchical structures on wrinkled phage microdots. a. Schematic of the three-level hierarchical structures on the microdots. **b.** Height change of the microdot surface after the formation of microscale wrinkles. Left: 3D AFM images of the microdot surface before and after height of the microdots. Right: Surface roughness of the microdot surface before and after CPD shrinkage. **c.** Nanobundles aligning orderly on the microwrinkles. Left: SEM images of the nanobundles on the wrinkles (coated with 3-

nm Pt). Right: Width distribution of the nanobundles. **d.** Phages aligning orderly on the nanobundles. 1, AFM images of the microwrinkles. 2, AFM images of the structure on the nanobundles. 3, Schematic of the phage alignment according to the AFM images. 4, Surface roughness of the nanobundles along the arrow direction in part 2.

5.5 Experimental methods

5.5.1 Phage propagation, purification and concentrating

To propagate M13, a single colony of *Escherichia coli* strain K12 ER2738 (New England Biolabs Ltd., E4104S) was inoculated in 4 mL of sterile LB medium and incubated overnight at 37 °C with 210 rpm shaking. Subsequently, 2.5 mL of the *E. coli* overnight culture and 10 μL of M13 phage (10^{12} PFU/mL) were added to 250 mL of autoclaved LB broth in a baffled flask and incubated at 210 rpm at 37 °C for 5 hrs. The propagated phage culture was then centrifuged at 7000 ×g for 15 minutes. After discarding the bacterial pellet, the phage-containing supernatant was stored at 4 °C. The M13 phage solution was then purified by following the procedure described by Sambrook[28]. Briefly, the phage supernatant was mixed in a 6:1 ratio with a sterile polyethylene glycol (PEG) solution (20 (w/v) % PEG/2.5 M NaCl) and stored in a fridge at 4°C overnight. The following day, the PEG-phage solution was centrifuged at 5000 ×g and 4°C for 25 mins to precipitate the phages. The pelleted phages were resuspended in 5 mL of sterilized water and gently shaken overnight on a roller at 4°C. The resuspended phage solution was again centrifuged at 5000×g for 30 mins to remove any bacterial remnants. The resulting phage solution was concentrated using 100 kDa (MWCO) and 30 kDa (Millipore Sigma, Ultra-15) centrifugal

filters to remove excess water. The final concentration was evaluated using the plaque assay method.[29]

5.5.2 Inkjet printing of phage microgel array

M13 bacteriophage (1×10^{14} PFU/mL) was mixed with EDC (0.1 M) to constitute the bioink. Optionally, the polystyrene substrates were CO_2 plasma treated for 3 mins through a plasma system (Plasma Etch, Inc.). A Scienion printer was subsequently used to print the bioink onto the substrates under 75% relative humidity, and the ink volume on spot was tuned from 3.25 nL to 13 nL. Then the samples were transferred to a sealed humid box for 12 hrs for phage gelation. Afterwards, the samples were washed by MilliQ water 3 times to remove redundant EDC.

5.5.3 Critical point dry (CPD)

To apply critical point dry, the microgels were firstly immersed in ethanol gradient (10%, 30%, 50%, 70%, 100%) for 50 mins (10 mins for each gradient) to replace contained water with ethanol. Afterwards, the microgels were dried using a Leica critical point dryer (EM CPD300).

During the CPD process, the sample chamber was firstly cooled to 14 ℃ to allow for the exchange of ethanol with liquid CO_2, and the chamber pressure climbed to the 800 psi range during this phase. Subsequently, the chamber was heated to 35 ℃ slowly (taking approximately an hour). As the temperature rose, the pressure slowly increased to a maximum of 1145 psi. As CO_2 transitions to its gaseous phase, the gas was slowly released for the remaining 2 hours until the chamber was back down to 15 psi.

5.5.4 Scanning electron microscopy

Prior to imaging, the samples were dehydrated either by air dry or CPD. Two types of Scanning Electron Microscopy (SEM) were used to image the microgels. TESCAN VEGA-II LSU SEM was used to image the polystyrene substrate and wrinkled microstructures of the samples, where 10 nm layers of gold were coated onto the samples in advance. A field emission scanning electron microscope (FEI Magellan 400) was used to image the nanofibrous textures on the surface of the microgels, where 3 nm layers of Pt were coated onto the samples in advance. The diameter and distance of phage microdots were analyzed by ImageJ based on the SEM images.

5.5.5 Quantification of width of wrinkles

To determine the width of wrinkles, SEM images of wrinkled structures were firstly adjusted for contrast. At least 60 points from 3 different images were manually selected and measured on ImageJ for each wrinkle morphology.

5.5.6 Atomic force microscopy

Atomic force microscopy images were collected using an MFP3D AFM (Asylum Research, Santa Barbara, CA) and a probe tip (Hi'Res-C14, μmash) with a spike radius below 1 nm, a typical spring constant of 5.0 N/m and resonance frequency ranging from 110-220 kHz. Igor Pro 6.0 (WaveMetrics, Inc. Lake Oswego, OR) and the Asylum software package (Asylum Research, Santa Barbara, CA) were applied to process AFM images and analyzed surface roughness.

5.5.7 Inverted fluorescence microscopy

Bright field and fluorescent micrographs of the microgels and their templates were obtained using an inverted microscope (Nikon Eclipse Ti2 inverted microscope).

Fluorescent micrographs were captured using four different optical filter sets (blue channel: ex/em = 340/435 nm; green channel: ex/em = 465/515 nm; orange channel: ex/em = 528/590 nm; red channel: ex/em = 625/670 nm). The excitation filter was positioned in front of the LED light source, and the image was captured using the emission filter attached to the camera. The intensity of the light source and the exposure time were consistent. The NIS-Elements Analysis software was applied to quantify the diameters of microgels.

5.6 References

1. Hampton, H. G., Watson, B. N. J. & Fineran, P. C. The arms race between bacteria and their phage foes. *Nature* **577**, 327–336 (2020).
2. Fortier, L. C. & Sekulovic, O. Importance of prophages to evolution and virulence of bacterial pathogens. *Virulence* **4**, 354–365 (2013).
3. Barderas, R. & Benito-Peña, E. The 2018 Nobel Prize in Chemistry: phage display of peptides and antibodies. *Anal. Bioanal. Chem.* **411**, 2475–2479 (2019).
4. Chung, W. J. *et al.* Biomimetic self-templating supramolecular structures. *Nature* **478**, 364–368 (2011).
5. Hosoya, H. *et al.* Integrated nanotechnology platform for tumor-targeted multimodal imaging and therapeutic cargo release. *Proc. Natl. Acad. Sci.* **113**, 1877–1882 (2016).
6. Bayat, F., Didar, T. F. & Hosseinidoust, Z. Emerging investigator series: bacteriophages as nano engineering tools for quality monitoring and pathogen detection in water and wastewater. *Environ. Sci. Nano* **8**, 367–389 (2021).
7. Smith, G. P. & Petrenko, V. A. Phage display. *Chem. Rev.* **97**, 391–410 (1997).
8. Lee, S. W. & Belcher, A. M. Virus-based fabrication of micro- and nanofibers using electrospinning. *Nano Lett.* **4**, 387–390 (2004).
9. Souza, G. R. *et al.* Three-dimensional tissue culture based on magnetic cell levitation. *Nat. Nanotechnol.* **5**, 291–296 (2010).
10. Peivandi, A., Tian, L., Mahabir, R. & Hosseinidoust, Z. Hierarchically Structured, Self-Healing, Fluorescent, Bioactive Hydrogels with Self-Organizing Bundles of Phage Nanofilaments. *Chem. Mater.* **31**, 5442–5449 (2019).
11. Zhi, X. *et al.* Nanofilamentous Virus-Based Dynamic Hydrogels with Tunable Internal Structures, Injectability, Self-Healing, and Sugar Responsiveness at Physiological pH. *Langmuir* **34**, 12914–12923 (2018).
12. Oh, J. W. *et al.* Biomimetic virus-based colourimetric sensors. *Nat. Commun.* **5**, 1–8 (2014).
13. Tian, L. *et al.* Self-Assembling Nanofibrous Viral Microgels as Sprayable Antimicrobials Targeting Multidrug Resistant Bacteria. *Submitt. to Nat. Commun.*

NCOMMS-22-00018A-Z, (2022).
14. De Los Santos Pereira, A., Kostina, N. Y., Bruns, M., Rodriguez-Emmenegger, C. & Barner-Kowollik, C. Phototriggered functionalization of hierarchically structured polymer brushes. *Langmuir* **31**, 5899–5907 (2015).
15. Koçer, G. *et al.* Light-Responsive Hierarchically Structured Liquid Crystal Polymer Networks for Harnessing Cell Adhesion and Migration. *Adv. Mater.* **29**, (2017).
16. Adams-McGavin, R. C. *et al.* Nanoporous and wrinkled electrodes enhance the sensitivity of glucose biosensors. *Electrochim. Acta* **242**, 1–9 (2017).
17. Chan, Y. *et al.* Solution-processed wrinkled electrodes enable the development of stretchable electrochemical biosensors. *Analyst* **144**, 172–179 (2019).
18. Khang, D.-Y., Jiang, H., Huang, Y. & Rogers, J. A. A Stretchable Form of Single-Crystal. *Science (80-.).* **311**, 208–212 (2006).
19. Chan, E. P., Smith, E. J., Hayward, R. C. & Crosby, A. J. Surface wrinkles for smart adhesion. *Adv. Mater.* **20**, 711–716 (2008).
20. Imani, S. M. *et al.* Flexible Hierarchical Wraps Repel Drug-Resistant Gram-Negative and Positive Bacteria. *ACS Nano* **14**, 454–465 (2020).
21. Sarikaya, M., Tamerler, C., Jen, A. K., Schulten, K. & Baneyx, F. Molecular biomimetics: nanotechnology through biology. *Nat. Mater.* **2**, 577–585 (2003).
22. Hou, H., Li, F., Su, Z., Yin, J. & Jiang, X. Light-reversible hierarchical patterns by dynamic photo-dimerization induced wrinkles. *J. Mater. Chem. C* **5**, 8765–8773 (2017).
23. Gabardo, C. M., Yang, J., Smith, N. J., Adams-McGavin, R. C. & Soleymani, L. Programmable Wrinkling of Self-Assembled Nanoparticle Films on Shape Memory Polymers. *ACS Nano* **10**, 8829–8836 (2016).
24. Le Goff, G. C., Blum, L. J. & Marquette, C. A. Shrinking hydrogel-DNA spots generates 3D microdots arrays. *Macromol. Biosci.* **13**, 227–233 (2013).
25. Chan, E. P. & Crosby, A. J. Fabricating microlens arrays by surface wrinkling. *Adv. Mater.* **18**, 3238–3242 (2006).
26. Kim, H. S. & Crosby, A. J. Solvent-responsive surface via wrinkling instability. *Adv. Mater.* **23**, 4188–4192 (2011).
27. De France, K. J. *et al.* 2.5D Hierarchical Structuring of Nanocomposite Hydrogel Films Containing Cellulose Nanocrystals. *ACS Appl. Mater. Interfaces* **11**, 6325–6335 (2019).
28. McCuen, R. Molecular cloning: a laboratory manual. *Cold spring Harb. Lab. Press* **186**, 182–183 (1990).
29. Kropinski, A. M., Mazzocco, A., Waddell, T. E., Lingohr, E. & Johnson, R. P. *Enumeration of bacteriophages by double agar overlay plaque assay*. *Bacteriophages: Methods and Protocols, Volume 1: Isolation, Characterization, and Interactions* **501**, (2009).

Chapter 5 Appendix: Supporting Information

5.7 Supplementary notes

5.7.1 Crosslinking reaction between M13 phages and EDC

1-Ethyl-3-(3-dimethylaminopropyl) carbodiimide (EDC) has been used as a carboxyl activating agent to induce the intermolecular coupling of carboxyl groups with amine groups[1]. M13 phages exhibit abundant carboxyl and amine groups on their protein capsid, which EDC can potentially crosslink. It was reported to use EDC to stabilize phages on the substrates[2]. However, it has not been used to construct phage hydrogels or microgels. Moreover, the special advantage of EDC was not recognized that none of the atoms from EDC (labelled in red in **Supplementary Fig. 1)** was coupled into the built phage network. EDC firstly reacted with the carboxyl groups on phage capsid and form immediate product with active ester which later reacted with the amine groups. Consequently, the phages were connected by amide bonds and formed phage hydrogels/microgels. On another word, EDC took oxygen atoms from carboxyl groups on phages and formed water-soluble isourea by-product which can be easily washed out. Eventually, a phage-exclusive network is achieved using simple M13+EDC bioink.

5.8 Supplementary figures

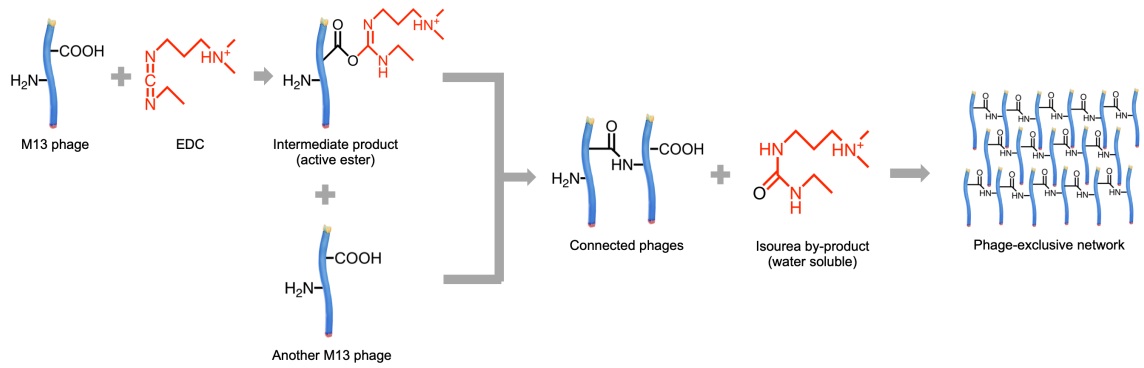

Supplementary Figure 1. The crosslinking reactions between M13 phages and EDC.

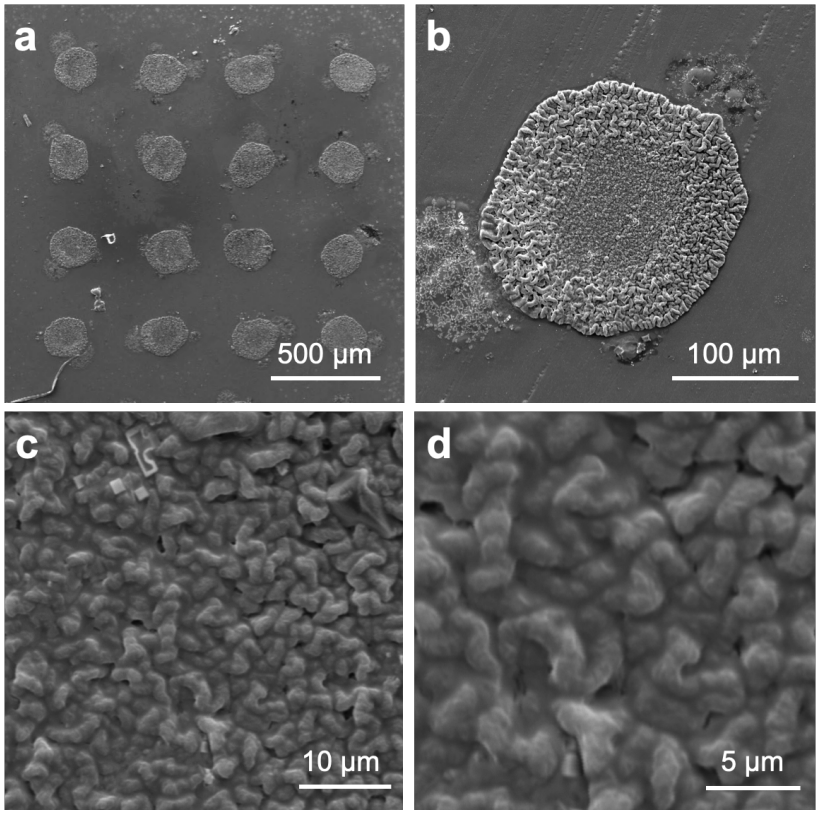

Supplementary Figure 2. Thermal-shrinking method to create wrinkles on phage microdots. SEM images of **a.** the array of shrunk phage microdots, **b.** a shrunk phage microdot and **c-d.** the wrinkle structure on the microdot surface.

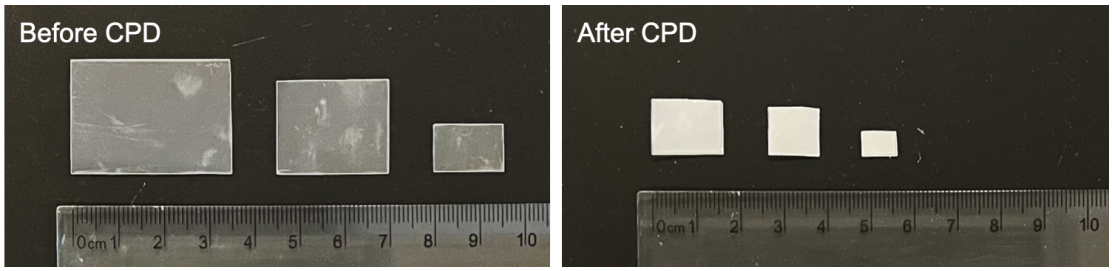

Supplementary Figure 3. CPD-shrinkage phenomenon of prestressed polystyrene sheet. Photos of 3 sizes of polystyrene sheet before and after CPD process.

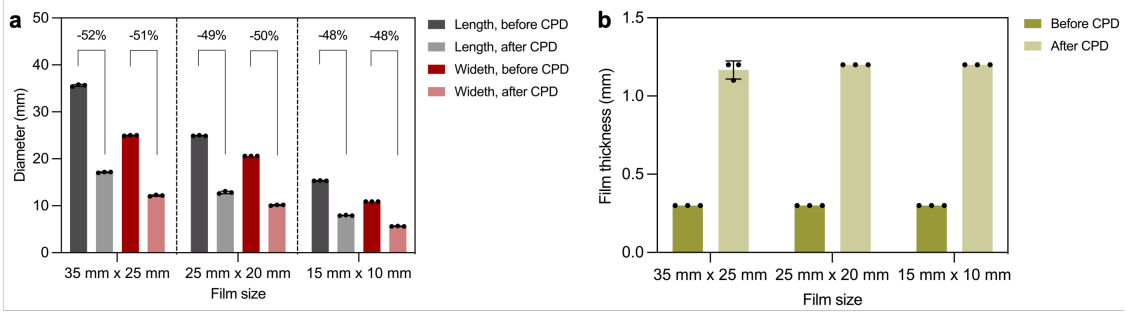

Supplementary Figure 4. Drastic size reduction of prestressed polystyrene sheets after CPD-shrinkage. a, Length and width of the 3 sizes of polystyrene sheet before and after CPD process. **b,** Film thickness of the 3 sizes of polystyrene sheet.

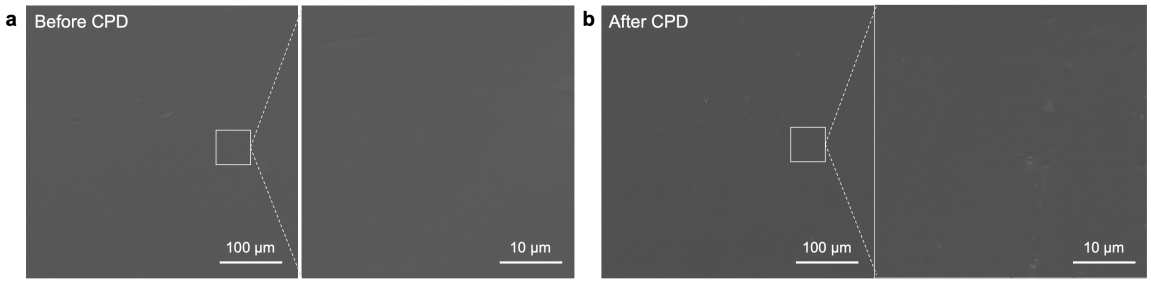

Supplementary Figure 5. Polystyrene sheets maintaining flat surface after CPD-shrinkage. SEM images of the surface of polystyrene sheets **a,** before and **b,** after CPD process.

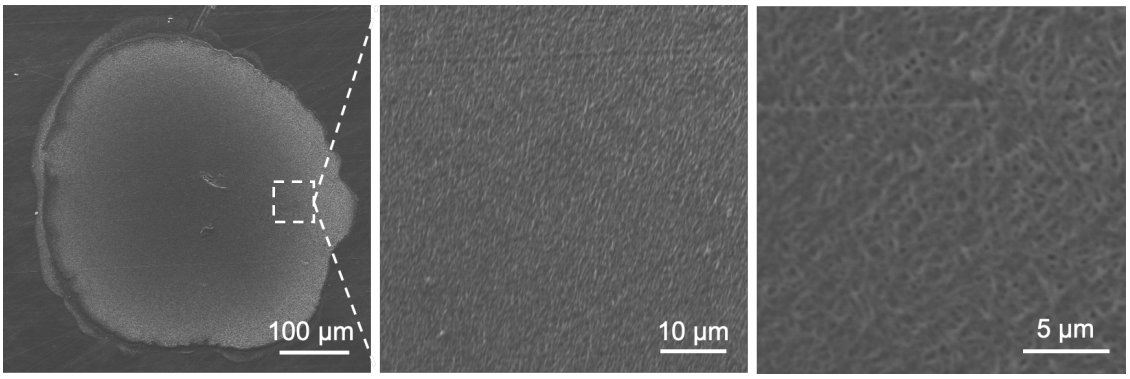

Supplementary Figure 6. Ethanol showed no observable effect on the surface morphology of phage microgels. SEM images of a phage microgel after immersing in ethanol for 5 hours.

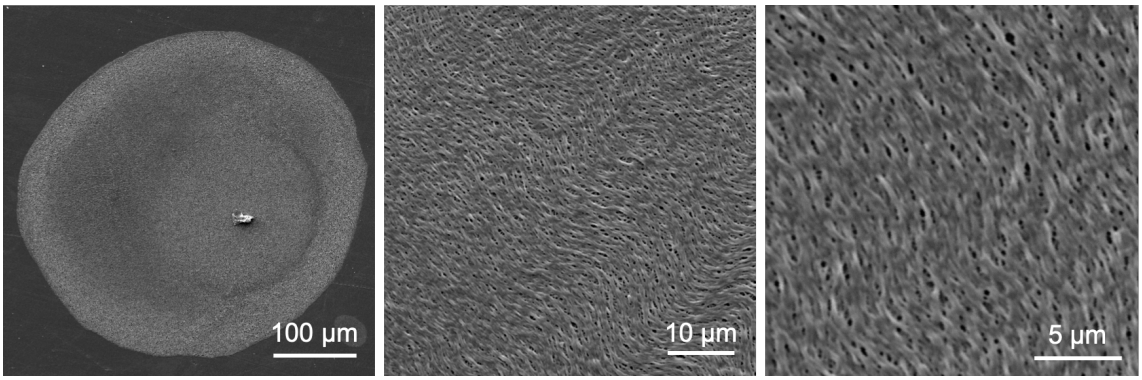

Supplementary Figure 7. SEM images of an air-dried phage microgel on plasma-treated substrate and the nanofibrous texture on the microgel surface.

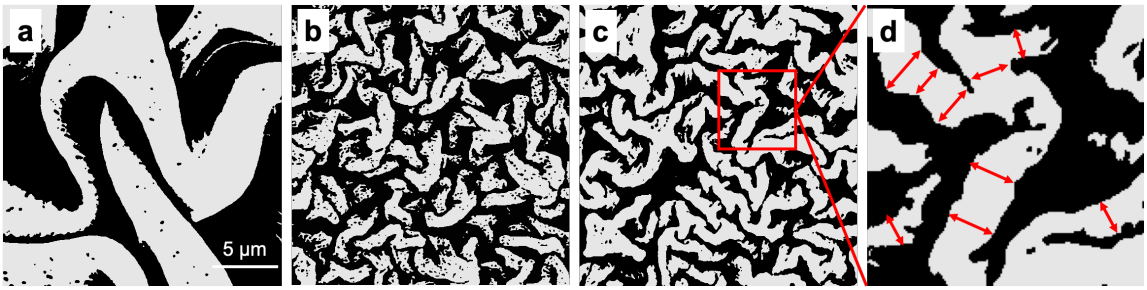

Supplementary Figure 8. Quantitative analysis of wrinkle width. a-c, Contrast-enhanced SEM images of wrinkled microstructures corresponding to the wrinkle morphologies in **Fig. 2c-e**, respectively. **d,** Zoom-in image of panel **c**. Inset arrows indicate the width of wrinkles.

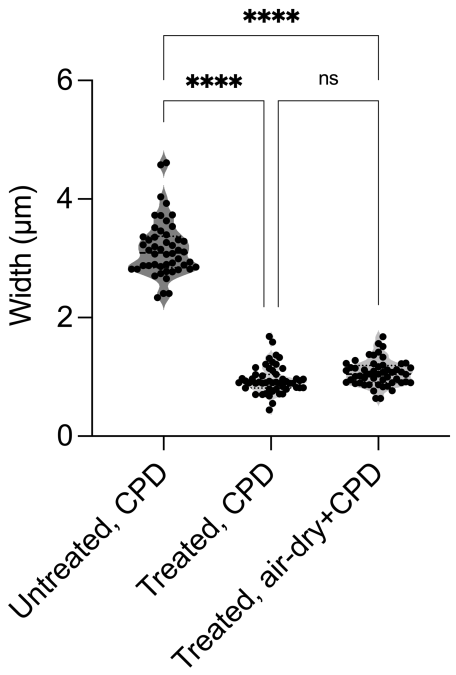

Supplementary Figure 9. Width distribution of the wrinkles at the central area of phage microdots.

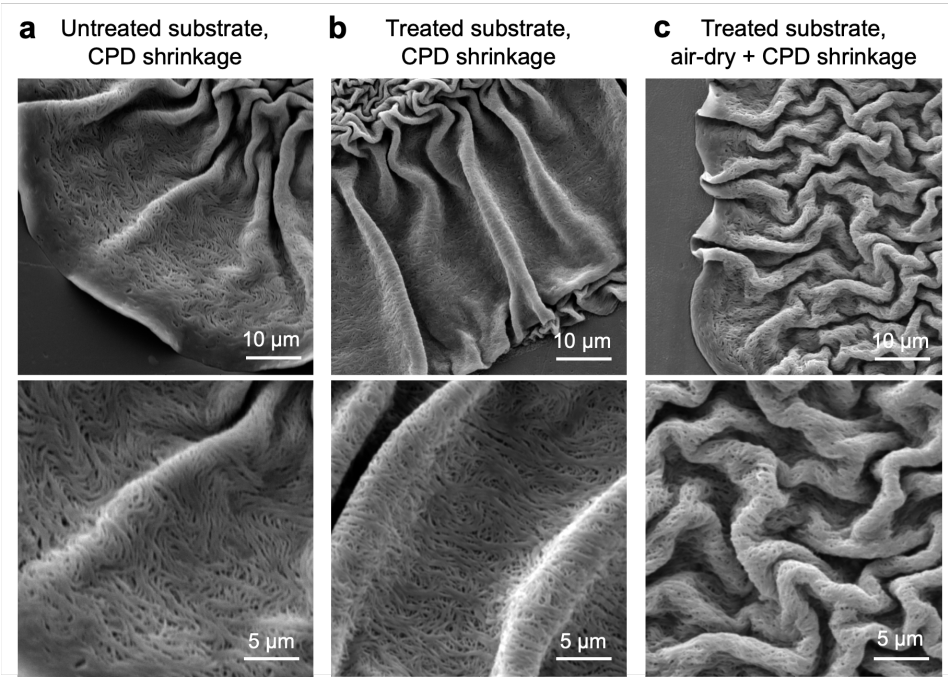

Supplementary Figure 10. Morphology difference at the edge areas of the wrinkled microgels obtained under different conditions. a-c, SEM images of the edge areas of the wrinkled microgels.

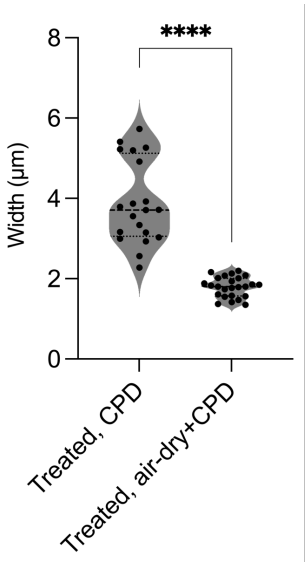

Supplementary Figure 11. Width distribution of wrinkles at the edge areas. Microdots on untreated substrate is not included here because of the unclear borders of the wrinkles at the edge area.

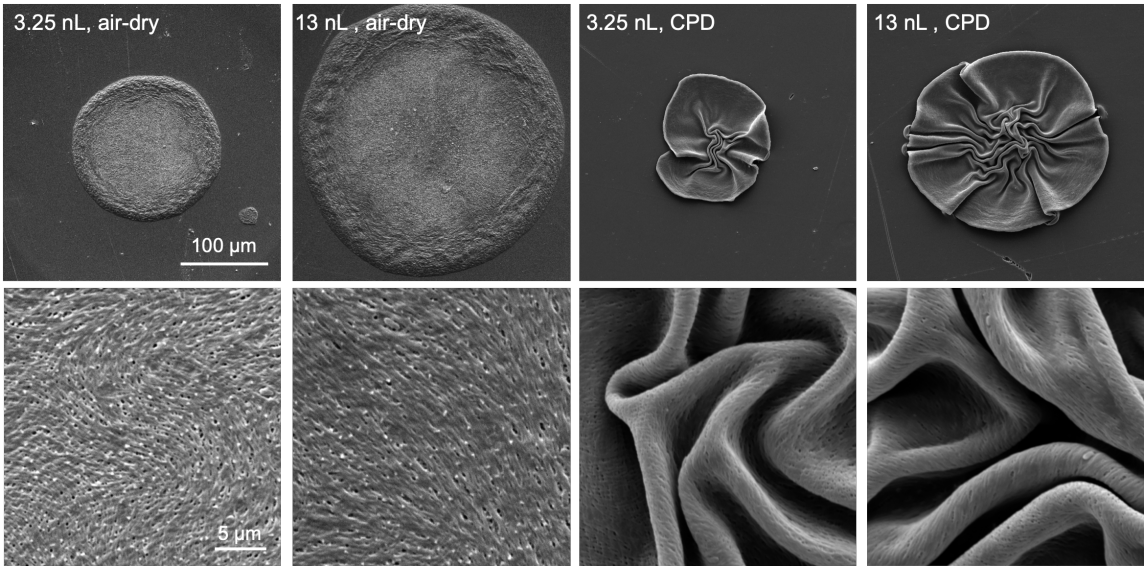

Supplementary Figure 12. Effect of bioink volume on wrinkled morphology. SEM images of phage microgels (3.25 nL and 13 nL of bioink respectively) on untreated substrates with and without CPD shrinkage.

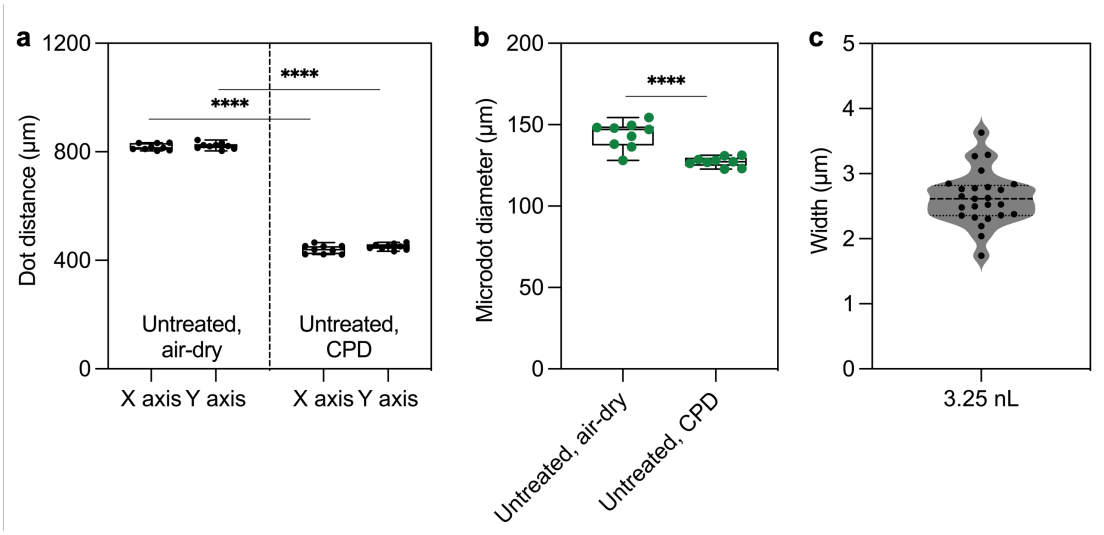

Supplementary Figure 13. Quantitative data of wrinkled microdots while using less bioink volume for each dot (3.25 nL instead of 13 nL). a. Microdot distance of phage

microgels (3.25 nL) with and without CPD shrinkage. **b.** Microdot diameter of phage microgels (3.25 nL) with and without CPD shrinkage. **c.** Wrinkle width at the central area of the phage microgels (3.25 nL).

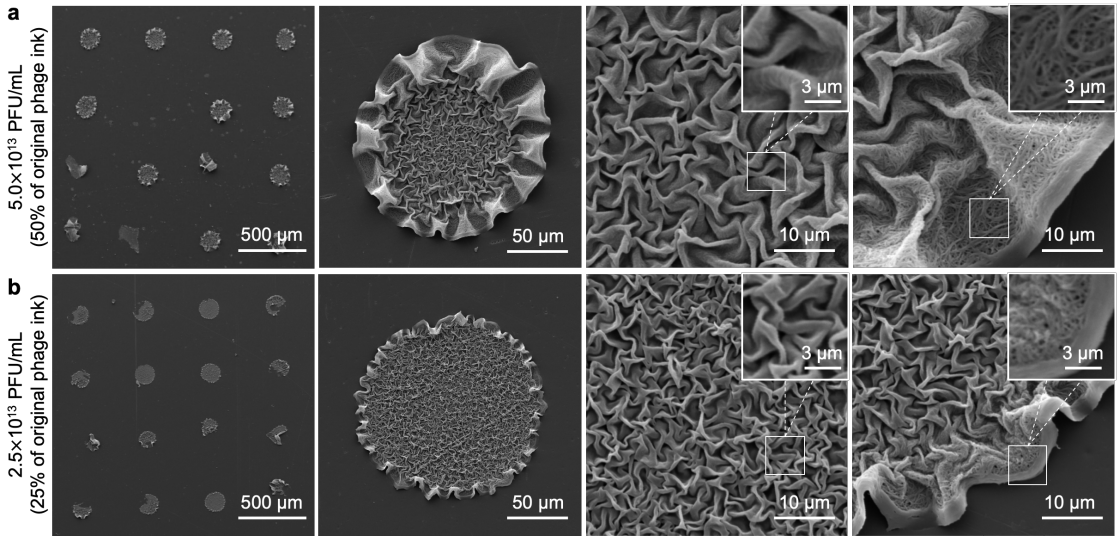

Supplementary Figure 14. Effect of the concentration of phage ink on the wrinkle morphology. From left to right: SEM images of the phage microdot array, one single dot, the microstructure in the center of the dot and the microstructure on the edge of the dot. Inserts are the partial enlarged pictures of corresponding images. The microdots were printed on untreated substrates and the phage concentration used were **a.** 5.0×10^{13} PFU/mL and **b.** 2.5×10^{13} PFU/mL respectively.

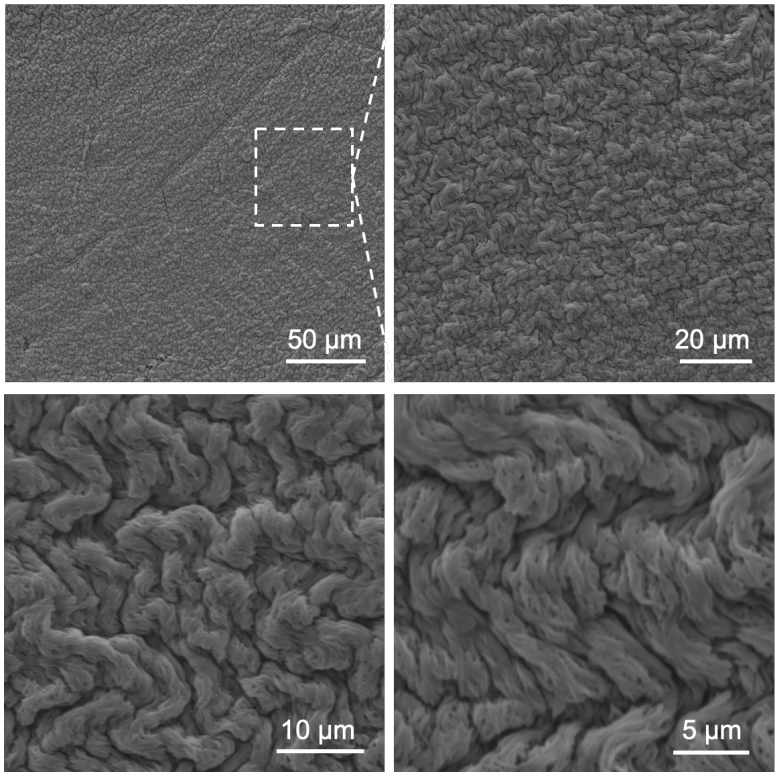

Supplementary Figure 15. Phage aerogel films exhibiting wrinkle microstructure via CPD shrinkage. SEM images of the hierarchical surface on phage aerogel films on treated polystyrene substrates after CPD shrinkage.

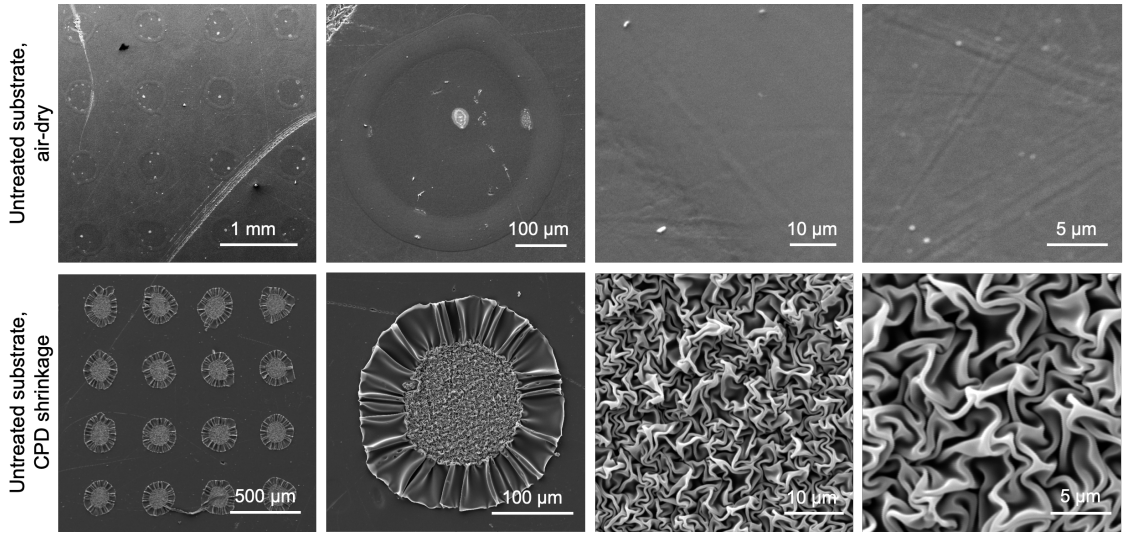

Supplementary Figure 16. BSA microdots exhibiting wrinkle microstructure via CPD shrinkage. From left to right: SEM images of phage microdot array, single dot and the microstructures on the dot without and with CPD shrinkage.

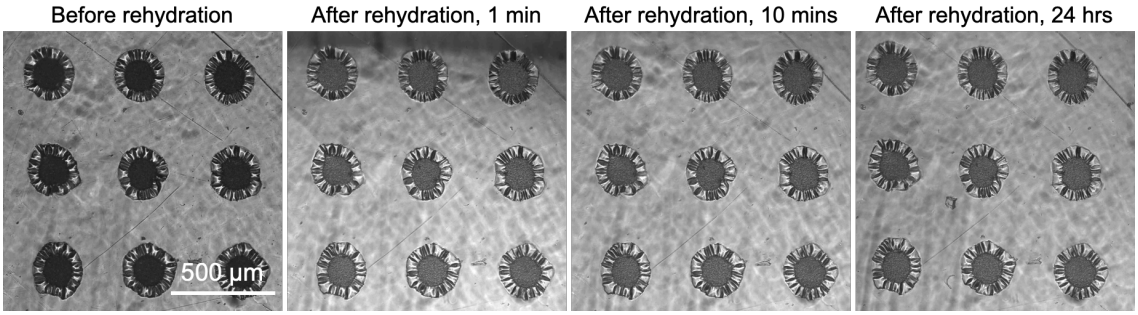

Supplementary Figure 17. Wrinkled microgels maintaining same microstructure after shaking in water for 24 hours. Bright field microscopy images of the wrinkled microgels before rehydration, in water for 1 min, 10 mins and 24 hrs respectively.

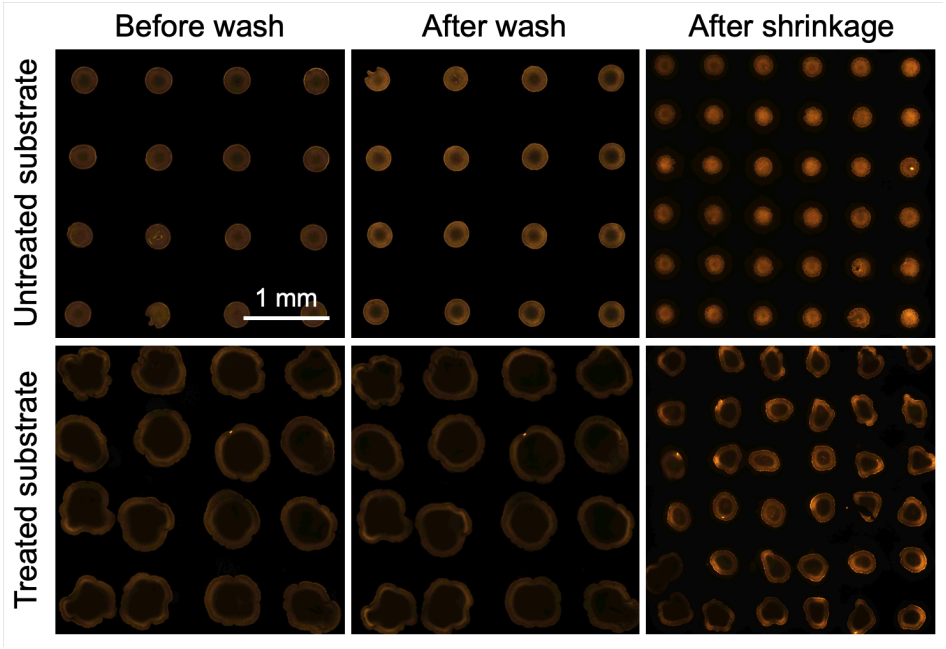

Supplementary Figure 18. Stability of DNAzyme in phage microdots through shrinkage process. Fluorescent images of phage+DNAzyme microdots before and after washing and shrinkage.

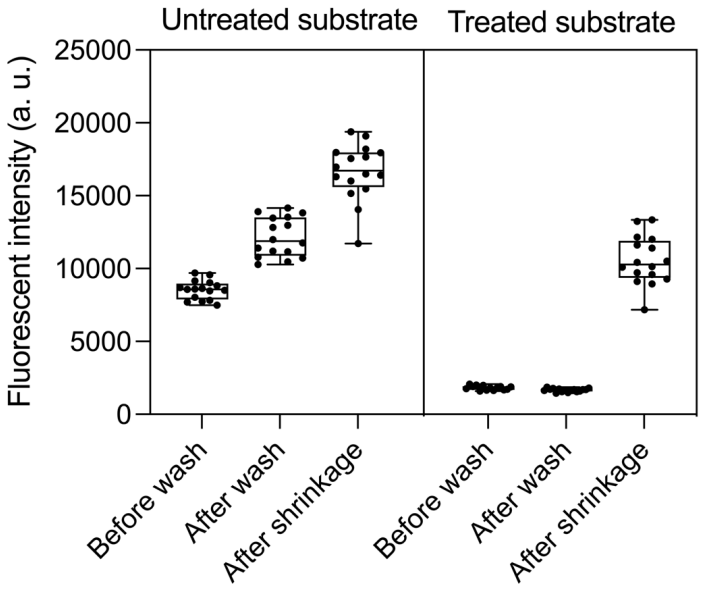

Supplementary Figure 19. Quantified fluorescent intensity of phage+DNAzyme microdots. Fluorescent images of phage+DNAzyme microdots before and after washing and shrinkage.

5.9 References

1. Grabarek, Z. & Gergely, J. Zero-length crosslinking procedure with the use of active esters. *Anal. Biochem.* **185**, 131–135 (1990).
2. Courchesne, N. M. D. *et al.* Assembly of a bacteriophage-based template for the organization of materials into nanoporous networks. *Adv. Mater.* **26**, 3398–3404 (2014).

Chapter 6 Conclusions and Future Direction

6.1 Conclusions

In this thesis, two biomaterial-friendly methods were proposed to fabricate three series of bioactive microstructured hydrogels. It highlighted the scientific importance of microstructured hydrogels on biomedical applications, such as antifouling surfaces, antimicrobial food spray and bacteria-sensing biointerfaces.

We, for the first time, designed microstructures and further hierarchically nano-on-micro morphology on protein hydrogels. By changing interfacial properties, 2-dimensional (flat) surface to 2.5-dimensional (shallow microbumps) surface and finally 3-dimensional (spherical microbumps) surface was achieved on protein hydrogels utilizing honeycomb templates. Nanogels made with same protein were further encapsulated in the microbumps and resulted in an interesting hierarchical nano-on-micro structure. These hierarchical morphologies significantly inhibited long term attachment of multidrug-resistant *Staphylococcus aureus* up to 100× over a flat hydrogel. Comparing to the few reports on microstructured (not hierarchically structured) synthetic polymer hydrogels, we were able to develop a protein hydrogel efficiently that exhibits bacteria repellency surpassing anything reported in the literature and avoids expensive and complex photolithographic or molding methods.

We further adapted the molding method to prepare free-standing phage microgels which is the first virus-exclusive microparticle platform. The crosslinked phages in each phage-exclusive microgel self-organized to exhibit a highly-aligned nanofibrous texture and emit tunable fluorescence that can expand potential applications beyond biocontrol to

theranostics and biosensing. The phage microgels exhibited strong loading capacity and effectively reduced multidrug resistant *Escherichia coli* O157:H7 on food products by 6 logs reduction in 9 hours and rendering food contaminant free.

Last but not least, we demonstrated another strategy, inkjet printing, to fabricate ordered arrays of phage microgels. A nanostructure-friendly substrate shrinkage was proposed to create diverse wrinkle patterns on phage microdots and preserve their sophisticated nanostructures, resulting in an unique single-material three-level hierarchical micro/nano-structure. This structure can potentially contribute to the applications in biosensing, drug-loading and surface-enhanced Raman spectroscopy. Specifically, we are exploring the biosensing applications for these novel structures.

6.2 Contributions to the science and technology

The novelty of **Chapter 3** is twofold: In addition to developing an antifouling protein hydrogel, we also developed of a method for patterning of hydrogels with ordered shape-controllable microstructures as well as nano-on-micro hierarchical structures that is compatible with protein hydrogels. Our method can also be extended to any hydrogel with heat-sensitive molecules, such as antibiotics and drugs, because most current method that could be used for hierarchically structuring of hydrogels are inherently incompatible with heat-sensitive molecules. **Table 1 and 2** highlight the novel contribution of chapter 3 compared to prior art on hierarchical and antifouling hydrogels.

Table 1. Contribution of chapter 3 to hierarchical microstructure formation

Method	Honeycomb mold		Photolithography and photopolymerization		Shrinking
	Our work	Others	Direct	indirect (with mold)	
Material	Protein (applicable to heat-sensitive molecules)	P(NIPAAm)[1, 2] or PMMA-PEG[3]	PEG,[4,5] or Polyphosphazenes [6]	PEG[7–10], calcium alginate and chitosan[11]	POEGMA[1 2]
Same template for multiple shapes	Yes	No	N/A	No	No
Hierarchical structure	Yes, isotropic	No	No	No	Yes but anisotropic
Surface roughness control	Yes	No	No	No	No
Compatibility with proteins	Yes	N/A	No (photo-reactive cross-linker is required)	N/A	No (elevated temperature involved)
Microstructure type	Spherical, semi-spherical and shallow microbump array	Spherical microbump array	Cylinders,[4,5,13,14] cantilever,[4] stars[5,13] and shallow dots[14]	Lines,[7] squares,[7,8] cylinders,[9] nanoneedles[10] and shallow dots[7,9,11]	Disordered wrinkles
Microdot count/cm^2	More than 100,000	More than 100,000	Normally less than 100	Normally dozens to hundreds	N/A
Required large/complex equipment	No (Require small pump, plasma chamber for some shapes)	No	Complex photolithographic or photopolymerization system		No

Table 2. Contribution of chapter 3 to microstructured antifouling hydrogels

	Our work	X. Yao et al. (*Adv. Funct . Mater.*, **2020**)[15]	H. Park et al. (*ACS Macro Lett.*, **2019**)[10]	D. Keskin et al. (*BioMacromolecules*, **2019**)[16]
Material	**Proteins (can be extended to any heat sensitive molecule)**	PVA hydrogels	PEG hydrogel coating	Poly (NIPAM) microgels
Method	**Honeycomb templates**	Microfluidic-Emulsion-Templating Method	Photolithographic silicon template and grafting	Emulsion synthesis and spraying deposition
Microstructure type & size	**Nano-on-micro bumps, 300 nm-30 µm**	Micropores, 133 µm	Nanoneedles, 200 nm in bottom diameter, 300 nm in height	Microgels coating, 100 nm - 800 nm
Hierarchical microstructure	**Yes**	No	No	No
Repellency & magnitude	***S. aureus* (Multidrug resistant, strong biofilm former),100× decrease**	*E. coli*, 53.8% decrease	*E. coli* and *B. subtilis,* No clear number stated	*S. aureus*, 99.7% decrease
Long term antifouling	**Yes, 48 hrs**	No, 4 hrs	Yes, 18 hrs	No, 4 hrs

In **Chapter 4**, the novelty is threefold: The bacteriophage microgels were manufactured through a high-throughput template method optimized in-house, which is particularly well-suited to soft biomaterials, because it is free of organic solvents and heat (**Table 3**). Meanwhile, bacteriophages are not only the natural antimicrobial agents in our products, but also the sole structural component. This is the first report of a pure viral and bioactive microgel. The only other reported nanofibrous microgels in the literature was made of amyloid fibers and did not achieve an ordered alignment like our microgels (**Table 4**). Our

microgels were applied as a superintegrated antimicrobial patch or microgel spray for cleaning up heavily contaminated food products.

Table 3. Contribution of chapter 4 to microgel generation method

Preparation method	Micromolding		Microfluidics	Emulsion /polymerization	Heat treatment
	Our work	**Others**			
Building material	**Phages (compatible to any environment-sensitive biomaterial)**	PEG derivatives[17,18]	PEG derivatives[19], agarose[20], alginate[20], protein[21–23]	PNIPAM derivatives[24], PEG derivatives[25]	Protein[26–28]
Compatibility with bioactive molecules	**Yes**	Yes	Yes	No	No (acid and high heat involved)
Preparation efficiency	**High-throughput (Over 35,000 microgels/cm^2)**	<10,000 in total	High-throughput	High-throughput	High-throughput
Organic solvent-free	**Yes**	Yes	No	No	Yes
Gelation time	**No requirement**	No requirement	Require fast gelation	Require fast gelation	N/A
Microgel size	**25 µm (Honeycomb pores can adjust sizes[29])**	Above 100 µm	1 µm to submillimeter	Submicrometer to 100 µm	100 nm to 1 µm
Shape flexibility	**Yes (Honeycomb pores can adjust shapes[30–32])**	Yes	No (Spheres and rods)	No (except combining other technics[25])	No
Required large/complex equipment	**No**	The templates are normally made by lithographic system	Yes	Yes	No

Table 4. Contribution of chapter 4 for nanostructured microgels

		Our work	U. Shimanovich et al, *ACS Nano*, 2019[21]	X. Zhou et al, *ACS Nano*, 2015[23]	B. Schulte et al, *Macromolecules*, 2014[33]	A. Wang et al, *Adv. Funct. Mater.*, 2012[34]
Microgel format		**Self-aligned phage-composed microgels**	Protein nanofiber-composed microgels	Protein nanofiber-composed microgels	Polymeric microgels	Hydrogel absorbed on porous microparticles
Material		**Phage M13**	Amyloid fibrils	Amyloid fibrils	Polyglycidol-based polymers	Gelatin on $CaCO_3$ microparticles
Nanostructure	**Ordered nanostructure**	**Yes**	No	No	No	No
	Type	**Nanofibrous**	Nanofibrous	Nanofibrous	Nanoporous	Nanoporous
	Size	**7 nm**	Not provided	Not provided	4-5 nm	Not provided
Intrinsic property (not from encapsulated molecules)	**Optical property**	**Multichannel tunable fluorescence**	No	No	No	No
	Other function	**Bioactivity**	No	No	pH response	No

In **Chapter 5**, the novelty is twofold: In addition to designing novel three-level hierarchical structures on viral materials, the CPD-shrinkage method to induce wrinkle morphologies is particularly well-suited to biomaterials with sophisticated functional structures (**Table 5**).

Table 5. Contribution of chapter 5 to wrinkled microdots

	Our work	G. Goff *et al*[35]	H. Hao *et al*[36]
Material	**Bacteriophages**	PDMAA derivatives	Anthracene-containing polymer (PAN)
Shrinkage method	**Critical point dry**	Heat shrinkage (> 160 ℃)	UV + heat (70 ℃)
Controllability of wrinkles	**Yes**	No	No
Heat-free	**Yes**	No	No
Hierarchical structure on the wrinkles	**Yes (Nanofibrous texture)**	No	No
Application	**Bacterial detection**	Detect biotinylated (B)	N/A

6.3 Challenges

Even though the methods proposed in the thesis are already well-developed. There are still challenges remaining in terms of commercialization:

(1) In chapter 4, the preparation method we proposed has no detrimental effect on the bioactivity of phage microgels. However, as we mentioned, it is hard to avoid the intramolecular crosslinking on the absorption sites of phages which would affect their infectivity. This problem might be solved by finding a reversible crosslinker that can also induce the gelation of phages.

(2) In chapter 4, the preparation method replies on peeling the top layer of honeycomb films to isolate microgels. This method works very well in small scale (when template area less than 10 cm^3 which can already produce over 350, 000 of microgels). But it is hard to predict the peeling completeness if the template is extended to larger scale.

(3) In chapter 5, the pressure-induced shrinkage method preserved the functional structures of phage materials. However, the desiccation after wrinkle formation caused the de-activity of phages. This can potentially be solved by using desiccation-resistant phages, encapsulating lytic phage in protective coatings, or modifying the method to create wrinkles while the phage microdots are still hydrated.

6.4 Recommendations for future work

(1) In the work of this thesis, we utilized two small-molecule crosslinkers (glutaraldehyde and EDC) to induce the gelation of proteins and phages, where different crosslinking reactions brought different optical properties. It is recommended to test more crosslinkers. For instance, long-chain crosslinkers might have lower requirement of the phage concentration for gelation. Reversible crosslinkers can induce the controllable degradation of phage microgels.

(2) The microgels and microdots we fabricated are composed of M13 filamentous phages. It is worth to investigate whether bacteriophages with other shapes (such as tailed and icosahedral) can form the gel and exhibit different nanostructures.

(3) The preparation method of phage microgels we proposed is potentially feasible for all materials, especially biological materials. We recommend to extend the method to produce other bioactive microparticles, such as protein microgels and biofilm beads.

(4) *In vivo* test of phage microgels: we have shown that phage microgels can kill antibiotic-resistant bacteria. Further animal study to treat bacterial infections could promote the commercialization of phage microgels to the next step.

(5) We have demonstrated that the pressure-induced substrate shrinkage can create wrinkle structures on different scale (microdots and macroscale films) and different materials (phages and BSA). It is encouraged to apply this method to construct microstructures on other materials, such as graphene oxide films.

(6) The pressure-induced substrate shrinkage is now realized by the liquefied carbon dioxide critical point dry. A high-pressure chamber could help analyze the shrinkage process better. Foundational calculations of shrinkage can further help predict and control the shrinkage process.

6.5 References

1. Kyoung, J. & Basavaraja, K. C. Preparation and characterization of smart hydrogel nanocomposites sensitive to oxidation – reduction. *Polym. Bull.* **70**, 207–220 (2013).
2. Kim, J. K., Jung, K. H., Jang, J. H. & Huh, D. S. Hydrophobic interaction-mediated reversible adsorption − desorption of nanoparticles in the honeycomb-patterned thermoresponsive. *Polym. Bull.* **71**, 1375–1388 (2014).
3. Online, V. A., Jang, J. H., Orba, M., Wang, S. & Huh, D. S. Adsorption–desorption oscillations of nanoparticles on a honeycomb-patterned pH-responsive hydrogel surface in a closed reaction system. *Phys. Chem. Chem. Phys.* **16**, 25296–25305 (2014).
4. Lv, C. *et al.* Humidity-responsive actuation of programmable hydrogel microstructures based on 3D printing. *Sensors Actuators, B Chem.* **259**, 736–744 (2018).
5. Levalley, P. J. *et al.* Fabrication of Functional Biomaterial Microstructures by in Situ Photopolymerization and Photodegradation. *ACS Biomater. Sci. Eng.* **4**, 3078–3087 (2018).
6. Allcock, H. R., Phelps, M. V. B., Barrett, E. W., Pishko, M. V. & Koh, W. G. Ultraviolet photolithographic development of polyphosphazene hydrogel microstructures for potential use in microarray biosensors. *Chem. Mater.* **18**, 609–613 (2006).
7. Koh, W. G. & Pishko, M. Photoreaction Injection Molding of Biomaterial Microstructures. *Langmuir* **19**, 10310–10316 (2003).
8. Koh, W. G., Itle, L. J. & Pishko, M. V. Molding of Hydrogel Microstructures to Create Multiphenotype Cell Microarrays. *Anal. Chem.* **75**, 5783–5789 (2003).
9. Kim, D. N., Lee, W. & Koh, W. G. Micropatterning of proteins on the surface of three-dimensional poly(ethylene glycol) hydrogel microstructures. *Anal. Chim. Acta* **609**, 59–65 (2008).

10. Park, H. H. *et al.* Lipid-Hydrogel-Nanostructure Hybrids as Robust Biofilm-Resistant Polymeric Materials. *ACS Macro Lett.* **8**, 64–69 (2019).
11. Franzesi, G. T., Ni, B., Ling, Y. & Khademhosseini, A. A controlled-release strategy for the generation of cross-linked hydrogel microstructures. *J. Am. Chem. Soc.* **128**, 15064–15065 (2006).
12. De France, K. J. *et al.* 2.5D Hierarchical Structuring of Nanocomposite Hydrogel Films Containing Cellulose Nanocrystals. *ACS Appl. Mater. Interfaces* **11**, 6325–6335 (2019).
13. Ding, Z., Salim, A. & Ziaie, B. Squeeze-film hydrogel deposition and dry micropatterning. *Anal. Chem.* **82**, 3377–3382 (2010).
14. Liu, J., Gao, D., Li, H. F. & Lin, J. M. Controlled photopolymerization of hydrogel microstructures inside microchannels for bioassays. *Lab Chip* **9**, 1301–1305 (2009).
15. Yao, X. *et al.* Omniphobic ZIF-8@Hydrogel Membrane by Microfluidic-Emulsion-Templating Method for Wound Healing. *Adv. Funct. Mater.* **30**, 1–9 (2020).
16. Keskin, D., Mergel, O., Van Der Mei, H. C., Busscher, H. J. & Van Rijn, P. Inhibiting Bacterial Adhesion by Mechanically Modulated Microgel Coatings. *Biomacromolecules* **20**, 243–253 (2019).
17. Li, Y. *et al.* Rapid Assembly of Heterogeneous 3D Cell Microenvironments in a Microgel Array. *Adv. Mater.* **28**, 3543–3548 (2016).
18. Yeh, J. *et al.* Micromolding of shape-controlled, harvestable cell-laden hydrogels. *Biomaterials* **27**, 5391–5398 (2006).
19. Headen, D. M., Aubry, G., Lu, H. & García, A. J. Microfluidic-based generation of size-controlled, biofunctionalized synthetic polymer microgels for cell encapsulation. *Adv. Mater.* **26**, 3003–3008 (2014).
20. Eydelnant, I. A., Betty Li, B. & Wheeler, A. R. Microgels on-demand. *Nat. Commun.* **5**, 1–9 (2014).
21. Roode, L. W. Y., Shimanovich, U., Wu, S., Perrett, S. & Knowles, T. P. J. Protein Microgels from Amyloid Fibril Networks. *ACS Nano* **1174**, 223–263 (2019).
22. Shimanovich, U., Song, Y., Brujic, J., Shum, H. C. & Knowles, T. P. J. Multiphase protein microgels. *Macromol. Biosci.* **15**, 501–508 (2015).
23. Zhou, X. M. *et al.* Enzymatically Active Microgels from Self-Assembling Protein Nanofibrils for Microflow Chemistry. *ACS Nano* **9**, 5772–5781 (2015).
24. Brugger, B. & Richtering, W. Magnetic, thermosensitive microgels as stimuli-responsive emulsifiers allowing for remote control of separability and stability of oil in water-emulsions. *Adv. Mater.* **19**, 2973–2978 (2007).
25. An, H. Z., Helgeson, M. E. & Doyle, P. S. Nanoemulsion composite microgels for orthogonal encapsulation and release. *Adv. Mater.* **24**, 3838–3844 (2012).
26. Schmitt, C. *et al.* Internal structure and colloidal behaviour of covalent whey protein microgels obtained by heat treatment. *Soft Matter* **6**, 4876–4884 (2010).
27. Nicolai, T. Formation and functionality of self-assembled whey protein microgels. *Colloids Surfaces B Biointerfaces* **137**, 32–38 (2016).
28. Phan-Xuan, T. *et al.* On the crucial importance of the ph for the formation and self-stabilization of protein microgels and strands. *Langmuir* **27**, 15092–15101 (2011).
29. Takehiro Nishikawa *et al.* Fabrication of Honeycomb Film of an Amphiphilic

Copolymer at the Air−Water Interface. *Langmuir* **18**, 5734–5740 (2002).
30. Daly, R., Sader, J. E. & Boland, J. J. Taming Self-Organization Dynamics to Dramatically Control Porous Architectures. *ACS Nano* **10**, 3087–3092 (2016).
31. Wang, W. *et al.* Deterministic Reshaping of Breath Figure Arrays by Directional Photomanipulation. *ACS Appl. Mater. Interfaces* **9**, 4223–4230 (2017).
32. Zhu, C., Tian, L., Liao, J., Zhang, X. & Gu, Z. Fabrication of Bioinspired Hierarchical Functional Structures by Using Honeycomb Films as Templates. *Adv. Funct. Mater.* **28**, 1–8 (2018).
33. Schulte, B., Walther, A., Keul, H. & Möller, M. Polyglycidol-based prepolymers to tune the nanostructure of microgels. *Macromolecules* **47**, 1633–1645 (2014).
34. Wang, A., Cui, Y., Li, J. & Van Hest, J. C. M. Fabrication of gelatin microgels by a 'cast' strategy for controlled drug release. *Adv. Funct. Mater.* **22**, 2673–2681 (2012).
35. Le Goff, G. C., Blum, L. J. & Marquette, C. A. Shrinking hydrogel-DNA spots generates 3D microdots arrays. *Macromol. Biosci.* **13**, 227–233 (2013).
36. Hou, H., Li, F., Su, Z., Yin, J. & Jiang, X. Light-reversible hierarchical patterns by dynamic photo-dimerization induced wrinkles. *J. Mater. Chem. C* **5**, 8765–8773 (2017).